Epitaxial and Lateral Solid-Phase Crystallization of Complex Oxides

By

Yajin Chen

A dissertation submitted in partial fulfillment of

the requirements for the degree of

Doctor of Philosophy

(Materials Engineering)

at the

University of Wisconsin- Madison

2019

Date of final oral examination: 09/19/2019

The dissertation is approved by the following members of the Final Oral Committee:

Paul G. Evans, Professor, Materials Science and Engineering
Susan E. Babcock, Professor, Materials Science and Engineering
Chang-Beom Eom, Professor, Materials Science and Engineering
Xudong Wang, Professor, Materials Science and Engineering
Thomas F. Kuech, Professor, Chemical and Biological Engineering
JR Schmidt, Professor, Chemistry

Abstract

The crystallization of complex-oxide materials through a transformation from the amorphous to crystalline forms presents a range of new opportunities to synthesize new materials, and simultaneously poses important scientific challenges. New crystallization method complements more conventional vapor-phase epitaxy techniques for epitaxial complex-oxide thin film growth that involve long-range surface diffusion on 2D planar crystal surfaces. The vapor-phase techniques are not readily adaptable to creating nanoscale epitaxial complex-oxide crystals. The alternative synthesis method described in this thesis is solid-phase crystallization, which is the crystallization of amorphous oxides, often in the form of thin films, by post-deposition heating. The creation of epitaxial complex-oxide nanostructures can facilitate their integration in 3D electronic, optoelectronic and ionic devices.

Epitaxial complex-oxide crystals in intricate geometries can be created by solid-phase crystallization employing patterned substrates with a distribution of isolated crystalline seeds. This method requires the study of distinct crystal growth and nucleation kinetics on epitaxial and non-epitaxial surfaces. Nanoscale seeded crystallization can be achieved by understanding the relative rates of nucleation and lateral crystal growth processes, and the role of seeds in determining the overall orientation of the resulting crystals. Epitaxial complex-oxide thin films in intricate geometries with an expanded range of compositions can be created by combining the use of atomic layer deposition (ALD) and solid-phase crystallization, with the development of new ALD procedures to deposit amorphous oxide films and the study of the subsequent crystallization processes to select the crystalline structures of the crystallized film. ALD itself allows for the conformal deposition of thin films over non-planar surfaces.

Solid-phase crystallization can also be used to deposit epitaxial complex-oxide thin films with a wider range of compositions, including those that cannot be deposited from the vapor phase at high temperatures. Such oxides include the oxides that have complex compositions and volatile components. The different kinetic constraints of solid-phase crystallization allow the epitaxial growth of those oxide thin films because of the slow diffusion in the solid state at relatively low crystallization temperatures.

This thesis describes the discovery that, at low crystallization temperatures, epitaxial crystal growth of the model perovskite $SrTiO_3$ on single-crystal $SrTiO_3$ propagates over long distances without nucleation of $SrTiO_3$ on Si with a native oxide. Two kinds of isolated nanoscale seed crystals are employed to study the seeded lateral crystallization of $SrTiO_3$, yielding highly similar results. Micron-scale crystalline regions form surrounding the seeds before encountering separately nucleated crystals away from the seeds. Seed crystals play an important role in determining the orientations of the resulting crystals. New chemical precursors and ALD procedures were developed to grow amorphous $PrAlO_3$ films. An epitaxial γ-Al_2O_3 layer formed at the interface between the $PrAlO_3$ film and (001) $SrTiO_3$ substrate during the deposition. Epitaxial $PrAlO_3$ films were achieved on (001) γ-Al_2O_3/$SrTiO_3$ by solid-phase epitaxy. The study of $SrTiO_3$ and $PrAlO_3$ is also applicable to a series of chemically and structurally similar functional ABO_3 compounds.

The concepts of solid-phase crystallization also apply to oxides with multiple metal ions and more complex crystal structure. The kinetic processes occurring during the crystallization of $ScAlMgO_4$, on (0001) sapphire substrates are quite different at two different temperatures. Epitaxial $ScAlMgO_4$ crystals grow through the film thickness at a crystallization temperature of 950 ºC. Solid-state reaction and evaporation of the component Sc prohibits the formation of large

$ScAlMgO_4$ crystals at a crystallization temperature of 1400 ºC. Low-temperature crystallization can be used to create epitaxial oxide thin films with complex compositions and volatile components.

Acknowledgements

First and foremost, I would like to gratefully thank my advisor, Prof. Paul G. Evans, for his consistent guidance and support throughout my years at UW-Madison. He invested much time and efforts on every research project I have worked on, including a lot of useful discussions of scientific ideas and experimental details. Without his keen suggestions and insights, I would not be able to learn quickly and develop my research and technical skills. His enthusiasm for science and hard work has constantly inspired me to be persist on seeking solutions to challenging scientific problems. He has provided guidance for my professional development skills. I am fortunate to have him as my advisor and mentor in my PhD program.

I would also like to thank Prof. Susan E. Babcock and Prof. Thomas F. Kuech for their guidance and support. They have constantly helped me with the research projects described in this thesis. Besides discussion about the scientific ideas, Prof. Kuech has generously provided me with access to his laboratory, making my experiments much easier to do. Prof. Babcock sets a model example for me to pursue a successful career as a woman scientist.

I would not have been able to grow as a research scientist without the help from the current and former members in Evans group. Thanks to Kyle McElhinny for his encouragement, suggestions and generous help in my first few years of study. I give special thanks to M. Humed Yusuf, a previous post-doc in the group. I learned a lot from him about how to conduct research by working with him although he was in the group for less than a year. Our work together makes

up a significant portion of Chapter 2. Thanks to Jack Tilka for his significant contribution to a portion of the work in Chapter 3 including EBSD and synchrotron X-ray diffraction measurements. Thanks to Youngjun Ahn for his help on synchrotron X-ray diffraction measurements and teaching me the knowledge of synchrotron X-ray diffraction. Two sets of those experiments contributed to a portion of the work described in Chapter 3. I would also like to thank other group members, Joonkyu Park, Samuel Marks, Anatasios Pateras, Arunee Lakkham, Hyeonjun Lee, Deepankar Dri Gyan and Peiyu Quan. I would like to thank two undergraduates that I worked with, Aditi Datta and Adam Alfieri. I had much fun working with every member in the Evans group.

Thanks to beamline scientists Dr. Martin V. Holt and Dr. Ian McNulty at station 26-ID-C of the Advanced Photon Source at Argonne National Laboratory (ANL) for the setup of synchrotron X-ray diffraction measurements. Thanks to Dr. Deborah M. Paskiewicz and Dr. Dillon D. Fong at ANL for providing single-crystal $SrRuO_3$ nanomembranes on Si substrates for the experiments in Chapter 3.

I have the great privilege to be a student of the IRG2 group in the University of Wisconsin Materials Research Science and Engineering Center (MRSEC) since my first year in graduate school. I greatly valued the interdisciplinary and collaborative working environment in the group. Many thanks to Yingxin Guan and Peng Zuo in IRG2, who conducted the TEM characterization for the work in Chapter 2 and Chapter 5. I would also like to give a great thanks to Wathsala L. I. Waduge and Prof. Charles H. Winter at Wayne State University. They have been wonderful collaborators. They were always open to discussing questions and generous for my requests of providing additional samples. My work with them makes up a significant portion of Chapter 4. I owe many thanks to other scientists and professors in the IRG2 group including Dr. Donald Savage, Prof. Chang-Beom Eom and Prof. JR Schmidt. They provided me many useful discussions

and excellent new scientific ideas. I greatly appreciate the opportunity of being a student member of the Executive Committee of MRSEC for a year. I acquired some extracurricular skills through the participation of a variety of MRSEC professional development and outreach activities that I would not have learned by just being a graduate student.

I greatly thank Dr. J. H. Fournelle in the Department of Geology and Geophysics at UW-Madison for the EPMA-WDS measurements of the thin films described in Chapter 4 and Chapter 5. I would like to give a special thanks to Prof. Max Lagally and RB Jacobson. Prof. Lagally provided me a sputtering system to work with. RB helped me construct and maintain the sputtering system for the deposition of STO films described in this thesis. He taught me many technical skills and helped me trouble shoot numerous problems of the instrument. I would not be able to learn about high-vacuum deposition systems quickly without him.

Finally, yet most importantly, I would like to thank my family, my grandfather, grandmother, my parents Li Chen and Ailing Li, and my brother, Shitao Chen. It is not easy to study abroad being far from the family. Their continuous encouragement, support and love has inspired me to insist on what I am doing. I hope I can be a person they are proud of. I'm very fortunate to meet my boyfriend, Teng Wei, also a PhD student at UW-Madison. His support and advice has helped me come across numerous challenges and dilemma in my PhD program.

The research projects described in this thesis were primarily supported by NSF Division of Materials Research through the University of Wisconsin Materials Research Science and Engineering Center (Grants DMR-1121288 and DMR-1720415).

Table of Contents

Chapter 1: Motivation and introduction

1.1 Motivation and overview

Complex oxides include a broad class of materials with a wide range of functionalities. To name a few, complex oxides exhibit thermoelectricity,[1] ferroelectricity,[2] magnetism,[3] and high-temperature superconductivity.[4] Crystalline complex oxides in the form of nanostructures and three-dimensional structures exhibit promising thermal, electronic and optical properties that are modified by nanoscale size effects. Examples of the opportunities arising from nanoscale control over the composition and structural phase include the creation of materials with promising thermoelectric properties and reduced thermal conductivity,[5-6] the interfaces exhibiting quantum electronic effects,[7-8] and the structures for optical devices with higher efficiency.[9]

Epitaxial complex-oxide thin films with a wide range of compositions have been routinely deposited by vapor-phase epitaxy techniques including thermal and electron-beam evaporation, molecular beam epitaxy, on- and off-axis sputtering and pulsed laser deposition (PLD).[10] Lattice-matched planar substrates are often used in those techniques to avoid the formation of defects induced by the difference between the lattice parameters of the thin film and the substrate.[10] Epitaxial oxide thin films deposited from the vapor phase are limited to two-dimensional geometries because of the line-of-sight transport of materials from sources to the planar substrates.

Vapor phase epitaxy techniques also require the use of high substrate temperatures to induce long-range surface diffusion for the *in situ* growth of crystalline films.[10] Some problems can arise during deposition at high substrate temperatures. One such problem occurs when one component of complex oxides forms volatile oxides at high deposition temperatures. A second

problem occurs when oxide thin films with other metastable compositions can exhibit phase separation at high temperatures, for example the formation of multiple phases in place of the desired single structural phase.

An alternative thin film synthesis method that complements vapor-phase epitaxy is solid-phase crystallization, which involves lower-temperature deposition process of the amorphous thin films and subsequent *ex situ* crystallization process. Because of the separation of deposition and crystallization processes, solid-phase crystallization faces different kinetic phenomena than vapor-phase epitaxy techniques.

The different kinetic constraints have the potential to allow deposition and crystallization of complex oxides in nanoscale intricate geometries. A patterned three-dimensional substrate part of which is composed of nanoscale crystalline seeds can be used to deposit the amorphous oxide films.[11-12] Oxide thin films in the amorphous form can also be deposited using techniques that do not rely on maintaining line-of-sight during deposition. The crystalline structures of the crystallized films starting from the initially amorphous form can then be selected by understanding the crystallization surrounding the crystalline seeds and away from the seeds.

The different kinetic constrains also allow solid-phase crystallization to be employed to avoid problems that can arise during deposition at high substrate temperatures. The compounds that have volatile components or other metastable compositions are first created in the amorphous form at low temperatures. The amorphous thin films are then by crystallized into crystalline structures with the same compositions by choosing crystallization conditions. On one hand, the diffusion of materials in the solid state is slow during crystallization. For example, the diffusion lengths of O and Al in solid Al_2O_3 are estimated to be less than 1 Å even for a relatively long crystallization time of 24 h at 1000 ºC.[13] On the other hand, evaporation of volatile components

and phase separation can be avoided in crystallization by understanding the crystallization kinetics and carefully selecting the crystallization conditions. A few successful examples in the literature of using solid-phase crystallization include the growth of epitaxial oxide thin films of superconducting $HgBa_2CaCu_2O_x$ and pyrochlore iridates with interesting magnetic properties despite the high volatility of Hg and Ir.[14-15]

The topic of this thesis is about the study of solid-phase crystallization to create complex-oxide thin films with intricate geometries and with new compositions. The possibility of creating complex-oxide thin films with intricate geometries was investigated by understanding the crystallization mechanisms and kinetics on substrate surfaces with distinct crystalline order, by studying the nanoscale control of the nucleation sites on a planar substrate, and also by exploring the deposition of amorphous oxide thin films that does not require the line-of-sight geometry. The creation of complex-oxide thin films with new compositions was investigated by studying the solid-phase crystallization of an oxide thin film with complex compositions that have volatile components and cannot be deposited using vapor-phase epitaxy.

Amorphous oxide thin films can be created by a wide range of techniques at substrate temperatures that are lower than the crystallization temperatures of the amorphous oxides. The techniques include ion implantation into crystalline materials,[16] sputter deposition,[17-19] PLD,[20] and atomic layer deposition (ALD).[9,21] Among the techniques, sputter deposition was chosen to deposit amorphous oxide thin films for solid-phase crystallization in Chapters 2, 3 and 5, because a wide range of alloys and compounds with the desired compositions can be deposited with this method. The deposited films by sputtering are smooth, with high-purity, and have excellent uniformity on large-area substrates.[22] The deposition of amorphous oxide thin films using ALD was particularly studied in Chapter 4 because ALD technique allows for precise control of the film thickness and

conformal deposition on high-aspect-ratio structures.[23-25] Low-temperature deposition is often required in ALD resulting in amorphous films.[23-25] The features of ALD technique are promising to study the crystallization amorphous oxide thin films in intricate geometries.

The crystallization mechanisms of amorphous oxide thin films on different substrate surfaces are not straightforward and have not been well explored yet. Even for the crystallization of amorphous oxides on the single-crystal substrates with the same compositions, the resulting crystalline structures can be different depending on the polymorphs of oxides. Simple crystalline oxides with competing polymorphs can exhibit complex crystallization phenomena. The crystallization of amorphous Al_2O_3 on single-crystal α-Al_2O_3 occurs by an initial transformation of amorphous Al_2O_3 to γ-Al_2O_3 and a subsequent transformation to epitaxial α-Al_2O_3.[26-27] The crystallization of compounds without competing polymorphs proceeds via more straightforward processes. The crystallization of several ABO_3 perovskite compounds $SrTiO_3$ (STO), $CaTiO_3$, and $BaTiO_3$ on single-crystal substrates occurs through a planar motion of the amorphous/crystalline interface toward the sample surface during the crystallization process, resulting in an epitaxial thin film with the same phase and orientation as the substrate.[16,27-31] This process is termed solid-phase epitaxy (SPE). SPE is a well-known process and extensively studied in semiconductors silicon and germanium.[32-34]

STO was chosen as the subject of the crystallization studies described in Chapters 2 and 3 of this thesis because of the experimental advantages arising from its simple-cubic symmetry and lack of competing polymorphic phases. STO was chosen also because it serves as a model system for perovskite oxides of technological interest and it has a wide range of functionalities. These functionalities include high dielectric permittivity,[35] room-temperature ferroelectricity in nanoscale crystals,[36] two-dimensional electron transport,[8] superconductivity,[7] and large

magnetoresistance and magnetic hysteresis at $LaAlO_3/SrTiO_3$ interfaces.[37] Because STO and other perovskites have similar structural and chemical properties, it is likely that the growth kinetics of STO are applicable to the formation of structurally similar complex oxides on other crystalline substrates and in more complex geometries.

1.2 Outline of thesis

This thesis reports detailed studies of the crystallization of amorphous complex-oxide thin films and nanostructures in which the amorphous material is prepared by sputter deposition. The construction of a sputter deposition system for this project is described in section 1.3 of Chapter 1. Several key X-ray diffraction techniques were employed in this thesis to characterize the structures of the amorphous and crystallized thin films. Section 1.4 of Chapter 1 describes the grazing-incidence X-ray scattering technique which was used to measure the scattered X-ray intensity from amorphous oxide thin films through this thesis. Section 1.5 of Chapter 1 provides the details of the synchrotron X-ray nanobeam diffraction method which was used to obtain the local structural information of nanoscale materials. Section 1.6 of Chapter 1 introduces the experimental method of laboratory high resolution θ-2θ scans to study the epitaxial relationship between the epitaxially crystallized thin films and single-crystal substrates.

The crystallization of amorphous oxides in intricate geometries requires the understanding of the relative rates of nucleation and growth on different substrate surfaces. Chapter 2 describes a systematic study of the distinct crystallization mechanisms and kinetics of STO on single-crystal (001) STO surfaces and Si surfaces with a native oxide, termed SiO_2/Si. The key insight in this study is that the amorphous-to-crystalline transformation on the two surfaces is significantly different. The crystallization of amorphous STO on (001) STO occurs by SPE and the

crystallization of amorphous STO on SiO_2/Si requires nucleation and growth. The distinct rates of nucleation and crystal growth allow amorphous STO to crystallize by SPE over long distances without nucleation on SiO_2/Si at a relatively low crystallization temperature of 450 ºC. The study demonstrates the possibility of creating epitaxial STO crystals in intricate geometries using solid-phase crystallization.

Nanoscale control of the nucleation sites on a planar substrate is another way to create complex oxides in nanoscale intricate geometries. Chapter 3 describes the study of the lateral solid-phase crystallization of an amorphous STO layer on an amorphous SiO_2/Si substrate with nanoscale seed crystals. Two kinds of seed crystals with different compositions and structures were employed to study the seeded lateral crystallization of STO: isolated STO nanocrystallites with random crystallographic orientations and single-crystal (001) $SrRuO_3$(SRO) nanomembranes. The lateral crystallization rates from both seeds are isotropic and are close to the vertical SPE growth rate of STO on (001) STO investigated using STO/STO homoepitaxy. The process in the amorphous phase instead of the process at the amorphous/crystalline interface determines the lateral crystallization rates. Micron-scale crystalline regions form surrounding the seeds before encountering separately nucleated crystals away from the seeds. Seed crystals play an important role in determining the orientations of the resulting crystals. This study points out to the opportunities of creating epitaxial complex-oxide nanostructures using seeded solid-phase crystallization.

Epitaxial complex-oxide thin films in intricate geometries with an expanded range of compositions can be created by developing the deposition of their amorphous layers by ALD. Chapter 4 discusses the development of new ALD precursors and procedures for the deposition of amorphous lanthanide aluminate thin films, using $PrAlO_3$ as an example, and the study of the SPE

growth of amorphous films on (001) STO. New chemical precursors that have the self-limiting growth mechanism were developed to grow amorphous $PrAlO_3$ films by ALD. The as-deposited amorphous films are slightly Al-rich, but with constant Pr:Al ratios and without impurities. The crystallization kinetics of amorphous $PrAlO_3$ films on SiO_2/Si and (001) STO substrates is dramatically different. The as-deposited $PrAlO_3$ films on amorphous SiO_2/Si substrates remained amorphous even after heating at 1000 ºC for 8 h. Amorphous $PrAlO_3$ films on crystalline (001) STO substrates grew epitaxially after crystallization at 800 ºC for 3 h. Epitaxial γ-Al_2O_3 layers formed at the interfaces between the amorphous $PrAlO_3$ films and the STO substrates during the growth by ALD. The interfacial layers play a key role in determining the crystalline structure of the crystallized $PrAlO_3$ film. The epitaxial relationship of the crystallized film on STO was actually [001] $PrAlO_3$ // [001] Al_2O_3 // [001] STO.

Solid-phase crystallization can be employed to create epitaxial oxide thin films with a wider range of compositions, including the oxides that have complex compositions and volatile components so that their thin film form cannot be deposited with conventional vapor phase epitaxy techniques. Chapter 5 discusses the crystallization of amorphous $ScAlMgO_4$ thin films created by sputter deposition on widely available (0001) sapphire substrates. The crystallization of amorphous $ScAlMgO_4$ at a relatively low temperature of 950 ºC and at a relatively high temperature of 1400 ºC was studied and showed different results. Epitaxial $ScAlMgO_4$ crystals throughout the film thickness formed on sapphire substrates after crystallization at 950 ºC for 10 h. In contrast, a large amount of oriented $MgAl_2O_4$ crystals formed on sapphire substrates after crystallization at 1400 ºC for 30 min, because complicated processes occurred including evaporation of Sc, long-range diffusion of Sc and reaction with the sapphire substrate. This study

shows that crystallization at relatively low temperatures needs to be employed for the growth of epitaxial oxide thin films that have complex compositions and volatile components.

1.3 Sputter deposition

Sputter deposition was employed to deposit amorphous thin films of STO and $ScAlMgO_4$ described in Chapters 2, 3 and 5 of this thesis. Sputtering occurs through the bombardment of accelerated ions on the surface of a solid target, which is a momentum transfer process.[19] Magnetron sputtering has been used in this study because higher deposition rates can be achieved and glow discharge can be maintained at lower working gas pressures.[22,38] Detailed reviews about sputtering processes and magnetron sputtering can be found in the literature.[19,22,38-39]

A sputter deposition system was constructed in order to conduct the research projects described in this thesis. Figure 1-1 shows a schematic diagram of the sputter deposition system and Figure 1-2 shows the general layout of the system. The system is composed of four major components: vacuum pumps, sputter sources, power supplies, and the vacuum chamber.

A rotary vane mechanical pump and a cryopump are used for the vacuum pumping. The mechanical pump (Leybold D30A Trivac) takes the chamber pressure down to be less than 100 mTorr first. A lower pressure is achieved using the cryopump (CTI cryogenics 8200). A pressure of 10^{-6} torr or lower can be reached. A molecular sieve foreline trap was installed above the mechanical pump to avoid the backflow of oil into the chamber. A manual bellows sealed valve was installed above the foreline trap to isolate the mechanical pump and the chamber. A gate valve and an exhaust valve were installed between the chamber and the cryopump. The pressure inside the chamber can be adjusted by adjusting the opening of the exhaust valve. An in-line valve was installed between the mechanical pump and the cryopump, which is used for the regeneration of

the cryopump regularly. A chiller (Neslab CFT-75) is used to provide cooling water for the compressor of the cryopump and the sputtering sources.

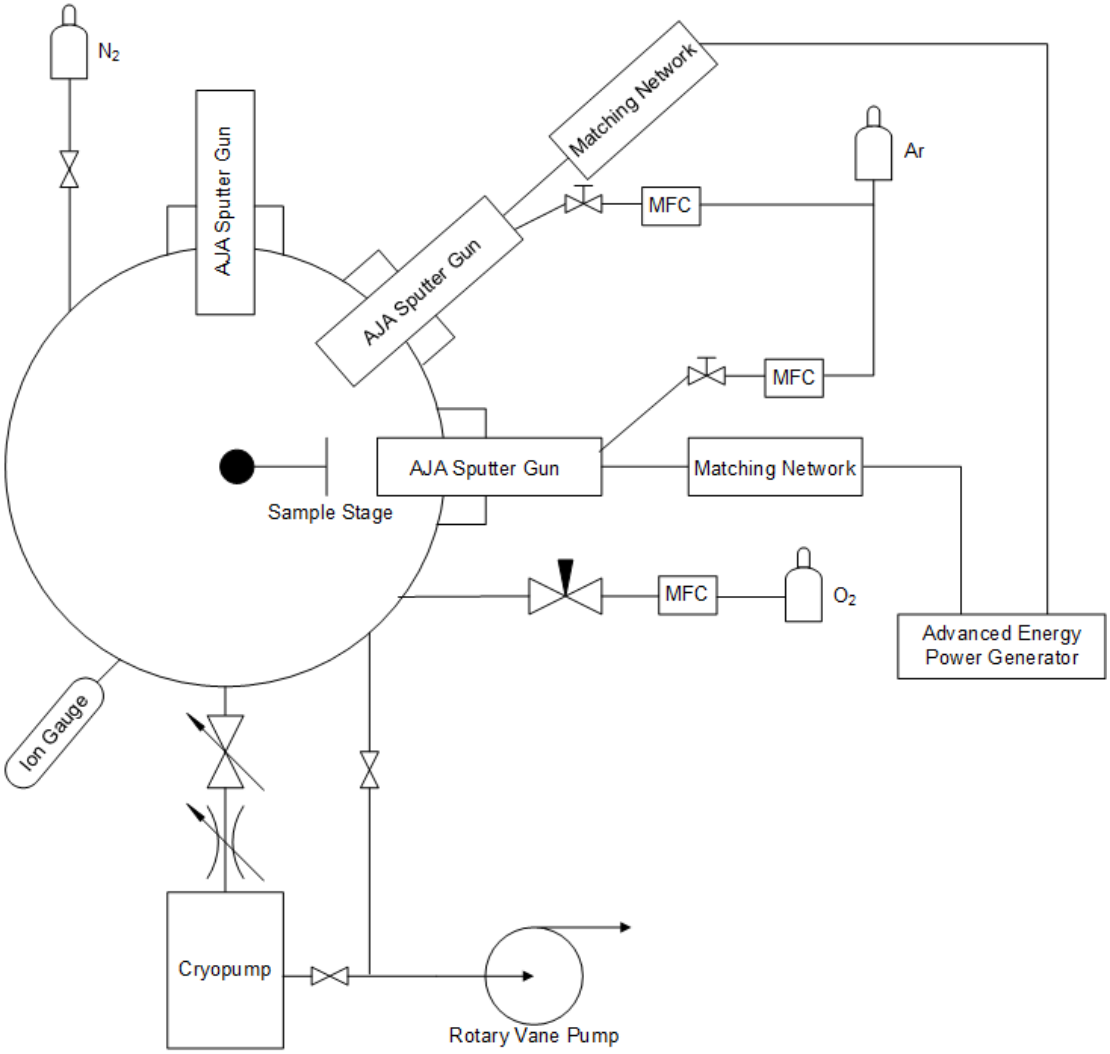

Figure 1-1. Schematic diagram of the sputter deposition system.

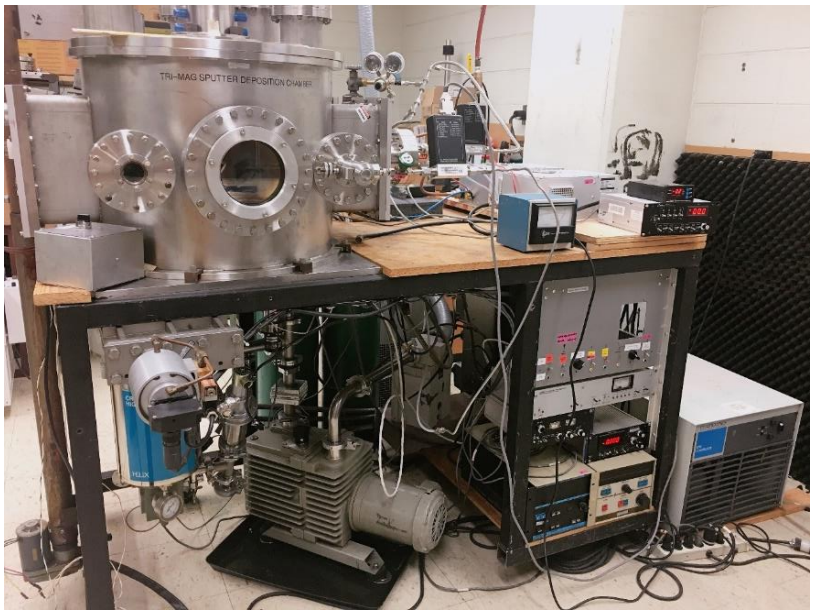

Figure 1-2. General layout of the sputter deposition system.

Three magnetron sputtering sources (AJA A320) were installed on three flanges of the chamber. Detailed configuration of the sputtering source can be found in the manual.[40] Figure 1-3 shows a simplified schematic diagram of the magnetron sputtering process. The deposition processes described in this thesis used argon gas for the sputter deposition. Ar^+ is generated by ionization of the Ar gas. The sputter deposition uses sources of material termed targets. The electric field makes the target a cathode and the substrate an anode. Ar^+ bombards the cathode surface and sputters off target surface atoms or molecules. The sputtered atoms or molecules deposit on the substrate resulting in a thin film. A magnetic field can trap electrons close to the target surface, where more gas atoms can be ionized by the electrons. The sputtering rates and deposition rates of thin films are thus higher at a given working gas pressure using magnetron sputtering. Moreover, the glow discharge can be maintained at lower working gas pressures because of the higher ionization rates near the target surface.[19,22,38-39] A radio frequency (RF) power supply is used to prevent positive ions Ar^+ from building up on the surface of the insulating target.[19,22,38-39]

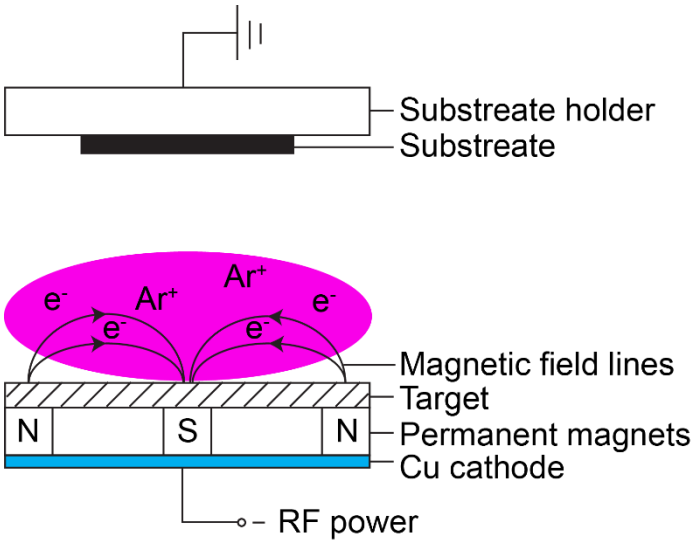

Figure 1-3. Simplified schematic diagram of magnetron sputtering process. The detailed configuration of the sputtering source including the ground shield and water cooling is not shown.

The oxide targets for this sputtering source are 2'' in diameter and 0.125'' in thickness and are bonded to a raised copper backing plate for better thermal conductivity. In order to minimize target cracking, the RF power is slowly ramped up to, and down from, the desired operating power level. Special attention should be paid when installing the target inside the sputtering source. There must not be an electrical short-circuit between the cathode assembly and the ground shield. The spacing between the top of clamping ring and ground shield should be between 0.75 and 2 mm when the working pressure is less than 30 mTorr. A shutter is placed in front of the sputtering source, between the target and the substrate. At the initial stage of sputtering, the shutter is closed so that the impurities on target surface are not sputtered onto the substrate and the sputtering conditions can be stabilized.

An RF power supply (Advanced Energy RFX 600 Generator) is used in this system to deliver power to the sputtering source. A matching network is used between the power supply and the sputtering source. The matching network can transform the impedance of the load to be 50 Ω. The reflected power can thus be minimized, and the power delivered to the sputtering source can

be maximized. The frequency used for the RF power supply is 13.56 MHz. A gas pressure of 30 mTorr and a power of 30 W is used to strike a plasma. After the plasma is stable, the gas pressure and power can be adjusted to the desired values.

The main vacuum chamber contains several flanges, three of which have sputtering sources installed. The chamber is 23 in. in diameter and 18 in. in height. The top plate of the chamber seals the chamber and can be raised to provide access to the sample holder and sputter guns. The substrate holder is attached to the center of the chamber top plate. The substrate holder is rotatable and can face each target individually. The position of the substrate holder relative to the center of the chamber is determined based on the target-substrate working distance. The deposition rate has approximately an inverse square relationship to the working distance.[41] The working distance is recommended to be from 50 to 200 mm for the sputtering source of this system.[40] The working distance of this system is 100 mm.

Two pressure gauges are used to measure the pressure inside the chamber. An ion gauge is used to measure the base pressure of the vacuum, ranging from 10^{-4} to 10^{-9} Torr. A capacitance manometer (MKS Baratron 270, 0-1000 mTorr) is used to measure higher pressures in the chamber such as the working pressure during deposition. The working gasses for the sputtering processes used in this study consist of Ar or Ar/O_2 mixture. Both Ar and O_2 gases are introduced into the chamber through mass flow controllers with the measurement and control of the flow of gases.

The detailed procedures for the use of this sputtering system are summarized in Table 1-1, including how to load a substrate, pump down the system, deposit a thin film and unload the deposited sample. The deposition conditions such as RF power and gas pressures described here are what used for the deposition of amorphous STO thin films. The deposition conditions vary depending on the materials that need to be deposited.

Table 1-1. Procedures for the use of the sputtering system to deposit amorphous STO thin films.

Load a substrate: 1) Turn off gate valve; 2) Turn exhaust valve from 10 to 0; 3) Turn on N_2 backfill; 4) Open N_2 gas tank; 5) Wait 5-10 min, then open chamber; 6) Once chamber is open, close N_2 gas tank and turn off N_2 backfill; 7) Load a substrate; Make sure the shutter of sputter source is closed; 8) Rotate substrate holder to face sputter source; 9) Close chamber.	**Pump down the system:** 1) Make sure N_2 gas tank is closed and N_2 backfill is off; Turn on the mechanical pump, wait for pressure gauge reaches 20 mTorr; 2) Open manual valve; 3) Turn on "Forepump to Chamber"; 4) Wait for Baratron pressure to read 50 mTorr; 5) Turn off "Forepump to Chamber"; 6) Close manual valve; 7) Turn off the mechanical pump; 8) Turn exhaust valve from 0 to 10; 9) Open gate valve; 10) Make Sure the system starts pumping down.
Deposit a thin film (conditions used for amorphous STO film deposition): 1) Turn exhaust valve from 10 to 0 to fully close; 2) Turn on ion gauge, turn ON filament, allow gauge to stabilize for a minute; 3) Pressure should be about 2×10^{-6} Torr or less; 4) Turn OFF filament, turn off ion gauge; 5) Open Ar gas tank and open manual valve of Ar gas line; Open Ar mass flow controller (MFC), channel 3 to AUTO (not open); 6) Turn display value for MFC to 115-125 to get Baratron reading of 30.0 ± 0.1 mTorr; 7) Turn on RF power (forward power should be 29 W and reflected power should be less than 5W. Check the problem if reflected power is larger than 5 W); 8) Let plasma strike for 10 min; 9) Adjust Ar gas flow to be 53-61 on display to get Baratron reading of 16.0-16.1 mTorr; 10) Open O_2 gas tank and open manual valve of O_2 gas line; Turn on O_2 MFC channel 3, should already be set at 24.9 on display; 11) Ensure RF forward power is still 29 W; 12) Pre-sputter for 10 min; 13) Open shutter of sputter gun, record time; 14) Allow to sputter for allotted time.	**Unload the deposited sample:** 1) Turn off RF power and close power supply; 2) Close MFC of Ar and O_2; 3) Close Ar, O_2 manual valves and gas tanks; 4) Close shutter of sputter gun; 5) Close gate valve between chamber and cryopump; 6) Flow N_2 gas to vent chamber; 7) Open chamber, turn off N_2 gas; 8) Remove sample; 9) Load a new substrate or pump down chamber without loading.

1.4 Grazing-incidence X-ray scattering

X-ray scattering and diffraction techniques allow the study of the structure of amorphous thin films. The X-ray diffraction patterns of crystalline materials often exhibit Bragg reflections because of the long-range periodic structures of crystalline materials.[42] Because amorphous materials do not have long-range translational order, no Bragg reflections will be observed for amorphous materials.[42] The X-ray diffraction patterns of amorphous materials exhibit a broad single halo or a few broad halos with intensity maxima because amorphous materials have short-range order.[42-43] In the studies present in this thesis, lab-source grazing-incidence X-ray scattering was used to study the amorphous thin films.

Grazing-incidence X-ray diffraction studies were conducted employing a Bruker D8 Advance diffractometer with Cu Kα radiation. The source power is 50 W and the X-ray wavelength is 1.54 Å. The scattered intensity was recorded using a two-dimensional area detector (VANTEC500). Figure 1-4 shows the lab-source grazing-incidence X-ray scattering geometry. A grazing incident angle of the X-ray beam was chosen, based on the beam width and sample size, to optimize the amorphous peak signal by maximizing the X-ray footprint on the sample surface. The introduction of a knife-edge into the measurement geometry dramatically increases the signal-background ratio in the data because the knife-edge blocks scattered X-ray intensity from air at the small 2θ angles that are close to where the amorphous peak is expected to appear. The knife-edge was a wedge made of a nickel-based alloy that absorbs X-rays. As shown in Figure 1-4, the knife-edge was placed directly above the middle of the thin-film sample between the X-ray source and the detector. The signal-background ratio is thus greatly increased in the resulting X-ray diffraction patterns.

The maximum signal from the thin film is obtained when the X-ray footprint on the sample surface is as large as the length of the thin film. The incident angle was thus chosen using the following equation:

$$sin\alpha = \frac{d}{L}$$

Here, α is the grazing incident angle, d is the X-ray beam spot size, L is the length of the thin film. The center of the detector is positioned at a 2θ angle where the amorphous peak is expected to be. The X-ray beam spot size was 0.5 mm in the grazing-incidence X-ray scattering measurements of amorphous thin films in this thesis.

Taking the samples in Chapter 2 as an example, the STO film deposited on a SiO_2/Si substrate was 20 mm long and the STO film deposited on a (001) STO substrate was 9 mm long because the film length was limited by the substrate size. The incident angles for STO on SiO_2/Si and STO on STO are thus 1.4º and 3.2º respectively. The investigated volume of materials is small because the deposited amorphous STO films are only 50 or 60 nm thick. A long exposure time was used for each measurement of 1800 s.

Amorphous materials have only short-range order. The scattered X-ray intensity from amorphous materials come from the probability of finding a neighboring atom.[42] The bond distance of Ti-O, Sr-O and O-O in STO is 1.94, 2.75 and 2.75 Å respectively.[44] The highest scattered X-ray intensity from amorphous STO is expected to be located around 2θ=32º based on the bond distances. The area detector has a large opening angle of 32º. The center of the detector is positioned at 2θ=30º, which is enough to capture the broad amorphous peak.

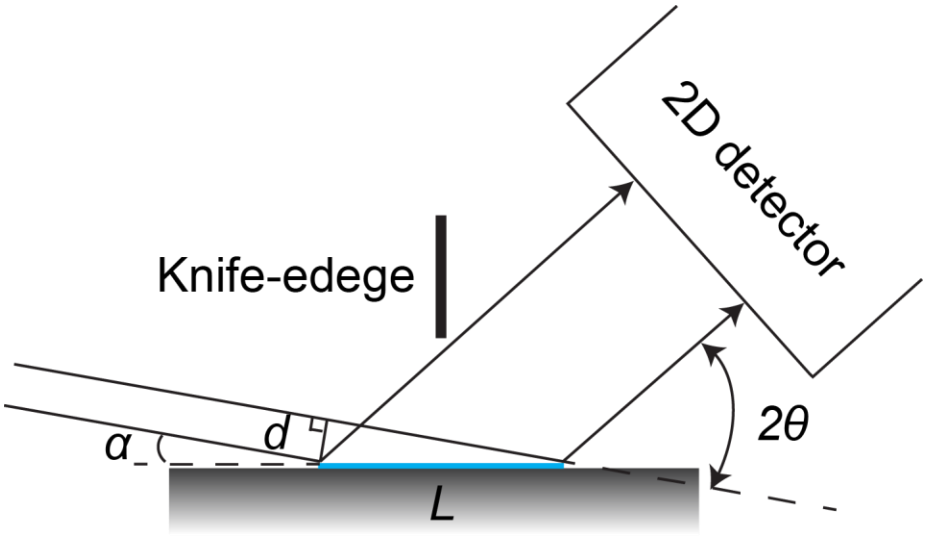

Figure 1-4. Lab-source grazing-incidence X-ray scattering geometry to characterize amorphous thin films. Blue part represents a thin-film sample.

The grazing-incidence X-ray diffraction method is a key tool for the projects described in this thesis. This method is valuable for people to study sub-micron amorphous thin films more widely. This method can be used to identify whether amorphous materials exist in a thin-film sample even when the sample also has crystalline phases. Standard powder X-ray diffraction measurements only measure Bragg reflections from the crystalline phases that have strong intensities. This method measures the relatively weak intensities from amorphous materials. This method can also be used to study the amorphous-to-crystalline phase transformation inside the thin film. The rates of amorphous-to-crystalline phase transformation are known based on the rates of decrease of the scattered X-ray intensity from amorphous materials. Chapter 2 gives an example how the kinetics of amorphous-to-crystalline phase transformation can be quantitatively studied using this method.

1.5 X-ray nanobeam diffraction

Chapter 3 describes how a-few-nanometer thick STO or tens-of-nanometer thick SRO seed crystals can be employed to template the crystallization of an amorphous STO layer. Structural characterization of the nanoscale seed crystals is important to study their roles in determining the crystalline structures of the crystallized STO film. The resolved local characterization of the structures of the locally crystallized STO on top of or laterally away from the seed crystals is also required.

The hard X-ray nanoprobe at station 26-ID-C of the Advanced Photon Source at Argonne National Laboratory provides a tightly focused X-ray beam that can be used for structural studies of nanoscale materials.[45] The photon energies of X-ray beam in this beamline can range from 3 to 30 keV.[46] By using Fresnel zone plate X-ray focusing optics, together with sensing and motion controls, the X-ray nanobeam reaches a focal spot size as small as 30 nm.[46] The X-ray beam focal spot size is largely determined by the outermost zone width of the zone plate, which is 24 nm in this case.[46] The details of the working mechanisms of Fresnel zone plates can be found elsewhere.[47-48]

Figure 1-5 shows a diagram of the focused X-ray nanobeam diffraction geometry. The center stop is used to block the transmitted X-rays and the order sorting aperture is used to block the unfocused and secondary X-rays. Only the first order focus of the beam arrives at the sample. In the experiments described in Chapter 3, the samples were mounted in a vacuum chamber and all measurements were conducted with a horizontal scattering geometry. A hybrid pixel array detector (LynX 1800 Medipix 3RX) was used to record the scattered X-ray intensity. The detector

has 516 × 516 pixels with an area effectively consisting of a stripe with a width of 4 pixels as a dead gap between quadrants in the middle of the detector. The pixel size is 55 μm.

Chapter 3 includes two sets of experiments using the hard X-ray nanoprobe. For studies of the structures of the SRO nanomembranes and the vertically crystallized STO film on top of the SRO nanomembranes, an X-ray nanobeam with a photon energy of 9 keV (λ=1.3776 Å) and a focal spot size of 50 nm were used. In another set of experiment using the geometry described in Figure 1-5, the X-ray nanoprobe was used to obtain structural information of the widely dispersed nanoscale STO seed crystals deposited on part of the SiO_2/Si substrates, employing an X-ray nanobeam with a photon energy of 10 keV (λ=1.2398 Å) and a focal spot size of 30 nm.

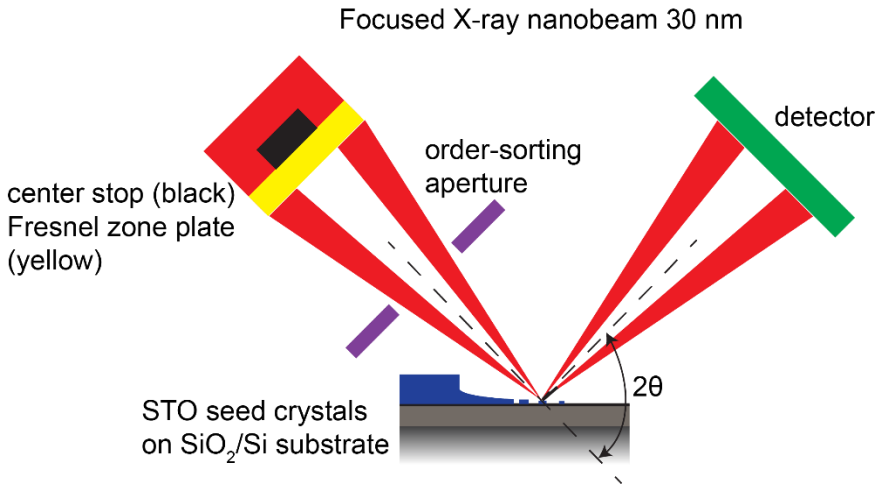

Figure 1-5. Focused X-ray nanobeam diffraction geometry to obtain structural information of the nanoscale STO seed crystals deposited on part of the SiO_2/Si substrates.

1.6 Laboratory thin-film θ-2θ scan

The epitaxial growth of amorphous thin films on top of single-crystal seeds or substrates was probed using laboratory high resolution θ-2θ scans, which measure the scattered X-ray intensity along the out-of-plane direction of the single-crystal seeds or substrates.

For the epitaxial growth of an amorphous STO film on top of the (001)-oriented SRO nanomembrane described in Chapter 3, a θ-2θ scan was conducted along the sample normal direction using PANalytical X'Pert MRD with monochromatic Cu $K\alpha_1$ radiation at λ=1.5406 Å.

θ-2θ scans along the sample normal direction were employed to study both the epitaxial relationship between the crystallized $PrAlO_3$ films and the (001) STO substrates described in Chapter 4, and the epitaxial relationship between the crystallized $ScAlMgO_4$ films and the (0001) sapphire substrates described in Chapter 5. Those θ-2θ scans in Chapter 4 and Chapter 5 were measured with a PANalytical Empyrean diffractometer equipped with Cu $K\alpha_1$ radiation (λ = 1.5406 Å) at a generator voltage of 40 kV and emission current of 40 mA.

1.7 References

1. Koumoto, K.; Terasaki, I.; Funahashi, R. Complex Oxide Materials for Potential Thermoelectric Applications. *MRS Bull.* **2006,** *31* (3), 206-210.
2. Setter, N.; Damjanovic, D.; Eng, L.; Fox, G.; Gevorgian, S.; Hong, S.; Kingon, A.; Kohlstedt, H.; Park, N. Y.; Stephenson, G. B.*; et al.* Ferroelectric Thin films: Review of Materials, Properties, and Applications. *J. Appl. Phys.* **2006,** *100* (5), 051606.
3. Solovyev, I.; Hamada, N.; Terakura, K. Crucial Role of the Lattice Distortion in the Magnetism of $LaMnO_3$. *Phys. Rev. Lett.* **1996,** *76* (25), 4825-4828.
4. Lin, H.; Wu, N. J.; Geiger, F.; Xie, K.; Ignatiev, A. A Ferroelectric-Superconducting Photodetector. *J. Appl. Phys.* **1996,** *80* (12), 7130-7133.
5. Ohtaki, M.; Koga, H.; Tokunaga, T.; Eguchi, K.; Arai, H. Electrical Transport Properties and High-Temperature Thermoelectric Performance of $(Ca_{0.9}M_{0.1})MnO_3$ (*M* = Y, La, Ce, Sm, In, Sn, Sb, Pb, Bi). *J. Solid State Chem.* **1995,** *120*, 105-111.
6. Vineis, C. J.; Shakouri, A.; Majumdar, A.; Kanatzidis, M. G. Nanostructured Thermoelectrics: Big Efficiency Gains from Small Features. *Adv. Mater.* **2010,** *22*, 3970-3980.
7. Reyren, N.; Thiel, S.; Caviglia, A. D.; Kourkoutis, L. F.; Hammerl, G.; Richter, C.; Schneider, C. W.; Kopp, T.; Ruetschi, A. S.; Jaccard, D.*; et al.* Superconducting Interfaces between Insulating Oxides. *Science* **2007,** *317*, 1196-1199.
8. Ohtomo, A.; Hwang, H. Y. A High-Mobility Electron Gas at the $LaAlO_3/SrTiO_3$ Heterointerface. *Nature* **2004,** *427*, 423-426.
9. Jang, J.; Moon, D.; Lee, H. J.; Lee, D.; Choi, D.; Bae, D.; Yuh, H.; Moon, Y.; Park, Y.; Yoon, E. Incorporation of Air-Cavity into Sapphire Substrate and its Effect on GaN Growth and Optical Properties. *J. Cryst. Growth* **2015,** *430*, 41-45.
10. Habermeier, H. U. Thin Films of Perovskite-Type Complex Oxides. *Mater. Today* **2007,** *10* (10), 34-43.

11. Taira, K.; Hirose, Y.; Nakao, S.; Yamada, N.; Kogure, T.; Shibata, T.; Sasaki, T.; Hasegawa, T. Lateral Solid-Phase Epitaxy of Oxide Thin Films on Glass Substrate Seeded with Oxide Nanosheets. *ACS Nano* **2014,** *8*, 6145-6150.
12. Ishiwara, H.; Yamamoto, H.; Furukawa, S.; Tamura, M.; Tokuyama, T. Lateral Solid-Phase Epitaxy of Amorphous Si Films on Si Substrates with SiO_2 Patterns. *Appl. Phys. Lett.* **1983,** *43* (11), 1028-1030.
13. Evans, P. G.; Chen, Y.; Tilka, J. A.; Babcock, S. E.; Kuech, T. F. Crystallization of Amorphous Complex Oxides: New Geometries and New Compositions via Solid Phase Epitaxy. *Curr. Opin. Solid State Mater. Sci.* **2018,** *22*, 229-242.
14. Tsuei, C. C.; Gupta, A.; Trafas, G.; Mitzi, D. Superconducting Mercury-Based Cuprate Films with a Zero-Resistance Transition-Temperature of 124 Kelvin. *Science* **1994,** *263* (5151), 1259-1261.
15. Fujita, T. C.; Kozuka, Y.; Uchida, M.; Tsukazaki, A.; Arima, T.; Kawasaki, M. Odd-Parity Magnetoresistance in Pyrochlore Iridate Thin Films with Broken Time-Reversal Symmetry. *Sci. Rep.* **2015,** *5*.
16. White, C. W.; Boatner, L. A.; Sklad, P. S.; Mchargue, C. J.; Rankin, J.; Farlow, G. C.; Aziz, M. J. Ion-Implantation and Annealing of Crystalline Oxides and Ceramic Materials. *Nucl. Instrum. Methods Phys. Res., Sect. B* **1988,** *32*, 11-22.
17. Ngoc, L. H. H.; Hirose, Y.; Nakao, S.; Hasegawa, T. Crystallization Kinetics of Amorphous Sputtered Nb-Doped TiO_2 Thin Films. *Appl. Phys. Express* **2011,** *4* (10).
18. Chen, Y. J.; Yusuf, M. H.; Guan, Y. X.; Jacobson, R. B.; Lagally, M. G.; Babcock, S. E.; Kuech, T. F.; Evans, P. G. Distinct Nucleation and Growth Kinetics of Amorphous $SrTiO_3$ on (001) $SrTiO_3$ and SiO_2/Si: A Step toward New Architectures. *ACS Appl. Mater. Interfaces* **2017,** *9*, 41034-41042.
19. Wasa, K. *Handbook of Sputter Deposition Technology: Fundamentals and Applications for Functional Thin Films, Nanomaterials, and MEMS*, Elsevier Inc.: Waltham, 2012; p 629-630.
20. Shimamoto, K.; Hirose, Y.; Nakao, S.; Fukumura, T.; Hasegawa, T. Solid Phase Epitaxy of $EuTiO_3$ Thin Films on $SrTiO_3$ (100) Substrates with Different Oxygen Contents. *J. Cryst. Growth* **2013,** *378*, 243-245.
21. Akbashev, A. R.; Chen, G. N.; Spanier, J. E. A Facile Route for Producing Single-Crystalline Epitaxial Perovskite Oxide Thin Films. *Nano Lett.* **2014,** *14*, 44-49.
22. Swann, S. Magnetron Sputtering. *Phys. Technol.* **1988,** *19* (2), 67-75.
23. Johnson, R. W.; Hultqvist, A.; Bent, S. F. A Brief Review of Atomic Layer Deposition: from Fundamentals to Applications. *Mater. Today* **2014,** *17* (5), 236-246.
24. George, S. M. Atomic Layer Deposition: An Overview. *Chem. Rev.* **2010,** *110* (1), 111-131.
25. Leskela, M.; Ritala, M. Atomic Layer Deposition Chemistry: Recent Developments and Future Challenges. *Angew. Chem. Int. Ed.* **2003,** *42* (45), 5548-5554.
26. Simpson, T. W.; Wen, Q. Z.; Yu, N.; Clarke, D. R. Kinetics of the Amorphous $\rightarrow \gamma \rightarrow \alpha$ Transformations in Aluminum Oxide: Effect of Crystallographic Orientation. *J. Am. Ceram. Soc.* **1998,** *81*, 61-66.
27. White, C.; McHargue, C. J.; Sklad, P.; Boatner, L.; Farlow, G. Ion implantation and annealing of crystalline oxides. *Mater. Sci. Rep.* **1989,** *4* (2), 41-146.
28. Meldrum, A.; Boatner, L. A.; Weber, W. J.; Ewing, R. C. Amorphization and Recrystallization of the ABO_3 Oxides. *J. Nucl. Mater.* **2002,** *300* (2-3), 242-254.

29. Rankin, J.; Hobbs, L.; Boatner, L.; White, C. An in situ Annealing Study of Lead Implanted Single Crystal Calcium Titanate. *Nucl. Instrum. Methods Phys. Res., Sect. B* **1988,** *32* (1-4), 28-31.
30. Rankin, J.; McCallum, J. C.; Boatner, L. A. The Effect of Annealing Environments on the Epitaxial Recrystallization of Ion-Beam-Amorphized $SrTiO_3$. *J. Mater. Res.* **1992,** *7* (3), 717-724.
31. Rankin, J.; Mccallum, J. C.; Boatner, L. A. Annealing-Environment Effects in the Epitaxial Regrowth of Ion-Beam-Amorphized Layers on $CaTiO_3$. *J. Appl. Phys.* **1995,** *78* (3), 1519-1527.
32. Kuech, T. *Handbook of Crystal Growth: Thin Films and Epitaxy*, Elsevier: 2014.
33. Narayan, J.; Holland, O. W.; Appleton, B. R. Solid-Phase-Epitaxial Growth and Formation of Metastable Alloys in Ion-Implanted Silicon. *J. Vac. Sci. Technol., B: Microelectron. Process. Phenom.* **1983,** *1* (4), 871-887.
34. Csepregi, L.; Kennedy, E.; Mayer, J.; Sigmon, T. Substrate-Orientation Dependence of the Epitaxial Regrowth Rate from Si-Implanted Amorphous Si. *J. Appl. Phys.* **1978,** *49* (7), 3906-3911.
35. Reinle-Schmitt, M. L.; Cancellieri, C.; Li, D.; Fontaine, D.; Medarde, M.; Pomjakushina, E.; Schneider, C. W.; Gariglio, S.; Ghosez, P.; Triscone, J. M.*; et al.* Tunable Conductivity Threshold at Polar Oxide Interfaces. *Nat. Commun.* **2012,** *3*, 932.
36. Lee, D.; Lu, H.; Gu, Y.; Choi, S. Y.; Li, S. D.; Ryu, S.; Paudel, T. R.; Song, K.; Mikheev, E.; Lee, S.*; et al.* Emergence of Room-Temperature Ferroelectricity at Reduced Dimensions. *Science* **2015,** *349*, 1314-1317.
37. Brinkman, A.; Huijben, M.; Van Zalk, M.; Huijben, J.; Zeitler, U.; Maan, J. C.; Van der Wiel, W. G.; Rijnders, G.; Blank, D. H. A.; Hilgenkamp, H. Magnetic Effects at the Interface between Non-Magnetic Oxides. *Nat. Mater.* **2007,** *6*, 493-496.
38. Kelly, P. J.; Arnell, R. D. Magnetron Sputtering: A Review of Recent Developments and Applications. *Vacuum* **2000,** *56* (3), 159-172.
39. Wasa, K.; Kitabatake, M.; Adachi, H. *Thin Film Materials Technology: Sputtering of Compound Materials*, Springer: Heidelberg, Germany, 2004.
40. A300 Series Magnetron Sputtering Sources Installation & Operation Manual. AJA International, Inc.: 2004.
41. Wuhrer, R.; Yeung, W. Y. Effect of Target-Substrate Working Distance on Magnetron Sputter Deposition of Nanostructured Titanium Aluminium Nitride Coatings. *Scr. Mater.* **2003,** *49* (3), 199-205.
42. Guinier, A. *X-ray Diffraction in Crystals, Imperfect Crystals, and Amorphous Bodies*, Courier Corporation: 1994.
43. Bates, S.; Zografi, G.; Engers, D.; Morris, K.; Crowley, K.; Newman, A. Analysis of Amorphous and Nanocrystalline Solids from Their X-ray Diffraction Patterns. *Pharm. Res.* **2006,** *23* (10), 2333-2349.
44. Zhang, H. J.; Chen, G.; Li, Z. H. First Principle Study of $SrTiO_3$ (001) Surface and Adsorption of NO on SrTiO3 (001). *Appl. Surf. Sci.* **2007,** *253* (20), 8345-8351.
45. Holt, M.; Harder, R.; Winarski, R.; Rose, V. Nanoscale Hard X-Ray Microscopy Methods for Materials Studies. *Annu. Rev. Mater. Res.* **2013,** *43*, 183-211.
46. Winarski, R. P.; Holt, M. V.; Rose, V.; Fuesz, P.; Carbaugh, D.; Benson, C.; Shu, D. M.; Kline, D.; Stephenson, G. B.; McNulty, I.*; et al.* A Hard X-ray Nanoprobe Beamline for Nanoscale Microscopy. *J. Synchrotron Radiat.* **2012,** *19*, 1056-1060.
47. Kirz, J. Phase Zone Plates for X Rays and the Extreme UV. *JOSA* **1974,** *64* (3), 301-309.

48. Feng, Y.; Feser, M.; Lyon, A.; Rishton, S.; Zeng, X. H.; Chen, S.; Sassolini, S.; Yun, W. B. Nanofabrication of High Aspect Ratio 24 nm X-ray Zone Plates for X-ray Imaging Applications. *J. Vac. Sci. Technol., B* **2007,** *25* (6), 2004-2007.

Chapter 2: Distinct nucleation and growth kinetics of amorphous $SrTiO_3$ on (001) $SrTiO_3$ and SiO_2/Si: A step toward new architectures

2.1 Introduction

Solid-phase crystallization can be applied to create complex-oxide thin films in complex geometries by crystallizing layers on a patterned 3D substrate, part of which is composed of crystalline seeds.[1-2] The eventual use of crystallization to create complex geometries requires understanding the propagation of a crystal growth front from a crystalline seed and nucleation either within the amorphous material or at interfaces that do not act as crystalline seeds.

This chapter describes the crystallization kinetics of amorphous $SrTiO_3$ (STO) layers deposited on planar single-crystal (001) STO substrates that can serve as crystalline seeds. The results of crystallization experiments using STO substrates contrast with the crystallization kinetics of STO on amorphous substrates that do not act as crystalline seeds. The amorphous surfaces employed in this study are widely commercially available SiO_2/(001) Si substrates.

STO was selected in this study because of the reasons introduced in Chapter 1. The crystallization of STO on single-crystal (001) STO substrates occurs through SPE, the motion of a smooth amorphous/crystalline interface toward the surface.[3] The kinetics of SPE in STO have been probed in amorphous layers created by ion implantation,[3-4] sputter deposition,[5] and pulsed-laser deposition,[6] revealing that interface velocities are thermally activated and that a planar interface is preserved. The crystallization mechanisms of the amorphous STO layers created by different methods on (001) STO are the same.

Although the amorphous STO layers created by different methods on (001) STO all crystallize by SPE, previous studies show that the rates of crystallization of STO on (001) STO can be affected by many effects including the creation method of amorphous STO layers, the annealing temperature range, the annealing environment and the possible impurities in the amorphous layers.

A key feature of the previous studies of the crystallization of amorphous STO layers is that the overall rate of crystallization depends slightly on the methods that have been used to create the amorphous layers. For example, amorphous STO layers created by ion implantation on (001) STO can fully crystallize by SPE at relatively lower temperatures of 270 – 550 °C.[3] Amorphous STO layers created by sputter deposition on (001) STO, however, can only fully crystallize by SPE at relatively higher temperatures of 400 – 800 ºC.[5] The annealing environment of both studies were in air.[3,5] The crystallization kinetics are different partially because of the different amorphous/crystalline interface microstructures in the different methods.[5] This variation in the rate of crystallization leads to some uncertainty regarding the velocity of interfaces between the amorphous layers and the substrates.

The crystallization processes of amorphous STO on (001) STO are more complex at a temperature higher than 800 ºC, where motion of the amorphous/crystalline interface by SPE is accompanied by nucleation of crystals in the region of the film far from the interface.[5] The annealing environment also plays an important role in determining the crystallization rates of amorphous STO on (001) STO.[4,7-8] The crystallization rates of amorphous STO created by ion implantation at temperatures of 265 to 430 ºC increase by more than one order of magnitude when the annealing environment includes water vapor, because hydrogen provided by the water vapor

serves as a catalyst in the crystallization of STO.[4] The activation energy required for the crystallization of STO, however, does not change in the different annealing environments.[4,9]

A previous crystallization study of another oxide system Al_2O_3 shows that the impurities in the amorphous layers can also affect the crystallization rates.[9] For example, the presence of Fe in the amorphous Al_2O_3 film increases the crystallization rates of Al_2O_3 significantly.[9]

In contrast to the SPE growth of STO on single-crystal STO, much less is known about crystal nucleation process or rates of nucleation of amorphous STO on amorphous SiO_2/Si substrates that do not provide crystalline templates for epitaxial growth of STO. The rates of nucleation of amorphous STO on SiO_2/Si were studied at the annealing temperatures at which STO on single-crystal STO crystallizes epitaxially by SPE. Because many effects discussed above can affect the rates of nucleation and growth, a systematic study of comparing the rates of nucleation and growth on the two substrates is required, with the other conditions the same.

The amorphous-to-crystalline transformation is dramatically different on the (001) STO and SiO_2/Si substrates, as shown schematically in Figure 2-1. A series of structural studies demonstrated that the crystallization of amorphous STO on a (001) STO substrate occurred by SPE, shown in Figure 2-1(a). Starting from an as-deposited amorphous STO layer on a (001) STO substrate, indicated by step (i), the crystallization occurs through the motion of the amorphous/crystalline interface toward the sample surface as shown in steps (ii) and (iii). The thickness of the amorphous layer gradually decreases. The amorphous STO layer is eventually fully crystallized and transforms into an epitaxial STO layer on the (001) STO substrate as shown in step (iv). In contrast, Figure 2-1(b) shows the different crystallization process of amorphous STO on a SiO_2/Si substrate, which proceeded by nucleation and growth. With an as-deposited amorphous STO layer on a SiO_2/Si substrate shown in step (i), the amorphous structure with a

probably different arrangement is persistent for a certain time before nucleation of STO crystals, described by step (ii). Step (iii) shows the polycrystalline nucleation and growth of STO crystals inside the amorphous STO layer. The amorphous STO layer eventually transforms into a polycrystalline STO layer on the SiO_2/Si substrate as shown in step (iv).

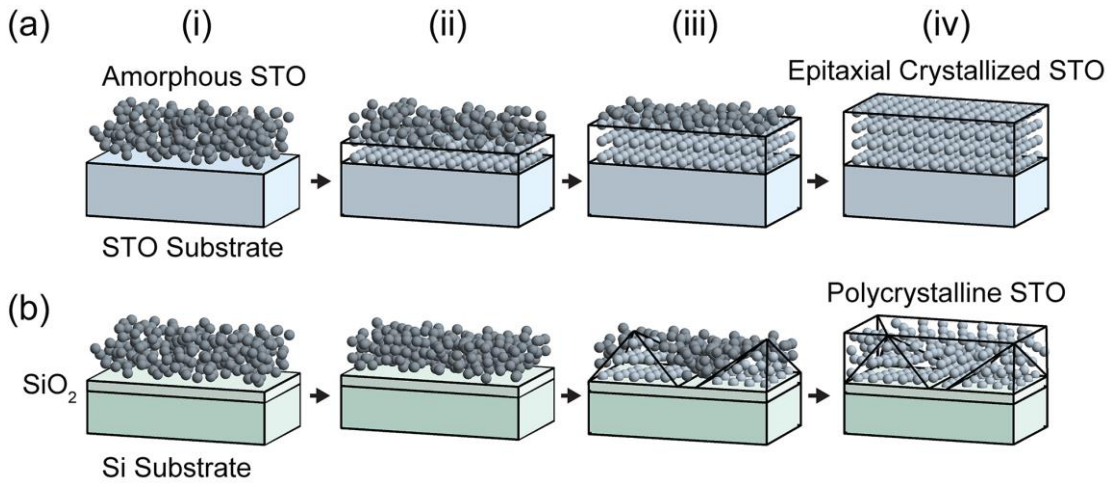

Figure 2-1. (a) Schematic of the crystallization of amorphous STO on (001) STO substrates by SPE: (i) as-deposited amorphous STO layer, (ii and iii) crystallization of STO through the motion of the amorphous/crystalline interface toward the surface, and (iv) fully crystallized epitaxial STO thin film. (b) Schematic of the crystallization of amorphous STO on SiO_2/(001) Si substrates by nucleation and growth: (i) as-deposited amorphous STO layer, (ii) persistence of the amorphous structure, (iii) polycrystalline nucleation and growth of STO crystals, and (iv) fully crystallized polycrystalline STO thin film.

The crucial insights from this study are that there is a difference in the crystallization kinetics of amorphous STO thin films deposited on the two substrates and the scaling of these rates is favorable for the formation of epitaxial crystals in complex geometries. The temperature dependence of the nucleation and growth processes for STO crystals allows the effective activation energy for nucleation of crystalline STO from an amorphous STO layer to be measured. The activation energy for nucleation is higher than the activation energy for the motion of the amorphous/crystalline interface. It thus is particularly important to consider crystallization at low temperatures, approximately 450 °C in the present study, where the rates of crystal growth for

STO on STO and rates of nucleation for STO on SiO_2/Si are significantly different and favor the growth of large epitaxial STO crystals even in the presence of interfaces with SiO_2/Si.

2.2 Nucleation on amorphous substrates

2.2.1 Nucleation process

The nucleation process of STO on SiO_2/Si hasn't been reported in the literature. Studies of nucleation processes of other simple amorphous oxides indicate that the nucleation involves both atomic-scale and larger-scale processes that are different from the SPE growth process. Molecular dynamics simulations of another oxide material Al_2O_3 show that nucleation involves a set of atomic-scale processes, in which the local structure with a short-range order rearranges into the metal-oxygen coordination favorable for crystal formation.[10] The building block of amorphous Al_2O_3 is mainly composed of slightly distorted $(AlO_4)^{5-}$ tetrahedron with a short-range order.[10-11] This calculated amorphous structure is similar to the surface structure of the metastable crystalline phase γ-Al_2O_3 at room temperature.[10] Al atoms in the stable crystalline phase α-Al_2O_3 are octahedrally coordinated.[12] This might be the reason why amorphous Al_2O_3 transforms to γ-Al_2O_3 phase first before evolving into α-Al_2O_3 phase in the crystallization process of amorphous Al_2O_3.[10] Larger-scale processes within the amorphous form can also have an important role in the nucleation process. The evolution of TiO_2 nanostructures in ALD follows a path from amorphous layers to amorphous particles to metastable crystallites and ultimately to stable crystalline forms.[13] The atomic-scale processes in nucleation thus differ from the atomic-scale processes in the SPE growth involving the motion of amorphous/crystalline interface, and can be expected to have a

different activation energy. The difference in the temperature dependence of nucleation and crystal growth can be exploited to find regimes favoring crystal growth and limiting nucleation.

2.2.2 Nucleation kinetics

The kinetics of nucleation process is particularly important in determining the annealing conditions under which STO polycrystals do not nucleate at locations far from the amorphous/crystalline interface. In classical nucleation theory, the nucleation process is the formation of crystals with super-critical size from crystalline clusters with sub-critical size.[14] When a crystal has a size smaller than the critical size, a further increase of the size of the particle requires more energy. When a crystal has a size larger than the critical size, the further increase of the size of the particle will release energy.[15] In the process of forming a nuclei with a size greater than the critical size, the temperature dependence of the rates of nucleation can be described by an Arrhenius equation: $k(T) = k_0 \exp\left(-\frac{E}{k_B T}\right)$ in which k_0 is a temperature-independent pre-exponential factor and E is the effective activation energy for nucleation, k_B is the Boltzmann constant and T represents temperature.[15]

In a system with finite size, the probability *P* that one nucleation event occurs within time *t* in volume *V* is:[16]

$$P = 1 - exp\ (-kV\ t)$$

Equation 2-1

Equation 2-1 can be rewritten as:

$$t = \frac{\ln\left(\frac{1}{1-P}\right)}{V}\frac{1}{k}$$

Equation 2-2

Here k is the nucleation rate, which has the Arrhenius temperature dependence mentioned above. The nucleation of the crystalline phase occurs when a large number of nuclei have formed to reach a certain probability P_0. From Equation 2-2, because $\frac{ln\left(\frac{1}{1-P}\right)}{V}$ is a positive number, the time t required to reach a given probability P_0 is proportional to $1/k$. The reciprocal of the time $1/t$ is thus proportional to k. Because k follows the Arrhenius temperature dependence, $1/t$ required for nucleation is also thermally activated with an Arrhenius temperature dependence. In our analysis below, for the nucleation process of STO on SiO_2/Si, the nucleation time is denoted as t^*. The reciprocal of the nucleation time ($1/t^*$) thus has an Arrhenius temperature dependence.

2.3 Experimental details

STO substrates (Shinkosha Co., Ltd.) were purchased with one side polished. TiO_2 terminated-surfaces were prepared before growth by an annealing and deionized (DI) water treatment.[17-18] Substrate preparation employed a three-step process that consisted of annealing at 1000 °C for 1 h, sonicating the substrates in DI water to dissolve superficial strontium oxide that resulted from the first anneal, and annealing again at 1000 °C for 1 h. The STO substrates were then sonicated in acetone, isopropyl alcohol (IPA), methanol and DI water, for 2 min in each solvent. Unlike the STO substrates, the (001) Si substrates were not subjected to additional processing steps prior to solvent cleaning. This preserved the native SiO_2 layer on which amorphous STO was deposited.

Amorphous STO films were deposited by on-axis radio-frequency magnetron sputter deposition onto substrates held at room temperature, conditions that are expected to yield amorphous layers.[5,19] Prior to depositing the amorphous STO films, the sputter-deposition vacuum chamber was evacuated to 2×10^{-6} Torr. STO layers were grown at a total pressure of 18 mTorr

with an $Ar:O_2$ pressure ratio of 9:1. STO was deposited at a rate of 15 nm h^{-1} to total thicknesses of approximately 60 nm. The precise thickness of each as-deposited film was measured using X-ray reflectivity (XRR).

During the crystallization process, samples were inserted into a preheated three zone tube furnace (Lindberg/MPH). Separate experiments were conducted to know the heating rate of the sample. A thermocouple was used to measure the temperature of the surface of a Si wafer with the thermocouple wire attached to the surface of the wafer. The Si wafer was put in the middle zone of the furnace where other samples were heated. The wafer reached a temperature 50 °C below the nominal temperature in less than 300 s. A temperature 5 °C less than the nominal temperature was reached in 600 s. The shortest reported time at 550, 650 and 600 °C is 300 s, thus there is some uncertainty in the reported temperature for these samples, which we have not explicitly considered in the analysis. All annealing and crystallization experiments were conducted in still air.

The transmission electron microscopy (TEM) cross-sectional specimens were prepared with a focused ion beam lift-out process. An electron-beam assisted carbon protective layer was deposited on the sample surface before its exposure to the Ga ion beam in order to prevent surface damage. High-resolution TEM imaging was conducted using a Tecnai TF-30 transmission electron microscope operated at 300 keV.

Grazing-incidence X-ray diffraction measurements were conducted for STO on STO and STO on SiO_2/Si to study the amorphous STO scattered X-ray intensities. The experimental details were introduced in Section 1.4 of Chapter 1. The crystallization kinetics of STO on STO and SiO_2/Si substrates were compared by analyzing the time evolution of the X-ray scattering intensity at a series of annealing temperatures. Integrating the 2D detector images along the scattering ring

azimuthal angle provide measurements of the scattered intensity as a function of 2θ. The total X-ray intensity scattered from amorphous STO was obtained by the following steps: (i) subtracting the scattering pattern of a bare substrate and (ii) integrating the difference over the 2θ range from 24° to 30°. The upper limit of integration was set at 30° to avoid the (110) STO peak at 32° in thin films deposited on SiO_2/(001) Si.

XRR data were collected using a Panalytical X'Pert MRD with monochromatic Cu Kα1 X-ray radiation at a wavelength of 1.5406 Å. XRR data shown in Figures. 2-5 and 2-6 were interpreted using the interdiff model of the GenX software package.[20] A simpler interpretation of XRR results based on a measurement of the mean of the fringe spacings was used to determine the initial thickness in growth rate results derived from X-ray scattering in Figure 2-4.

2.4 Crystallization on different surfaces

2.4.1 Distinct crystallization mechanisms

The as-deposited STO layers on both STO and SiO_2/Si substrates exhibited grazing-incidence X-ray scattering patterns consistent with an amorphous thin film, as in Figures 2-2(a) and (b). The slight difference in the intensities of the scattering patterns in Figures 2-2(a) and (b) arises from the different X-ray incident angles, and thus illuminated volumes, for STO on STO (incident angle 3.2º) and STO on SiO_2/Si (1.4º). The crystallization of STO on the (001) STO substrate results in the disappearance of the amorphous scattering signal without the appearance of polycrystalline diffraction rings. Figure 2-2(c) shows the X-ray scattering pattern of the same STO film shown in Figure 2-2(a) following annealing at 650 °C for 5 min, a temperature and duration yielding full crystallization of the film.

TEM provides further evidence of the crystallization of STO on STO by SPE. The TEM measurements were conducted by Dr. Yingxin Guan during her work as a PhD student in Professor Thomas Kuech's group at University of Wisconsin-Madison. Annealing an as-deposited amorphous film at 600 ºC for 32 min results in full crystallization, as shown by the cross-sectional high-resolution TEM images in Figure 2-3(a). The images were obtained from a <100>-oriented cross-sectional specimen and show lattice fringes with spacing that is consistent with <001> oriented STO. The image with a larger field of view includes the sample surface, at which there is no interlayer between the amorphous carbon and the crystallized STO layer, indicating that the STO layer has fully crystallized under this condition. The orientation of the lattice fringes is constant throughout the entire crystallized layer and identical to the substrate. These observations are consistent with the expectation that the layer is epitaxial and that the crystallization of STO on STO occurs via SPE.

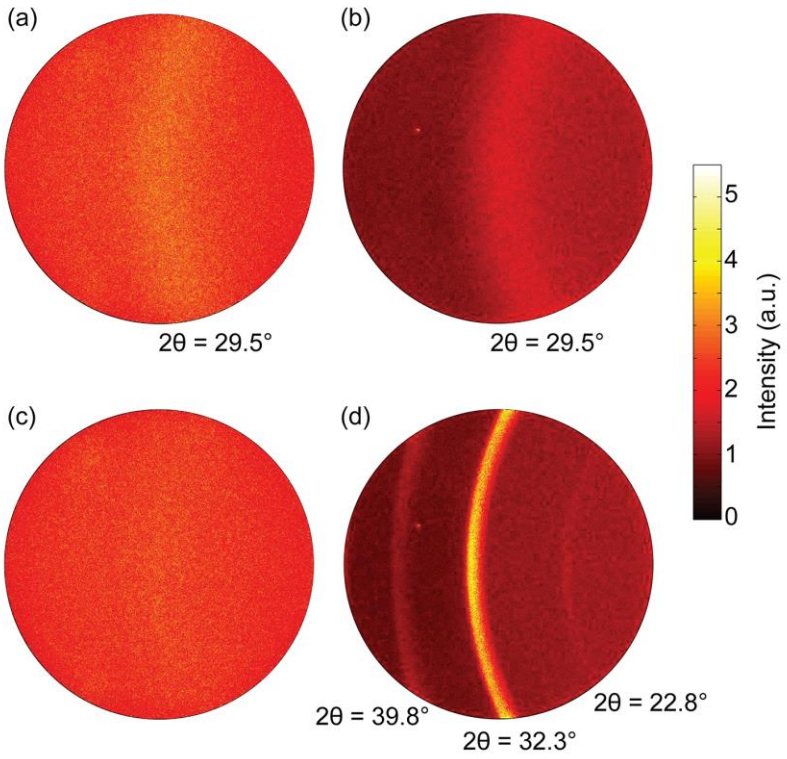

Figure 2-2. Grazing-incidence X-ray scattering patterns of (a) amorphous STO on (001) STO and (b) amorphous STO on SiO_2/(001) Si, with a ring of scattering from amorphous STO at $2\theta = 29.5°$. Scattering patterns of crystallized STO on (c) (001) STO and (d) SiO_2/(001) Si. Rings of powder diffraction intensity appear 2θ angles of 22.8°, 32.3°, and 39.8° arising from the (100), (110), and (111) reflections of polycrystalline STO appear following crystallization on SiO_2/(001) Si.

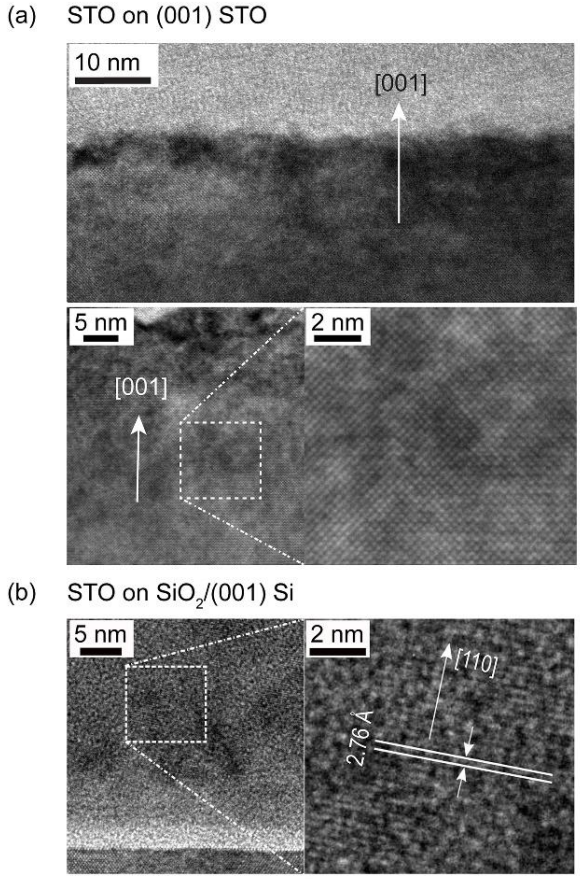

Figure 2-3. High-resolution TEM micrographs of fully crystallized STO films on (a) (001) STO and (b) SiO_2/(001) Si substrates.

For STO on SiO_2/(001) Si, heating transforms the amorphous layer into a nanocrystalline microstructure. Figure 2-2(d) shows the X-ray scattering pattern of a crystallized STO thin film after annealing at 650 °C for 18 min, exhibiting a series of powder diffraction rings arising from (100), (110) and (111) reflections of STO. The integrated intensities of the (100) and (111) reflections are 3.3% and 19.8% of the intensity of the (110) peak, respectively. The peak positions and ratios of peak intensities agree with the powder X-ray diffraction pattern of STO,[21] indicating

that the STO crystals form on SiO_2/(001) Si in random orientations. The (100), (110) and (111) reflections have angular widths of 0.8°, 1.2°, and 1.5°, respectively, giving crystal sizes of 11 nm, 7 nm and 6 nm, respectively, based on Scherrer's formula. The X-ray reflections of STO thin films on SiO_2/(001) Si crystallized at lower temperatures, from 450 °C to 600 °C, have similar angular widths and relative intensities. The 10 nm size of the STO crystals is much smaller than the total film thickness of approximately 60 nm. The small STO crystal size, even after the completion of crystallization indicates that nucleation for STO on SiO_2/(001) Si occurs within the volume of the film and is not limited to the free surface or to the STO/SiO_2 interface.

The crystallized STO layer on SiO_2/(001) Si substrate is shown in the high-resolution TEM image in Figure 2-3(b) for a STO layer with an initial thickness of 61 nm heated to 600 °C for 36 min. The image was obtained from a Si <110>-oriented cross-sectional specimen. The spacing of the fringes is 2.76 Å, which matches the spacing of {110} planes in STO and is indicative of the local orientation of the crystallized STO. A high-resolution image of one STO nanocrystal within the layer exhibits lattice fringes with a misorientation of 11° with respect to the Si substrate. Other domains containing {110} crystal planes, with different angular orientations with respect to Si, were also observed in the high-resolution TEM analysis. Figure 2-3(b) shows a high-resolution TEM image in which a STO single lattice orientation is apparent across the entire image. The crystalline domain size in Figure 2-3(b) is on the order of tens of nanometers, which is larger than the mean value of the crystal size, determined from the widths of STO X-ray reflections. The difference between crystal sizes estimated with these methods can arise from inhomogeneity in the grain size of the polycrystalline STO.

2.4.2 Distinct crystallization kinetics

Insight into the kinetic mechanism of crystallization can be obtained by examining the structure of partially crystallized STO layers. The evolution of the scattered X-ray intensity for an amorphous STO layer on (001) STO for a series of crystallization times at 600 °C is shown in Figure 2-4(a). The data shown in Figure 2-4(a) were acquired in a series of separate heating steps, each of which was followed by X-ray scattering characterization. The integrated intensity of the scattering feature arising from amorphous STO is shown as a function of heating time for annealing temperatures from 450 °C to 650 °C in Figure 2-4(b). The intensity of scattering arising from amorphous STO decreases continuously with increasing annealing time.

The intensity in the angular range of scattering from the amorphous layer is slightly higher than the background intensity even at long annealing times, an effect that is accounted for in the analysis below. We hypothesize that this difference, which is on the order of 10-30% of the total intensity of the scattering from the amorphous layer, may arise from small differences in the run-to-run alignment of the sample on the X-ray diffractometer, the formation of very small crystallites, or scattering from surface contamination accumulated during processing.

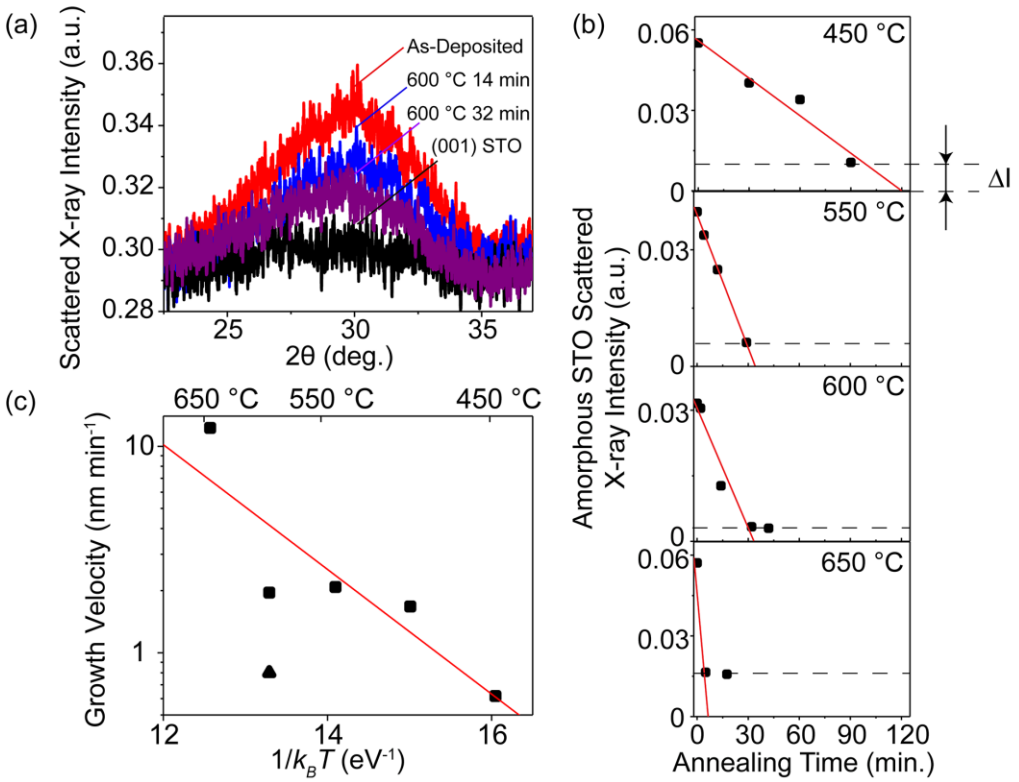

Figure 2-4. (a) Grazing-incidence X-ray scattering intensity for an STO film deposited on (001) STO and annealed at 600 °C in a series of steps with the indicated total duration. The curves represent as-deposited (red), partially crystallized (blue), and fully crystallized (purple) layers. Scattering intensity from the bare STO substrate (black) is shown for comparison. (b) Integrated X-ray intensity from the amorphous STO as a function of annealing time at temperatures of 450 °C, 550 °C, 600 °C, and 650 °C. The lines indicate the fit used to determine the crystalline/amorphous interface velocity at each temperature. (c) Growth velocities determined using the data shown in (b) (squares) and growth velocity at 600 °C determined using XRR (triangle). The line is a fit to determine the effective activation energy.

The growth velocity for crystallization of STO on (001) STO via SPE was determined using the rate of decrease of the scattered X-ray intensity from the amorphous layer. The X-ray intensity scattered from amorphous STO, I, can be modelled as $I = C\,x(t) + \Delta I$. Here C is a constant set by the incident X-ray intensity, the scattering per unit volume from the amorphous layer, detector parameters, and beam footprint on the sample surface; $x(t)$ is the thickness of the amorphous layer at time t, and ΔI is the non-zero intensity of X-rays scattered from the fully crystallized film. The velocity v of the amorphous/crystalline interface is determined using $v =$

$\frac{dx}{dt} = \frac{1}{C}\frac{dI}{dt}$. The constant C can be obtained by comparing the initial and final states, $C = \frac{I_0 - \Delta I}{x_0}$, where x_0 is the initial thickness of the amorphous STO film and I_0 is the initial scattered intensity of the as-deposited film. The growth velocity, v, is then:

$$v = \frac{dI}{dt}\frac{x_0}{I_0 - \Delta I}$$

Equation 2-3

The growth velocities found by applying Equation 2-3 are plotted as a function of temperature in Figure 2-4(c). Velocities range from 0.6 nm min^{-1} at 450 °C to 12.3 nm min^{-1} at 650 °C. The velocity of 1.7 nm min^{-1} at 500 °C has the same order of magnitude as the value of 3.7 nm min^{-1} that can be inferred from the previously reported time required to crystallize a sputter-deposited STO film at the same temperature.[5] The differences between the rate reported here and the value from the literature are discussed in more detail below.

Previous studies of SPE of STO, as well as Si, SiGe, and other semiconductors have found that the growth velocity at temperature T can be described by an Arrhenius temperature dependence given by $v(T) = v_0 e^{-E_a/k_B T}$.[3,20] Here E_a is the effective activation energy for the processes determining the velocity, v_0 is a velocity prefactor. A fit of this expression to the growth velocities reported in Figure 2-4(c) for the temperature range from 450 °C to 650 °C gives an activation energy of 0.7 eV.

The activation energy for the interface velocity reported here is in reasonable agreement with the value of 0.77 eV observed for the crystallization of amorphous STO produced by ion implantation.[3] Other reported activation energies range from 1.0 eV in an H_2O atmosphere to approximately 2.1 eV in vacuum.[4] The activation energy for the SPE growth of STO on (001) STO depends on the gas ambient during annealing and the sample preparation method. Hydrogen,

provided by the dissociation of water molecules at the surface, penetrates the amorphous layer to the amorphous-crystalline interface to increase the crystallization rate of amorphous STO. The crystallization velocity increases at a higher concentration of diffusing hydrogen at the interface and the process requires a lower activation energy.[4,8] The amorphous STO films deposited by sputtering have different crystallization rates than the films prepared by ion implantation at a few annealing temperatures.[5] The differences in activation energy and velocity reported here may thus arise from sensitivity to the ambient atmosphere during crystallization or the different sample preparation method.

XRR studies provide further support for the conclusion that the crystallization of STO on (001) STO occurs through the motion of a planar amorphous/crystalline interface by SPE. Figure 2-5(a) shows XRR curves for an amorphous STO layer on a STO substrate for a series of annealing times at 600 °C. The XRR curve fit employed a two-layer model consisting of an amorphous STO layer on a uniform underpinning layer consisting of the STO substrate and crystallized STO layer. The densities of amorphous STO and crystalline STO were constrained in the range 4.2 ± 0.1 g cm^{-3} and at 5.1 g cm^{-3}, respectively, based on their literature values.[4,15,22] Thickness and root-mean-square (rms) roughness parameters for reflectivity curve fits are shown in Table 2-1. It is apparent from the XRR study that the amorphous layer thickness decreases continuously as a function of time during crystallization, as in Figure 2-5(b).

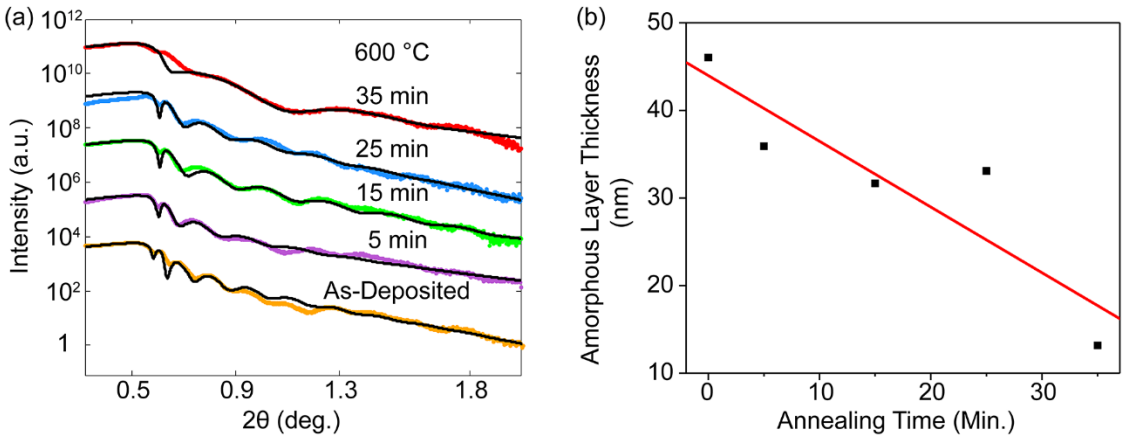

Figure 2-5. (a) XRR measurements of as-deposited amorphous STO on STO (orange) and after annealing at 600 °C for 5 min (purple), 15 min (green), 25 min (blue), and 35 min (red). Black lines show calculated reflectivity curves using the parameters given in the text. The intensity of the annealed samples has been shifted vertically to allow the curves to be distinguished. (b) Amorphous STO layer thickness, derived from the fringe spacing in XRR data, as a function of annealing time at 600 °C.

The velocity determined from the rate of amorphous/crystalline interfaces motion in Figure 2-5(b) is 0.8 nm/min, which is slightly less than the value deduced from the X-ray scattering data (1.9 nm/min), but consistent with the overall temperature dependence of the crystallization velocity. The discrepancy in crystallization front velocities for these two samples can be explained by a combination of random and systematic errors: temperature variation by several °C in the furnace can result in a velocity variation of 0.5 nm/min by applying the Arrhenius relationship, and the magnitude of ΔI, as discussed earlier with respect to Equation 2-3, can influence the velocity as much as 0.2 nm/min. The continuously decreasing thickness and the constant roughness of the STO interface are signs of crystallization at a planar amorphous/crystalline interface.

Table 2-1. Thickness and interface roughness determined from XRR measurements during the crystallization of amorphous STO on a crystalline STO substrate.

STO/STO annealing conditions	Amorphous STO layer thickness (nm)	Amorphous STO layer rms roughness (nm)	Substrate/crystallized STO interface rms roughness (nm)
As-deposited	46.04	1.06	2.38
600 °C 5 min	35.92	0.74	2.55
600 °C 15 min	31.67	1.07	1.72
600 °C 25 min	33.07	1.24	2.46
600 °C 35 min	13.17	0.66	2.20

The crystallization of STO on SiO_2/(001) Si lacks the crystalline template provided by the STO substrate and instead occurs by a nucleation and growth process that results in a nanocrystalline microstructure. The time dependence of the intensity of X-ray scattering from amorphous STO layers on SiO_2/(001) Si at an annealing temperature of 600 °C is shown in Figure 2-6(a). Intensity rings appear in the diffraction pattern after annealing for 16 min, indicating the formation of randomly oriented polycrystalline STO and marking the point when a large number of nuclei have formed at this temperature. The nucleation time depends on the temperature of the crystallization process.

XRR studies of crystallized STO on SiO_2/(001) Si reveal the changes in the density of STO that accompany the crystallization process. Figure 2-6(b) shows XRR curves of a STO layer deposited on SiO_2/(001) Si and annealed at 600 °C for different durations. The XRR fits for STO on SiO_2/(001) Si were performed with a three-layer model consisting of the STO film, native SiO_2, and Si substrate. The densities of the SiO_2 and Si were set at 2.196 g cm^{-3} and 2.329 g cm^{-3}, respectively. The density of partially crystallized STO film was allowed to vary between the densities of amorphous and crystalline STO.

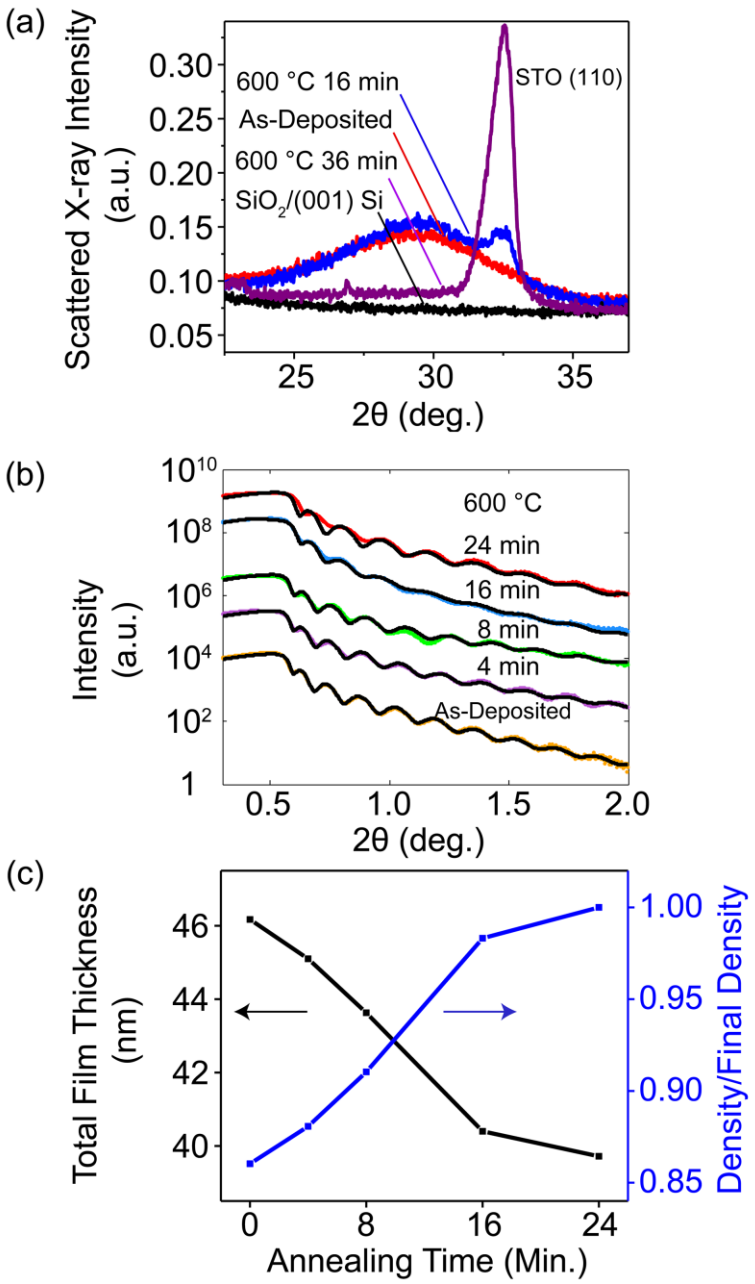

Figure 2-6. (a) Grazing-incidence X-ray scattering intensity for an STO layer deposited on SiO_2/(001) Si substrate and annealed at 600 °C for different time periods. The curves represent as-deposited (red), partially crystallized (blue), and fully crystallized (purple) films. (b) XRR measurements of an as-deposited amorphous STO (orange), and the same sample annealed at 600 ℃ for 4 min (purple), 8 min (green), 16 min (blue), and 24 min (red). Fits using the parameters given in Table 2-2 are shown as black lines. (c) Film thickness and density as a function of annealing time at 600 ℃.

The thickness and rms roughness derived from the fits are shown in Table 2-2. The XRR study shows that the STO thickness decreases upon crystallization, from 46 nm to 40 nm, as shown in Figure 2-6(c), indicating that the as-deposited density of amorphous STO is 87% of the density of crystalline STO. The observed change in density upon crystallization is consistent with reported densities of 4.2 ± 0.1 g cm^{-3} and 5.1 g cm^{-3} for amorphous and crystalline STO, respectively.[4,22-23] The XRR results thus indicate that a volume contraction of on the order of 13% can be expected during the crystallization of amorphous STO thin films.

Table 2-2. Thickness and interfaces roughness determined from XRR measurements during the crystallization of amorphous STO on an SiO_2/(001) Si substrate.

STO/SiO_2/ (001) Si annealing conditions	**Total thickness of polycrystalline and amorphous STO layers (nm)**	**STO roughness (nm)**
As-Deposited	46.17	0.79
600 °C 4 min	45.10	0.13
600 °C 8 min	43.63	0.10
600 °C 16 min	40.40	0.74
600 °C 24 min	39.72	0.77

2.5 Quantification of the distinct crystallization kinetics

The role of nucleation in the crystallization of STO on SiO_2/Si can be quantified by considering the nucleation time t^*, which was defined from the fundamental perspective of nucleation theory in Section 2.2.2 of this Chapter. Experimentally t^* can be measured by defining it to be the longest time at which the X-ray intensity scattered from amorphous STO is equal to its as-deposited value. The value of t^* for STO on SiO_2 is sufficiently long that at low temperatures it exceeds the total crystallization time of STO on STO substrates. At 450 °C, for example, as in Figure 2-7(a), t^* is more than 14 h whereas the crystallization of STO on STO (001) is completed within 1.5 h. The nucleation time at 650 °C is less than the minimum practical annealing time, and thus was not measured.

In addition to the eventual decrease in the scattering from amorphous STO due to crystallization, there is also a reproducible increase in the scattered intensity from the amorphous layer of approximately 10% at short times in Figure 2-7. The increase of the intensity is hypothesized to arise from a rapid rearrangement of the amorphous structure at the initial stages of heating. There is also a slight narrowing of the angular distribution of intensity, as can be seen in the difference between the as-deposited and 16 min scattering patterns in Figure 2-6(a). Annealing-induced changes in the amorphous scattering pattern were observed in tin-doped indium oxide (ITO) amorphous oxide thin films and the changes were linked to a unit-cell-scale rearrangement of the In-O bonding.[24] Changes in electronic transport parameters were also observed following heating of ITO films and further indicate the structural rearrangement.[25] We note, however, the rearrangement of the amorphous structure in ITO leads to large angular shifts of the amorphous scattering pattern, which are not observed here. Amorphous STO incorporates multiple metal ions, and it is hypothesized that an unknown local ionic rearrangement leads to the sharpening observed in Figure 2-6(a) and the increase in amorphous scattering intensity observed at short times in Figure 2-7. Further experiments such as pair distribution function (PDF) based on synchrotron X-ray radiation can be conducted to understand the changes of the amorphous STO scattering pattern observed here. The subtle differences of the local structures of the amorphous thin films at early stages of annealing can be discerned with PDF analysis.[26-27]

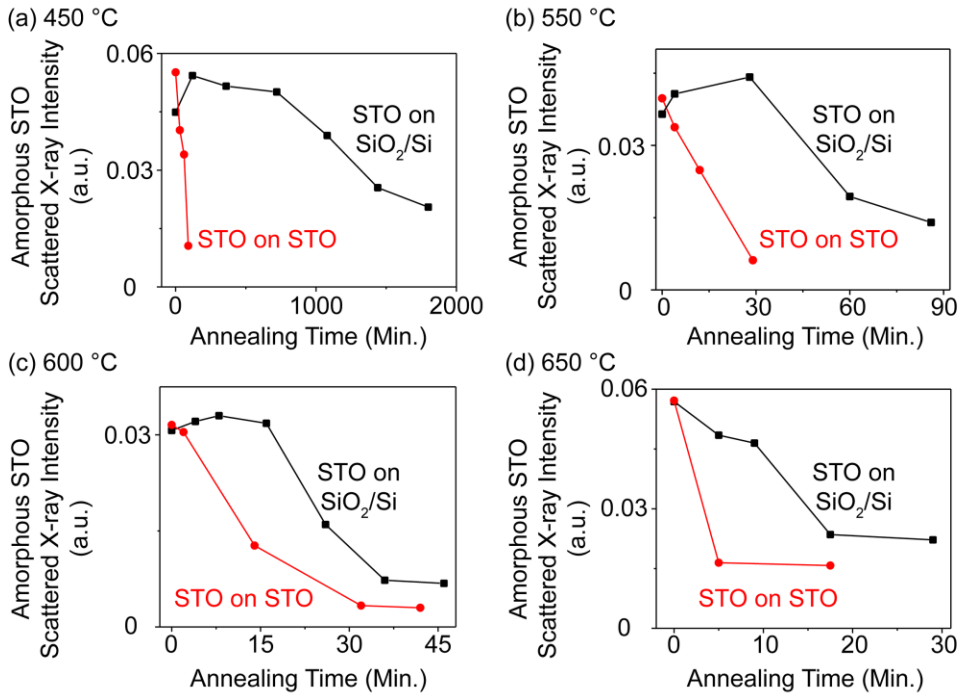

Figure 2-7. Time dependence of the X-ray intensity scattered from amorphous STO for STO on SiO_2/(001) Si (black) and STO on (001) STO (red) for annealing temperatures of (a) 450, (b) 550, (c) 600, and (d) 650 ℃.

As discussed in Section 2.2.2 of this Chapter, the reciprocal of the nucleation time ($1/t^*$) for STO on SiO_2/Si can be expressed using an Arrhenius temperature dependence: $\frac{1}{t^*} = \frac{1}{t_0^*} e^{-E_b/k_B T}$. The use of the Arrhenius equation to describe the thermally activated nucleation process has previously been applied in the crystallization of glassy materials.[15] Here $1/t_0^*$ is a temperature-independent constant and E_b is the activation energy for nucleation. The variation of the experimentally observed t^* with temperature is shown in Figure 2-8(a). The activation energy for nucleation obtained by fitting the expected temperature dependence to the experimentally observed nucleation time is 1.4 eV. The difference between the activation energies for crystal growth and nucleation is a key effect that allows us to find a window in which crystal growth proceeds over long distances without significant nucleation.

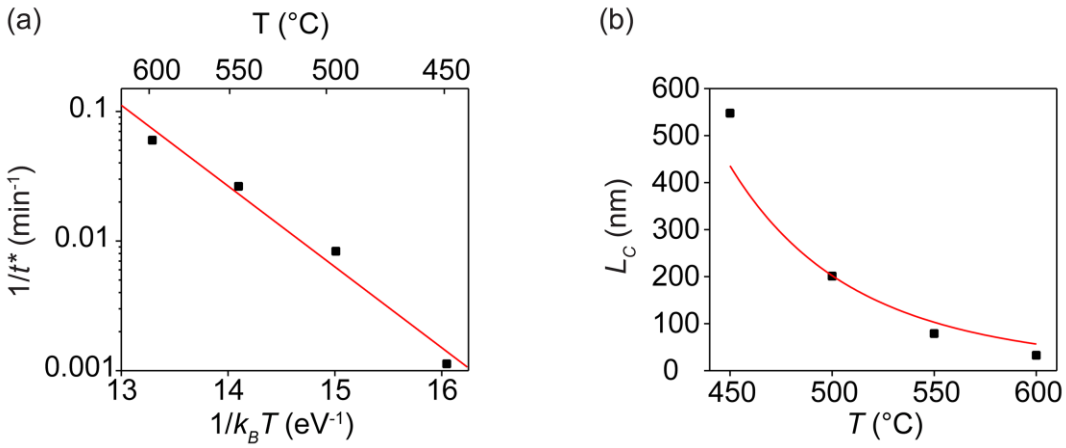

Figure 2-8. (a) Nucleation time for STO on SiO_2/(001) Si as a function of annealing temperature. The line is a fit to determine the effective activation energy. (b) Maximum STO crystallization distances before nucleation (L_C) as a function of temperature. Points are the product of measured interface velocity and nucleation time, v and t^*. The temperature dependence predicted based on the measured activation energies of v and t^* is shown as a solid line.

This relatively long nucleation time and high activation energy for nucleation of crystalline STO on SiO_2 provides the insight required to form STO and other complex oxides in sophisticated geometries. In such cases, crystalline STO can act as a crystalline template and materials with other compositions, such as SiO_2 can serve as a mask. As is apparent from the long nucleation time in Figure 2-7, SiO_2 can form interfaces with amorphous STO without providing nucleation sites for crystallization.

The key parameter for the process of guiding the path of crystallization using SiO_2 as a mask is the maximum film thickness or distance over which the amorphous STO can crystallize by SPE before the nucleation of crystalline STO occurs away from the moving interface. This maximum crystallization distance, L_C, can be expressed as $L_C=vt^*$, where v is the velocity of the amorphous/crystalline interface due to SPE and t^* is the nucleation time. The values of L_C at annealing temperatures in the range of this study are plotted in Figure 2-8(b) based on values of v and t^* determined from STO on (001) STO and STO on SiO_2/(001) Si, respectively. As would be

expected from the difference in the activation energies of the two processes, the maximum crystallization distance by SPE L_C covered before nucleation increases as the temperature decreases. The largest L_C is in the present study is achieved at the relatively low temperature of 450 °C. Figure 2-8(b) indicates that for temperatures above 600 °C the crystallization lengths that can be achieved are less than 50 nm, lower than the thickness of as-deposited amorphous layers. Crystallizing amorphous films by SPE at temperatures above 600 °C can lead to highly defective crystalline layers due to nucleation away from the amorphous/crystalline interface. The high-temperature regime of Figure 2-8(b) is thus consistent with previous observations that the crystallized STO films become highly defective at high temperatures due to nucleation away from the crystallization interface.[5] L_C is a function of v and t^*, which are both thermally activated, and can be expressed as:

$$L_C = vt^* = v_0 t_0^* e^{-(E_a - E_b)/k_B T} = v_0 t_0^* e^{-\Delta E/k_B T}$$

Equation 2-4

Figure 2-8(b) shows a plot of the measured product vt^*, illustrating that the maximum crystallization distance at different annealing temperatures can be estimated using Equation 2-4.

The increase in the crystallization distance L_C at low temperatures, apparent in Figure 2-8(b), shows that flash heating or other rapid thermal processing techniques at high temperatures are not appropriate to create thick single-crystalline layers of STO by suppressing nucleation. A similar consideration is important in the crystallization of STO within high-aspect-ratio structures e.g. narrow and deep trenches or pores. Very large distances of the progression of crystalline interfaces are obtained at low temperatures e.g. 500 nm at 450 °C. Equation 2-4 further suggests

that L_C can be increased by optimizing the difference between the activation energies for nucleation and interface motion, for example by varying the annealing environment.

2.6 Conclusions

A comparison study of the crystallization kinetics of amorphous STO on single-crystal (001) STO and amorphous SiO_2/Si substrates shows that at relatively low temperatures, the amorphous/crystalline interface can propagate over long distances by SPE without polycrystalline nucleation away from the interfaces. The results indicate that it will be possible to synthesize single-crystalline oxides in nanoscale complex geometries via crystallization from the amorphous layer. In addition to STO, crystallization by SPE has already been demonstrated in other complex oxides, for example in the perovskites $EuTiO_3$,[28] $CaTiO_3$,[3] $BiFeO_3$ on STO,[29-30] and $SmNiO_3$ on $LaAlO_3$.[31] The discovery of the crystallization kinetics of STO thus points to methods for which a wide range of other functional oxides, e.g. ferroelectrics and multiferroics, can also be grown in complex geometries by exploiting the difference between the kinetics of nucleation at non-epitaxial interfaces and the kinetics of SPE growth at epitaxial interfaces. More generally, crystallization from an amorphous layer provides an alternative route to the synthesis of nanoscale complex-oxide materials that have been discovered and studied at the scale of individual structures.[32-33] In addition, there are indications in the literature that complex oxide electronic interfaces can be created by recrystallization.[34] 3D structures are very useful for the design of microelectronic and optoelectronic devices, and energy storage systems.[35-37] Further exploration of nucleation and growth effects in these systems will facilitate the integration of complex oxides in 3D electronic, optoelectronic, and ionic devices.

2.7 References

1. Taira, K.; Hirose, Y.; Nakao, S.; Yamada, N.; Kogure, T.; Shibata, T.; Sasaki, T.; Hasegawa, T. Lateral Solid-Phase Epitaxy of Oxide Thin Films on Glass Substrate Seeded with Oxide Nanosheets. *Acs Nano* **2014,** *8* (6), 6145-6150.
2. Ishiwara, H.; Yamamoto, H.; Furukawa, S.; Tamura, M.; Tokuyama, T. Lateral Solid-Phase Epitaxy of Amorphous Si Films on Si Substrates with SiO_2 Patterns. *Appl. Phys. Lett.* **1983,** *43* (11), 1028-1030.
3. White, C. W.; Boatner, L. A.; Sklad, P. S.; Mchargue, C. J.; Rankin, J.; Farlow, G. C.; Aziz, M. J. Ion-Implantation and Annealing of Crystalline Oxides and Ceramic Materials. *Nucl. Instrum. Methods Phys. Res., Sect. B* **1988,** *32*, 11-22.
4. Simpson, T. W.; Mitchell, I. V.; Mccallum, J. C.; Boatner, L. A. Hydrogen Catalyzed Crystallization of Strontium Titanate. *J. Appl. Phys.* **1994,** *76* (5), 2711-2718.
5. Wang, F.; Badaye, M.; Yoshida, Y.; Morishita, T. Characterization of the Recovery and Recrystallization of $SrTiO_3$ Surface by Ion Channeling. *Nucl. Instrum. Methods Phys. Res., Sect. B* **1996,** *118* (1-4), 547-551.
6. Almeida, B. G.; Pietka, A.; Caldelas, P.; Mendes, J. A.; Ribeiro, J. L. Determination of Infrared Optical Parameters of $SrTiO_3$ Thin Films from the Reflectivity Spectrum. *Thin Solid Films* **2006,** *513* (1-2), 275-282.
7. Mccallum, J. C.; Rankin, J.; White, C. W.; Boatner, L. A. Time Resolved Reflectivity Measurements in Pb-Implanted $SrTiO_3$. *Nucl. Instrum. Methods Phys. Res., Sect. B* **1990,** *46* (1-4), 98-101.
8. Rankin, J.; McCallum, J. C.; Boatner, L. A. The Effect of Annealing Environments on the Epitaxial Recrystallization of Ion-Beam-Amorphized $SrTiO_3$. *J. Mater. Res.* **1992,** *7* (3), 717-724.
9. White, C.; McHargue, C. J.; Sklad, P.; Boatner, L.; Farlow, G. Ion implantation and annealing of crystalline oxides. *Mater. Sci. Rep.* **1989,** *4* (2), 41-146.
10. Gutierrez, G.; Johansson, B. Molecular Dynamics Study of Structural Properties of Amorphous Al_2O_3. *Phys. Rev. B* **2002,** *65* (10), 104202.
11. Hoang, V. V. Molecular Dynamics Study on Structure and Properties of Liquid and Amorphous Al_2O_3. *Phys. Rev. B* **2004,** *70* (13).
12. Levin, I.; Brandon, D. Metastable Alumina Polymorphs: Crystal Structures and Transition Sequences. *J. Am. Ceram. Soc.* **1998,** *81* (8), 1995-2012.
13. Shi, J.; Li, Z. D.; Kvit, A.; Krylyuk, S.; Davydov, A. V.; Wang, X. D. Electron Microscopy Observation of TiO_2 Nanocrystal Evolution in High-Temperature Atomic Layer Deposition. *Nano Letters* **2013,** *13* (11), 5727-5734.
14. Christian, J. W. *The Theory of Transformations in Metals and Alloys,* Elsevier Science Ltd. : Oxford, 2002.
15. Kempen, A. T. W.; Sommer, F.; Mittemeijer, E. J. Determination and Interpretation of Isothermal and Non-isothermal Transformation Kinetics; the Effective Activation Energies in Terms of Nucleation and Growth. *J. Mater. Sci.* **2002,** *37* (7), 1321-1332.
16. Jiang, S. F.; ter Horst, J. H. Crystal Nucleation Rates from Probability Distributions of Induction Times. *Cryst. Growth Des.* **2011,** *11* (1), 256-261.
17. Connell, J. G.; Isaac, B. J.; Ekanayake, G. B.; Strachan, D. R.; Seo, S. S. A. Preparation of Atomically Flat $SrTiO_3$ Surfaces Using a Deionized-water Leaching and Thermal Annealing Procedure. *Appl. Phys. Lett.* **2012,** *101* (25), 251607.

18. Boschker, J. E.; Tybell, T. Qualitative Determination of Surface Roughness by *in situ* Reflection High Energy Electron Diffraction. *Appl. Phys. Lett.* **2012,** *100* (15), 151604.
19. Yadav, S.; Ghosh, S. Amorphous Strontium Titanate Film as Gate Dielectric for Higher Performance and Low Voltage Operation of Transparent and Flexible Organic Field Effect Transistor. *ACS Appl. Mater. Interfaces* **2016,** *8* (16), 10436-10442.
20. Bjorck, M.; Andersson, G. GenX: an Extensible X-ray Reflectivity Refinement Program utilizing Differential Evolution. *J. Appl. Crystallogr.* **2007,** *40*, 1174-1178.
21. ICDD PDF Powder Diffraction File. *International Centre for Diffraction Data, Newtown Square, Pennsylvania, USA.*
22. Liu, J.; Shen, Z. J.; Nygren, M.; Su, B.; Button, T. W. Spark Plasma Sintering Behavior of Nano-sized (Ba, Sr)TiO_3 Powders: Determination of Sintering Parameters Yielding Nanostructured Ceramics. *J. Am. Ceram. Soc.* **2006,** *89* (9), 2689-2694.
23. Cuffini, S. L.; Macagno, V. A.; Carbonio, R. E.; Melo, A.; Trollund, E.; Gautier, J. L. Crystallographic, Magnetic, and Electrical-Properties of $SrTi_{1-x}Ru_xO_3$ Perovskite Solid-Solutions. *J. Solid State Chem.* **1993,** *105* (1), 161-170.
24. Paine, D. C.; Whitson, T.; Janiac, D.; Beresford, R.; Ow-Yang, C. W.; Lewis, B. A Study of Low Temperature Crystallization of Amorphous Thin Film Indium-Tin-Oxide. *J. Appl. Phys.* **1999,** *85* (12), 8445-8450.
25. Kim, M. G.; Kim, H. S.; Ha, Y. G.; He, J. Q.; Kanatzidis, M. G.; Facchetti, A.; Marks, T. J. High-Performance Solution-Processed Amorphous Zinc-Indium-Tin Oxide Thin-Film Transistors. *J. Am. Chem. Soc.* **2010,** *132* (30), 10352-10364.
26. Terban, M. W.; Cheung, E. Y.; Krolikowski, P.; Billinge, S. J. L. Recrystallization, Phase Composition, and Local Structure of Amorphous Lactose from the Total Scattering Pair Distribution Function. *Crystal Growth & Design* **2016,** *16* (1), 210-220.
27. Billinge, S. J. L.; Kanatzidis, M. G. Beyond crystallography: the study of disorder, nanocrystallinity and crystallographically challenged materials with pair distribution functions. *Chemical Communications* **2004,** (7), 749-760.
28. Shimamoto, K.; Hirose, Y.; Nakao, S.; Fukumura, T.; Hasegawa, T. Solid Phase Epitaxy of $EuTiO_3$ Thin films on $SrTiO_3$ (100) Substrates with Different Oxygen Contents. *J. Cryst. Growth* **2013,** *378*, 243-245.
29. Akbashev, A. R.; Plokhikh, A. V.; Barbash, D.; Lofland, S. E.; Spanier, J. E. Crystallization Engineering as a Route to Epitaxial Strain Control. *APL Mater.* **2015,** *3* (10), 106102.
30. Akbashev, A. R.; Chen, G. N.; Spanier, J. E. A Facile Route for Producing Single-Crystalline Epitaxial Perovskite Oxide Thin Films. *Nano Lett.* **2014,** *14* (1), 44-49.
31. Shi, J.; Zhou, Y.; Ramanathan, S. Colossal Resistance Switching and Band Gap Modulation in a Perovskite Nickelate by Electron Doping. *Nat. Commun.* **2014,** *5*, 4860.
32. Setter, N.; Damjanovic, D.; Eng, L.; Fox, G.; Gevorgian, S.; Hong, S.; Kingon, A.; Kohlstedt, H.; Park, N. Y.; Stephenson, G. B.*; et al.* Ferroelectric Thin films: Review of Materials, Properties, and Applications. *J. Appl. Phys.* **2006,** *100* (5), 051606.
33. Ramesh, R.; Spaldin, N. A. Multiferroics: Progress and Prospects in Thin Films. *Nat. Mater.* **2007,** *6* (1), 21-29.
34. Aurino, P. P.; Kalabukhov, A.; Tuzla, N.; Olsson, E.; Klein, A.; Erhart, P.; Boikov, Y. A.; Serenkov, I. T.; Sakharov, V. I.; Claeson, T.*; et al.* Reversible Metal-Insulator Transition of Ar-Irradiated $LaAlO_3/SrTiO_3$ Interfaces. *Phys. Rev. B* **2015,** *92* (15), 155130.

35. Xu, S.; Yan, Z.; Jang, K. I.; Huang, W.; Fu, H. R.; Kim, J.; Wei, Z.; Flavin, M.; McCracken, J.; Wang, R.*; et al.* Assembly of Micro/Nanomaterials into Complex, Three-Dimensional Architectures by Compressive Buckling. *Science* **2015,** *347* (6218), 154-159.
36. Kong, Y. L.; Tamargo, I. A.; Kim, H.; Johnson, B. N.; Gupta, M. K.; Koh, T. W.; Chin, H. A.; Steingart, D. A.; Rand, B. P.; McAlpine, M. C. 3D Printed Quantum Dot Light-Emitting Diodes. *Nano Lett.* **2014,** *14* (12), 7017-7023.
37. Tian, X. C.; Jin, J.; Yuan, S. Q.; Chua, C. K.; Tor, S. B.; Zhou, K. Emerging 3D-Printed Electrochemical Energy Storage Devices: A Critical Review. *Adv. Energy Mater.* **2017,** *7* (17).

Chapter 3: Seeded lateral solid-phase crystallization of the perovskite oxide $SrTiO_3$

3.1 Introduction

As described in detail in Chapter 1, because epitaxial complex-oxide thin film growth by vapor-phase epitaxy involves long surface diffusion lengths and often requires the line-of-sight transport of material from the sources to the growth surface, it has been challenging to extend the potential of highly functional, large-area epitaxial crystalline complex oxides into the realm of nanomaterials. A promising approach for the synthesis of epitaxial complex-oxide nanostructures is the crystallization of amorphous precursors via post-deposition heating.[1] The kinetics of solid-phase crystallization are favorable for the formation of complex oxides in intricate nanoscale geometries. The diffusion in the solid state is slow at the temperatures that are required for the crystallization of amorphous oxides, and the seeded growth is fast in comparison with nucleation on non-epitaxial interfaces, as discussed in Chapter 2 for $SrTiO_3$ (STO).[1-2]

Lateral crystallization from nano-engineered nucleation sites has recently emerged as a way to achieve nanoscale oxide materials. Previous reports indicate that isolated crystalline seeds can serve as nuclei for the crystallization of metal oxides from their amorphous form.[3-4] Seeded solid-phase crystallization can be used to create crystals with controlled crystallinity, including the crystallographic orientation and grain size, on a variety of substrates at significantly lower temperatures than are employed in epitaxial

growth.[3-4] The substrates can be amorphous or polycrystalline substrates including glass or plastic that are of industrial importance.

A particular example of the importance of seeding is in selecting the crystallographic phase of oxide compounds that exhibit multiple structural phases. Micron-scale crystals of α-Al_2O_3 can be formed by crystallizing amorphous Al_2O_3 with α-Al_2O_3 seed crystals, without the formation of the γ-Al_2O_3 phase commonly observed in unseeded crystallization.[3,5]

Another particular example shows the importance of seeding in creating oxide crystals on amorphous substrates with the selected crystallographic orientation and with micron-scale lateral size. The crystallization of amorphous Nb-doped TiO_2 can be directed by nanosheet-seeded lateral SPE, resulting in (001)-oriented Nb-doped TiO_2 crystals with lateral sizes up to 10 μm on glass substrates.[4] Preliminary results indicate that this approach may also apply to STO. Lattice-matched $Ca_2Nb_3O_{10}$ nanosheets with a 1-nm-thick STO secondary seed layer were used to seed the lateral SPE growth of an amorphous STO film deposited by PLD, but the kinetics and structural details of this process have not yet been reported.[4]

Fully exploiting the control of lateral crystallization from nanoscale nucleation sites requires the development of methods for laterally resolved local characterization of structural properties. Important unresolved questions in complex-oxide seeded solid-phase crystallization are associated with the rate of crystallization, the evolution of the amorphous and crystalline structures, and the precise role of the intentionally introduced seeds in determining the overall orientation of the resulting crystals.

This chapter reports the discovery of strategies for seeding crystallization with nanoscale nucleation sites and the discovery of kinetic phenomena important to crystallization. The nucleation strategies reported here employ two types of seeds: (i) single-crystal $SrRuO_3$ (SRO) nanomembranes (NMs) with (001) orientation and a thickness of 50 nm and (ii) nanocrystalline seeds of STO with random orientation and with a few nanometers in thickness. The nanoscale seeds were placed on SiO_2/Si substrates before the deposition of an amorphous STO layer. The lateral solid-phase crystallization rates of amorphous STO from SRO NMs and STO nanocrystalline seeds are close to the SPE growth rate on a planar STO substrate and are unexpectedly isotropic. The kinetics of crystallization at the temperature investigated here favor crystal growth initiated at seeds rather than nucleation away from seeds and, as a result, regions with several microns in extent can be crystallized near seeds before nucleation at separate locations.

The use of nanoscale seeds supported on SiO_2/Si substrates to initiate the crystallization of STO is illustrated in step (i) of Figures 3-1(a) and (b). The SRO NM and STO nanocrystalline seeds were subsequently covered with a uniform amorphous STO layer deposited by sputter deposition over the entire surface, as depicted in step (ii) of Figure 3-1. The amorphous STO layers were deposited by sputtering with the same conditions described in Section 2.3 of Chapter 2. Heating the seed crystal/amorphous layer structure induces solid-phase crystallization (step (iii) of Figure 3-1). At the relatively low temperature employed in this study, amorphous STO crystallizes into polycrystalline STO laterally from the seed crystals over several microns before impinging on crystals that formed via unseeded nucleation.

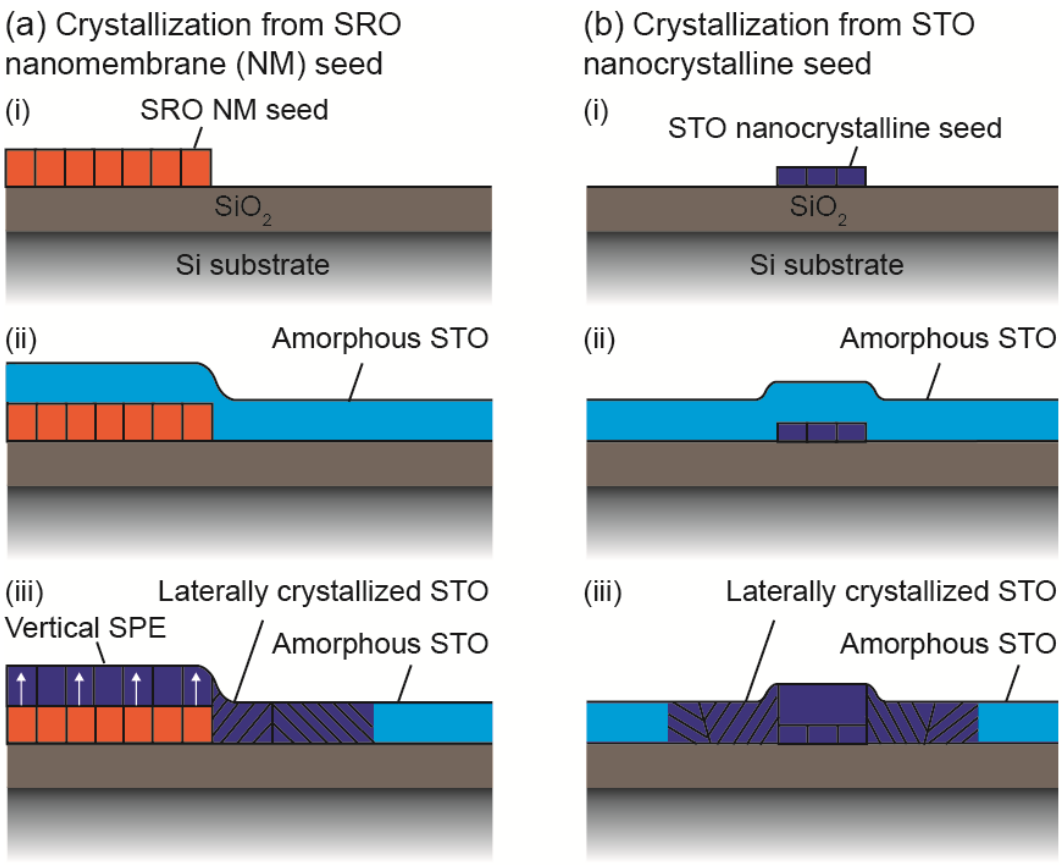

Figure 3-1. Seeded solid-phase crystallization of amorphous STO using (a) a single-crystal SRO NM seed and (b) an STO nanocrystalline seed: (i) placement or fabrication of seeds on a SiO_2/Si substrate, (ii) deposition of an amorphous STO layer, and (iii) vertical crystallization of amorphous STO on top of the SRO NM and lateral crystallization of amorphous STO from the edges of the seeds.

3.2 Synthesis and characterization of seed crystals

3.2.1 Synthesis and characterization of SRO seed crystals

The SRO NM seed crystals were formed by transferring 50-nm-thick single-crystalline SRO thin films grown on (001) STO to SiO_2/Si substrates. The SRO NMs were created through a collaboration with Dr. Dillon Fong and Dr. Deborah Paskiewicz at Argonne National Laboratory (ANL). The epitaxial growth, release, and transfer were done by Dr. Paskiewicz during her work as a postdoctoral researcher at ANL. The fabrication

process involves several steps. First, epitaxial SRO thin films with dimensions of 2 × 2 mm^2 were grown on (001) STO substrates. Then the sample surface was patterned with a photoresist exhibiting a periodic array of 50 x 50 μm^2 holes and immersed in a room-temperature $HF/HNO_3/H_2O$ etching solution allowed to reach the substrate. The duration of the immersion depended on the size and spacing of the etchant access holes. The SRO NMs became freestanding after the near surface region of the STO substrate was dissolved.[6] A SiO_2/Si substrate was subsequently submerged in the solution to slowly withdraw the SRO NMs. SRO has excellent chemical and thermal stability and a lattice parameter close to STO, making it a favorable choice for use as a seed crystal that can be moved to other substrates using liquid or dry transfer.[7]

The SRO NMs had lateral extents ranging from several microns to one millimeter. A scanning electron microscopy (SEM) image of a corner of an SRO NM on a SiO_2/Si substrate and a schematic of the SRO seed layer are shown in Figures 3-2(a) and (b). SEM characterization was performed using a Zeiss LEO 1530 Schottky-type field-emission scanning electron microscope, with an accelerating voltage of 3 kV. Other SEM measurements described in Figures 3-3, 3-6, 3-8 and 3-9 in the following text were also conducted with this accelerating voltage.

The SEM image shows that the SRO NM is uniform and has abrupt edges. The SRO NM sheets were characterized using synchrotron X-ray nanobeam diffraction. The details of the measurements were described in Section 1.5 of Chapter 1. The intensity distributions given in the text of this Chapter are reported in terms of the wavevector Q, defined as $Q = 4\pi/\lambda \sin\theta$. Figure 3-2(c) shows a plot of the intensity as a function of the out-of-plane wavevector Q_z, equivalent to a thin-film θ-2θ scan, for the SRO 002 X-ray

reflection. The out-of-plane lattice parameter and thickness derived from Figure 3-2(c) are 3.94 Å and 52 nm. The FWHM of the rocking curve of the SRO 002 reflection is 0.19°, shown in Figure 3-2(d). The small mosaic width of the SRO 002 reflection indicates that the SRO NM remains a single crystal after it is transferred.

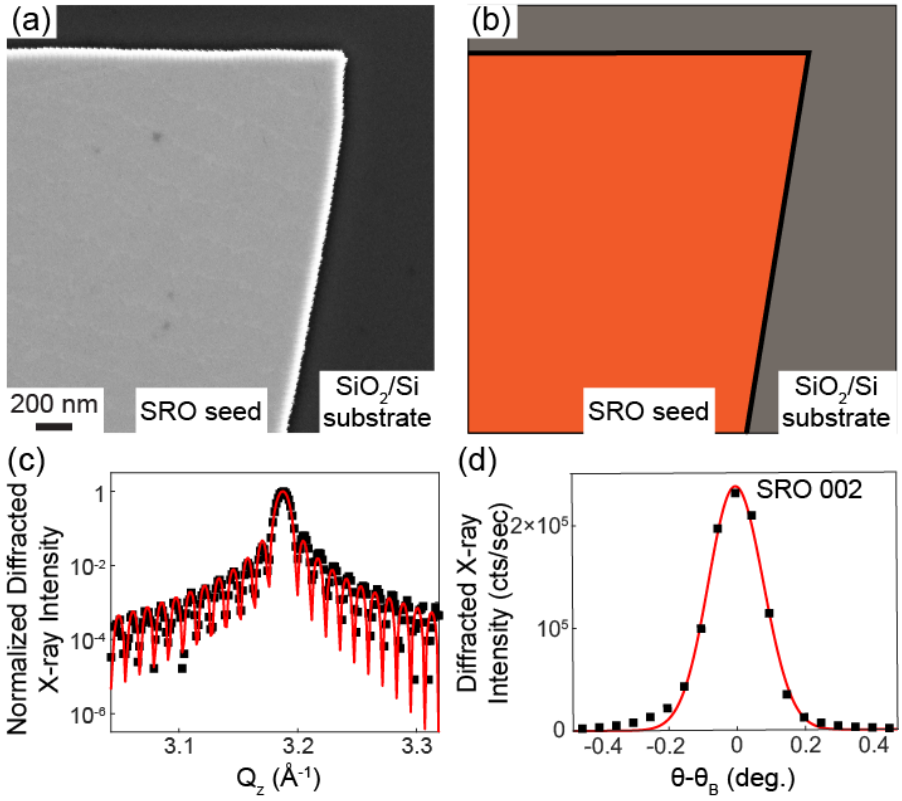

Figure 3-2. (a) SEM image of a corner of the SRO NM seed on a SiO_2/Si substrate. (b) Geometry of the SRO NM seed on a SiO_2/Si substrate. (c) X-ray diffraction pattern of the SRO NM seed. (d) X-ray rocking curve of the SRO NM seed. Here θ_B= 20.43° is the Bragg angle of the SRO 002 pseudocubic reflection at the 9 keV x-ray photon energy of these measurements.

3.2.2 Synthesis and characterization of STO seed crystals

The complementary strategy employing STO seed crystals is based on the synthesis of widely dispersed STO nanocrystals. The STO seed crystals were created by depositing a thin amorphous STO layer through a shadow mask, followed by dewetting and

crystallization of the layer by thermal annealing. The steps involved in this process are illustrated in Figure 3-3(a). A very thin STO layer forms adjacent to the thicker layer deposited through the openings of the shadow mask (Fotofab, LLC), as shown in panels (i) and (ii) of Figure 3-3(a). The amorphous layer was crystallized by heating to 650 °C for 180 min, as shown in panel (iii) of Figure 3-3(a).

X-ray diffraction measurements using the Bruker D8 Advance diffractometer were conducted at each step in the formation of the nanocrystalline STO seeds. Figure 3-3(b) shows grazing-incidence X-ray scattering patterns acquired from the bare SiO_2/Si substrate, the as-deposited amorphous STO film, and the fully crystallized STO film. The bare SiO_2/Si substrate exhibits a featureless low-intensity background. The X-ray scattering pattern of the amorphous STO includes a broad intensity maximum centered at wavevector Q = 2.1 $Å^{-1}$. After heating to 650 °C for 180 min, the broad peak disappears and a series of polycrystalline STO X-ray reflections with far higher intensity appear. The sharp reflections indicate that the amorphous STO had crystallized into polycrystalline STO seeds.

The spatial distribution of the STO seeds is shown in the SEM image in Figure 3-3(c). A key feature in this distribution is a gradient in the seed concentration resulting from the initial non-uniformity of the STO coverage near the edge of the shadow mask. The seeds have sizes ranging from tens to hundreds of nanometers, as shown in the images of several individual nanocrystalline STO seeds in Figure 3-3(d). Many isolated STO seeds that have only three or four lateral facets are probably composed of just one or a few STO crystals. Larger seeds without obvious facets may be aggregates of several crystals with different orientations.

Figure 3-3(e) shows an atomic force microscopy (AFM) topography image of an area containing several isolated STO nanocrystalline seeds. The surface morphology of the STO seed crystals was imaged using a non-contact mode with a Bruker Multimode 8 AFM. The STO seed crystals have a complex height profile in which their edges are higher than their centers, as shown in Figure 3-3(f) for three different crystallites. In each case, the edges of the seeds are 1-7 nm higher than their centers, consistent with the curvature of the seeds, as discussed below. The inside of the seed crystals is very thin, with apparent heights from 0.1 nm to 5 nm, as shown in the height profiles of several nanocrystalline seeds in Figure 3-3(f).

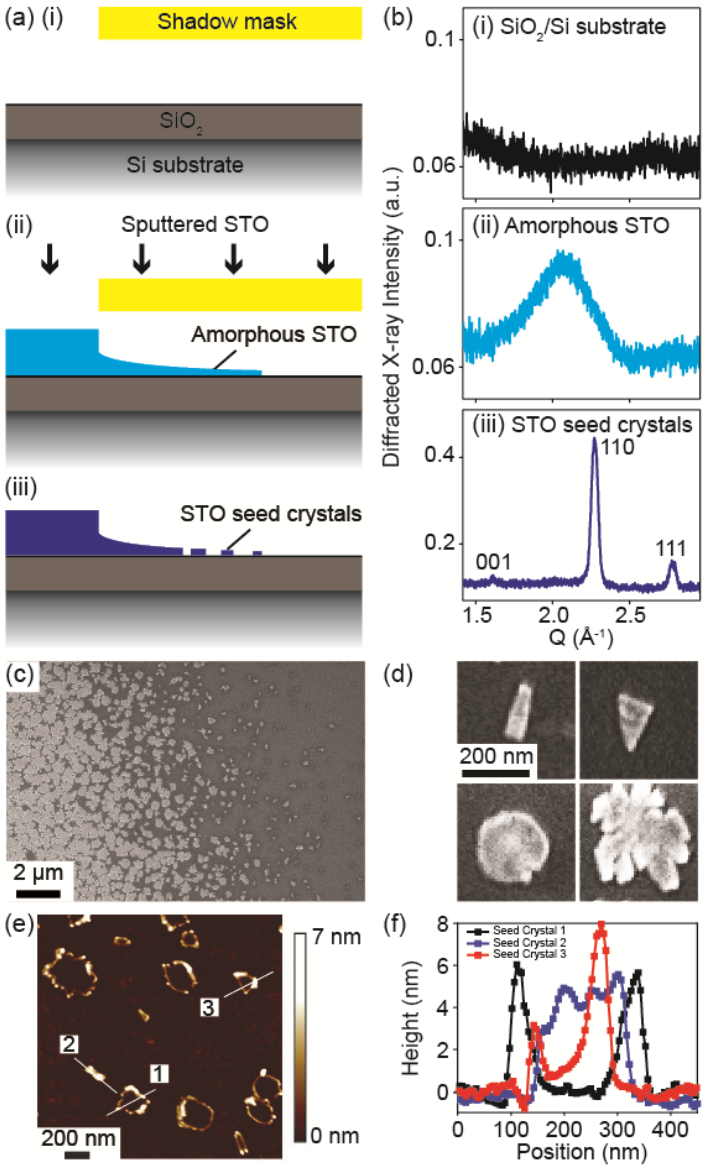

Figure 3-3. (a) Synthesis of STO seed crystals: (i) SiO_2/Si substrate. (ii) Deposition of an amorphous STO layer onto the substrate through a shadow mask, creating a low-coverage of amorphous STO close to the shadow mask edge. (iii) Ripening and crystallization of STO seeds. (b) Grazing-incidence X-ray scattering corresponding to steps (i) to (iii) in the synthesis of STO seed crystals. (c) and (d) SEM images of the distribution and shapes of STO seed crystals. (e) AFM image of STO seed crystals. (f) Height profiles of the crystals indicated in (e).

The crystallinity and orientation of the STO nanocrystalline seeds were probed using synchrotron X-ray nanobeam diffraction with a spot size of 30 nm. The details of the measurements were described in Section 1.4 of Chapter 1. The nanocrystalline seeds were

investigated within a sample consisting of both seeds and an STO layer, after heating to 450 °C for 2160 min. The nanodiffraction experiment thus probed the seeds and the volume of material crystallized above each seed. Figures 3-4(a) and (b) show maps of the diffracted intensity as a function of the location of the X-ray beam, where STO crystallites are oriented with the [110] and [001] directions aligned along the surface normal, respectively. The crystallites in Figures 3-4(a) and (b) have lateral sizes of hundreds of nanometers, consistent with the SEM and AFM images in Figure 3-3. The spatial extents of the crystals appearing in the nanobeam diffraction maps span a subset of their overall physical volume in which the Bragg condition is satisfied and the detector accepts the diffracted beam. For the [110] STO crystallite map in Figure 3-4(a), the total detector acceptance was increased by placing the detector at different angular positions to acquire the map. The image of the [110] oriented crystal thus reflects the full extent of the crystal. The [001]-oriented crystal in Figure 3-4(b) was studied with a smaller X-ray detector acceptance and the extent of this crystal is slightly underestimated.

Both the AFM and X-ray nanobeam measurements indicate that the STO crystallites have a significant curvature. The X-ray nanobeam diffraction study shows that the orientation of the seeds in Figures 3-4(a) and (b) vary by 7° over a distance of 200 nm, which is consistent with the tilt of $\tan^{-1}(5\text{ nm}/50\text{ nm}) \approx 6°$ observed in the AFM height profiles in Figure 3-3(f). The radius of curvature of the seeds is thus approximately 1 μm. A schematic model of the microstructure of the STO nanocrystalline seeds based on these measurements is shown in Figure 3-4(c). The seeds exhibit both a range of crystallographic orientations and a morphology in which the crystal is higher at the edges.

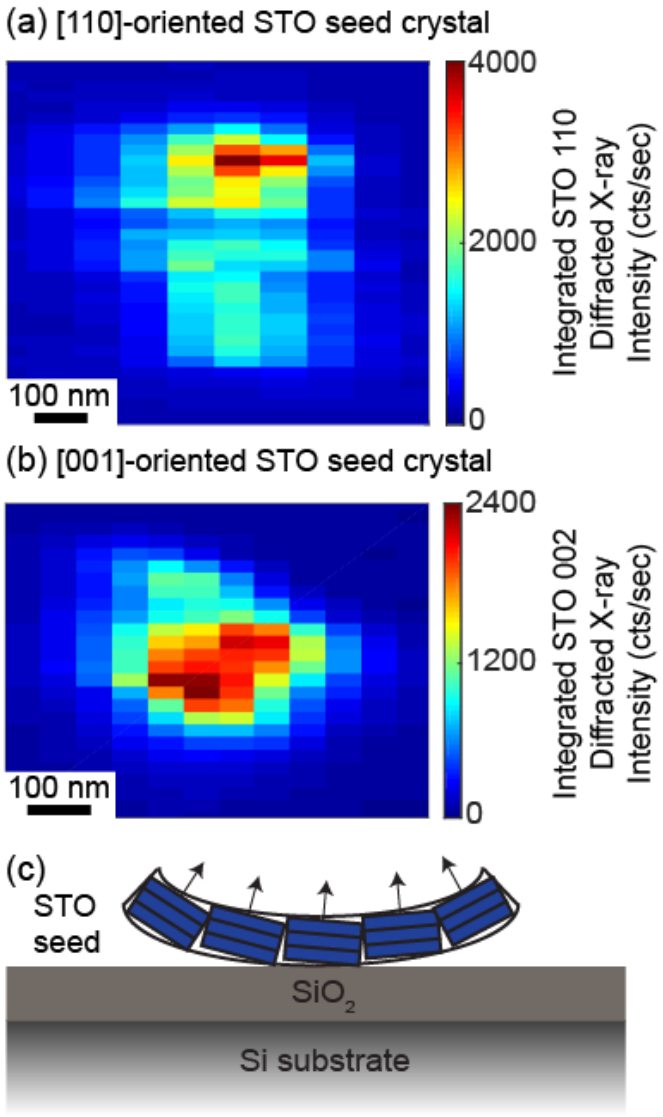

Figure 3-4. X-ray nanodiffraction maps of isolated STO seed crystals and the crystallized STO film on top of the seeds with (a) [110] and (b) [001] orientations along the surface normal using the 110 and 002 X-ray reflections, respectively. (c) Diagram of STO nanocrystal seed curvature. The lines and arrows for each crystallite indicate the orientation and normal directions of crystallographic planes.

Previous studies found that STO crystallites formed by crystallizing an amorphous STO layer are curved and attributed the curvature to the stress at the amorphous/crystalline interface.[8] The STO seed crystals in Figure 3-3 are not surrounded by an amorphous film, which indicates that the curvature of the seeds results from a different effect. The elastic or plastic curvature of STO seed crystals may arise instead from a small stress imbalance

through the thickness of the STO crystals. A second possible reason of curvature is through delamination during cooling from 650 °C to room temperature due to the different thermal expansion coefficients of STO and SiO_2/Si.

3.3 Lateral solid-phase crystallization from seed crystals

Lateral solid-phase crystallization was studied by probing nucleation and crystal growth of a uniform amorphous STO layer deposited across the entire surface, including the regions atop and adjacent to the seed crystals, as depicted in step (ii) of Figure 3-1(b). The thickness, roughness, and uniformity of the STO layer in a region of the sample near the edge of the SRO NM seeds was investigated using synchrotron X-ray reflectivity. The reflectivity experiment was conducted at station ID-01 of the European Synchrotron Radiation Facility using a photon energy of 8.00 keV (λ=1.5498 Å) and an X-ray beam focused to a spot size of approximately 300 nm using a Kirkpatrick-Baez X-ray focusing mirror. The reflectivity data were collected in a region at a distance of 10 μm away from the edge of the SRO NM. The sample was oriented so that the long footprint of the beam was parallel to the edge of the SRO NM.

The X-ray reflectivity of the amorphous layer is shown in Figure 3-5. The analysis of the measured reflected intensity distribution employed the same method used for the analysis of the XRR data of an amorphous STO layer on the SiO_2/Si substrate described in Section 2.4.2 of Chapter 2 using the GenX software package.[9] The results of the fit give a STO layer thickness of 38 nm, a root-mean-square roughness of 0.5 nm and a density of 4.3 g cm^{-3}. The density of the STO layer is consistent with the reported values of 4.2 ± 0.1 g cm^{-3} of amorphous STO.[10] The X-ray reflectivity study indicates that the amorphous STO

layers on seed crystals are uniform and not perturbed by the presence of the seed crystals during deposition.

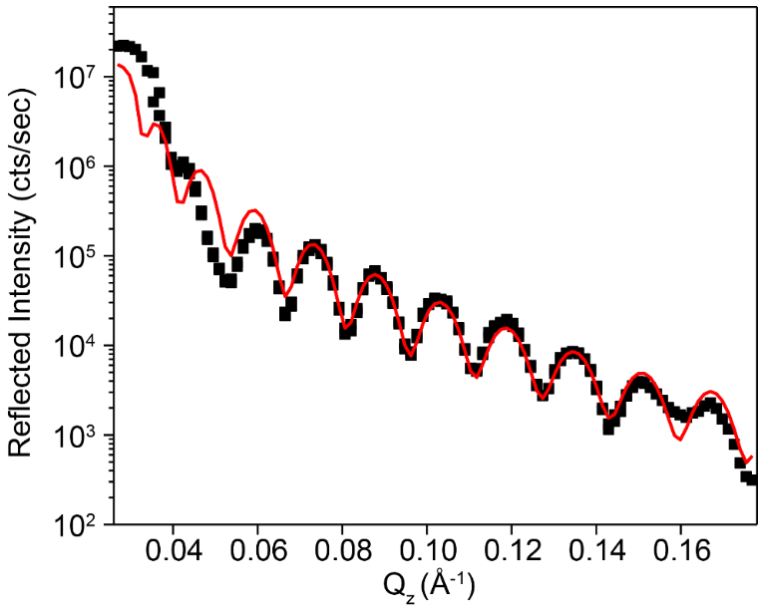

Figure 3-5: Reflected X-ray intensity (square points) and X-ray reflectivity model consisting of an amorphous STO thin film on a SiO_2/Si substrate.

3.3.1 Lateral crystallization from SRO seed crystals

The crystallization of amorphous STO from SRO NM seeds was investigated in a series of experiments in which the samples were heated to 450 °C. Crystallization proceeds both laterally from the edges of the SRO NMs and vertically from their faces. Lateral crystal growth results in regions of crystallized STO around the edges of the NMs, as shown in Figure 3-6. Figures 3-6(a)-(c) show SEM images of the edge of an SRO NM with an as-deposited amorphous STO layer before crystallization and after crystallization by heating to 450 °C for 360 min and 2160 min. The crystallization results in the formation of the comparatively bright regions at the edges of the SRO NM seeds. The lateral growth distances measured at different locations along the edge are 630 ± 40 nm at 360 min and

2000 ± 40 nm at 2160 min. A linear fit to the crystallization distance, shown in Figure 3-6(d), gives a lateral growth rate of 0.9 ± 0.1 nm/min. The lateral growth rate during crystallization from the edge of the SRO NM seed is slightly larger than the vertical growth rate in thin-film SPE on a single-crystal (001) STO substrate at this temperature, which was 0.6 nm/min.[2]

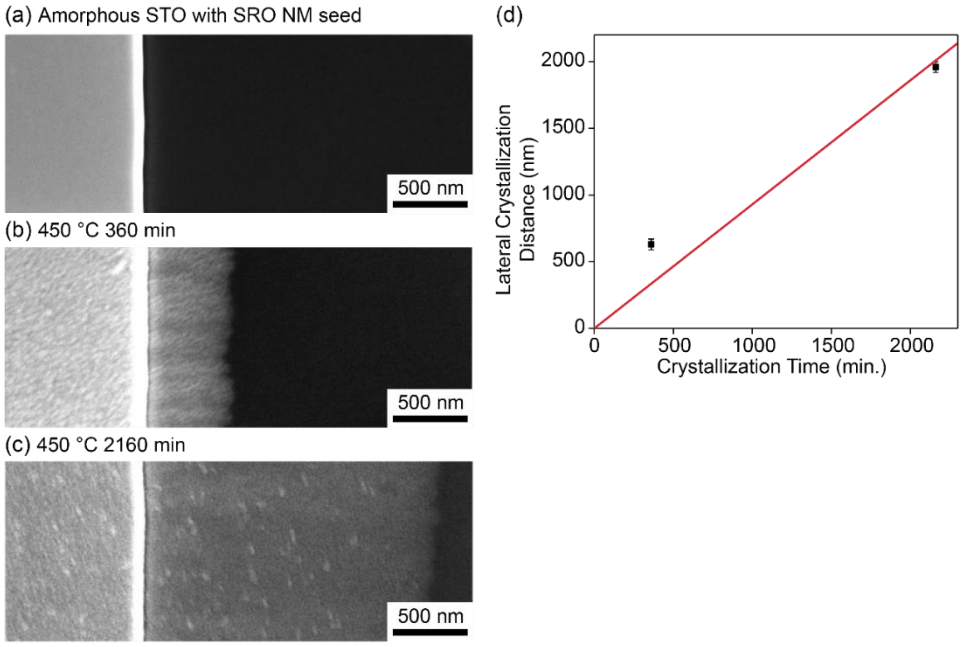

Figure 3-6. SEM images of an SRO NM seed (a) with an amorphous STO layer before crystallization, and after crystallization at 450 ºC for (b) 360 min and (c) 2160 min. (d) Lateral crystallization distance from the edge of the SRO NM seed as a function of crystallization time at 450 ºC. The linear fit gives a lateral crystal growth rate of 0.9 nm/min.

The crystallinity and crystallographic orientation of the laterally crystallized STO layer near the SRO NM seed was characterized using electron backscatter diffraction (EBSD). The EBSD measurements were conducted by Dr. Jack Tilka during his work as a PhD student at University of Wisconsin-Madison. The orientation of STO crystallized near SRO NMs was probed by EBSD using imaging and analysis software (EDAX, Inc.). The EBSD data was acquired with the sample titled 70° with respect to the primary beam.

Figure 3-7(a) shows a secondary electron SEM image of an area close to an edge of the SRO NM seed in which the sample had been heated to 450 °C for 2160 min. Figures 3-7(b)-(d) show EBSD inverse pole figure maps in which each pixel is colored according to the crystallographic direction within the STO or SRO crystal that points along different Cartesian directions. Here, z is parallel to the surface normal, y points away from the edge of the NM, and x is along the edge. The randomly colored region outside the crystallized region in Figures 3-7(b)-(d) is a result of arbitrary fitting of the background and noise to the EBSD pattern of the amorphous STO layer.

The EBSD inverse pole figure maps of the crystallized regions near the SRO NM show that the laterally crystallized STO has an overall polycrystalline microstructure. Micron-scale STO grains extend from the edge of the SRO NM seed to the amorphous/crystalline STO boundary. A large number of grains within the crystallized STO layer in Figure 3-7(c) are oriented with a <001> direction along the length of the SRO NM edge, the same in-plane orientation of the SRO NM seed. The existence of regions of STO exhibiting the same in-plane orientation as the SRO NM indicates that there is some texture of the laterally crystallized STO within the larger-scale polycrystallinity.

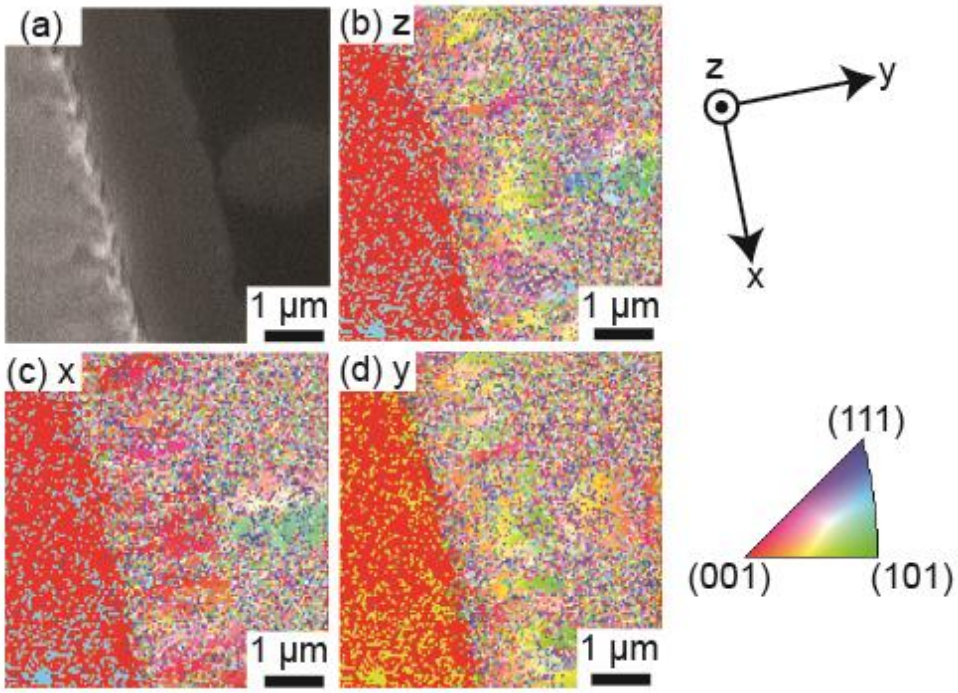

Figure 3-7. (a) Secondary electron SEM image after crystallization from an SRO NM seed at 450 ºC for 2160 min. (b), (c), and (d) EBSD inverse pole figure maps of the area shown in (a) in which each pixel is colored with according to which crystallographic direction of the combined SRO and STO crystal is along the z, x and y unit vectors defined in the inset.

The shape of the crystallized region near the SRO seed provides insight into the possible dependence of the lateral crystallization rate on the STO crystallographic orientation. Figure 3-7 shows that many regions of the crystallized STO near the SRO seed exhibit in-plane growth directions that are not oriented along <001>. The width varies by less than 10% at different locations along the edge and does not show any systematic relationship between the growth rate and orientation. The images in Figure 3-7 thus indicate that the growth rates vary by less than 0.1 nm/min as a function of crystallographic orientation under these crystallization conditions.

In addition to the crystallization nucleated at the boundary of the SRO NM, the SEM and EBSD measurements reveal a low concentration of STO crystals that were

nucleated in locations away from the edge of the SRO NM seed. A separately crystallized region is visible at a distance of 3 μm from the edge of the SRO NM in the SEM image and EBSD inverse pole figure maps in Figures 3-7(b)-(d). The EBSD inverse pole figure maps of the crystal nucleated far from the SRO NM does not exhibit the preferred <001> in-plane texture observed in crystals nucleated from the SRO NM. The separately nucleated and crystallized area instead appears to be formed from several crystals with non-<001> directions in the plane of the sample surface.

3.3.2 Lateral crystallization from STO seed crystals

The lateral crystallization from STO seed crystals was studied by heating the amorphous STO/STO seed structure to 450 °C. After heating, circular regions of crystallized STO form surrounding each seed crystal, as shown in the SEM images acquired after heating to 450 °C for 270 min, 450 min, and 840 min in Figures 3-8(a)-(c). The average crystallized radius at different crystallization times was determined by measuring the mean radius of 10-30 isolated crystallized regions at each temperature and is plotted in Figure 3-8(d). The vertical growth of STO on top of the STO seeds through the 40-nm thickness of the amorphous STO takes place over a much shorter time than the micron-scale lateral crystallization. The time associated with the complicated initial three-dimensional crystallization is thus safely neglected in this analysis.

A linear fit to the time-dependence of the crystallization distances observed over the entire range of crystallization times gives a lateral growth rate of 0.5 ± 0.1 nm/min at 450 °C, shown as the solid line in Figure 3-8(d). Including only the crystallization time points up to 720 min, however, gives a growth rate of 0.6 ± 0.2 nm/min, shown as the dashed line in Figure 3-8(d). This growth rate is very close to the vertical growth rate of

amorphous STO on top of single-crystal (001) STO.[2] As discussed below, the slight underestimation of the crystallization rate by including the long crystallization times in the growth rate measurement may be caused by the crystals formed by unseeded nucleation and growth on substrates at relatively long crystallization times.

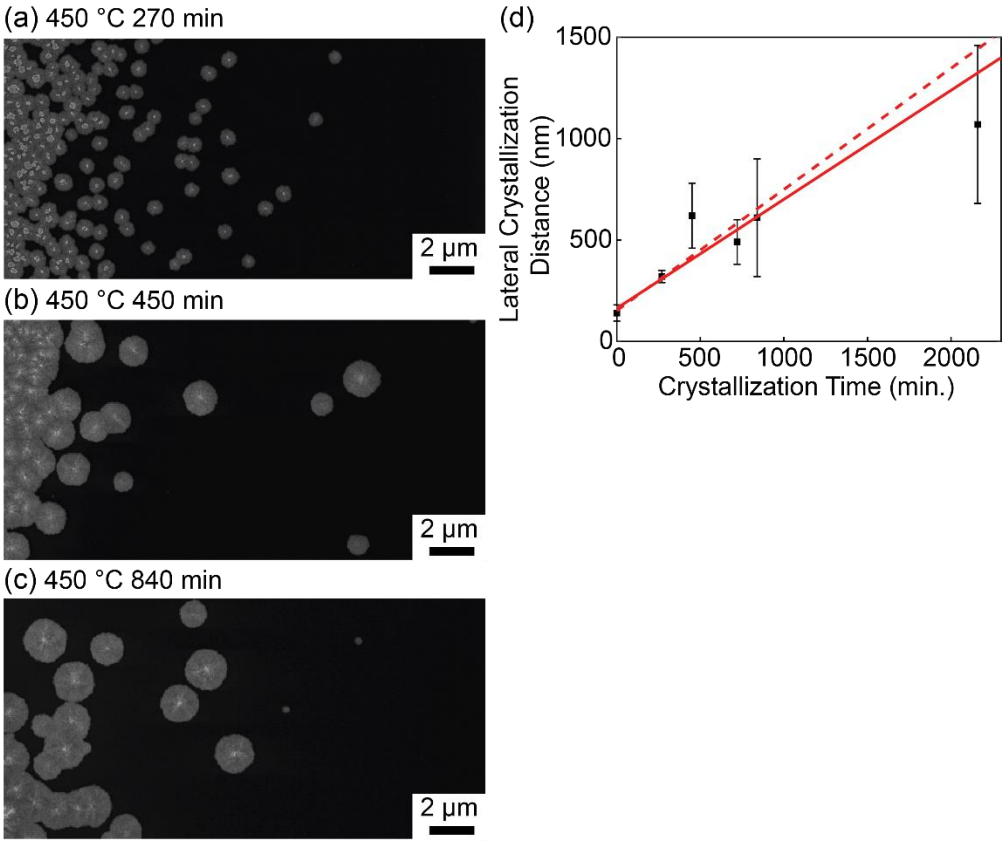

Figure 3-8. SEM images of an initially amorphous STO film deposited on isolated STO seed crystals following crystallization at 450 °C for (a) 270 min, (b) 450 min, and (c) 840 min. (d) Crystallized radius as a function of crystallization time. The solid and dashed lines are linear fits over the full range of times and times up to 720 min, respectively.

The crystals formed by heating to 450 °C for 270 min are approximately circular, as shown in Figures 3-9(a) and (b) and have a mean radius of 300 nm. The statistical distribution of radii has a standard deviation of 30 nm. Crystallization into circular islands indicates that, under these conditions, the growth rate does not depend on the

crystallographic orientation of the amorphous/crystalline interface. The effectively isotropic growth rate from nanocrystalline STO seeds matches what was observed during crystallization from the SRO NM seeds.

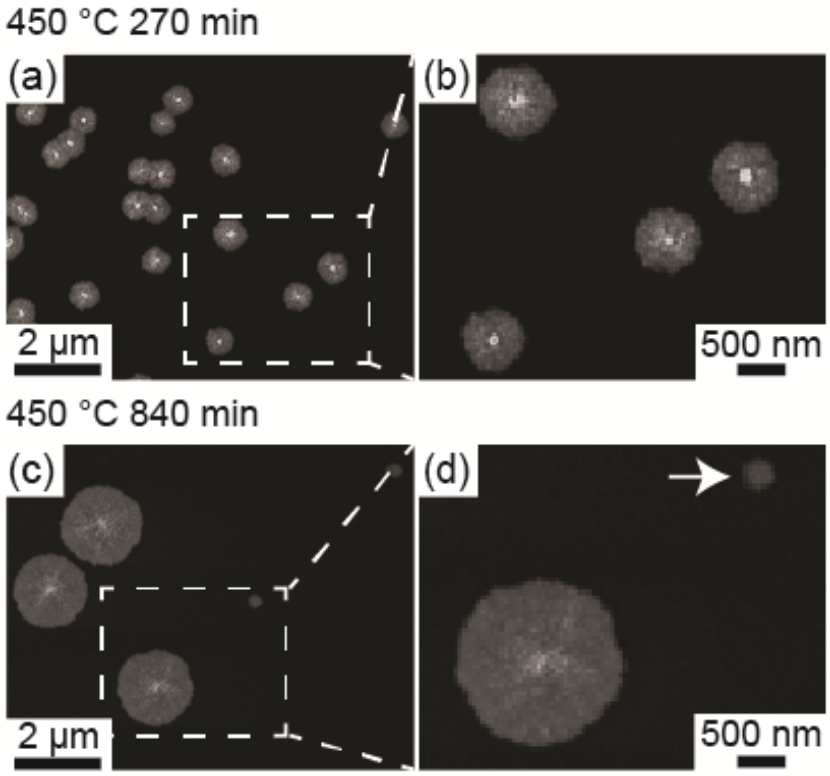

Figure 3-9. SEM images after crystallization at 450 ºC for the indicated times, (a) and (b) 270 min, (c) and (d) 840 min. The arrow in (d) indicates an STO crystal nucleated at a location away from an STO seed crystal.

Nucleation and growth of STO crystals at locations away from the STO nanocrystalline seeds was observed at long crystallization times. Figure 3-9(c) shows an SEM image of the STO film with the nanocrystalline seeds heated to 450 ºC for 840 min. The contrast in the micrographs allows the crystallized STO to be distinguished from the STO nanocrystalline seed. The crystallized STO regions nucleated at seed crystals have a mean radius of 800 nm. Other crystallized regions have smaller radii ranging from 200 to 400 nm. The difference between this range of sizes is far larger than the standard deviation

of 30 nm observed with shorter heating times. The absence of visible STO seed crystals at the centers of the regions with smaller radii indicates that they were formed by nucleation at sites away from the seeds following a long incubation time. A similar long incubation time was previously observed in unseeded crystallization of amorphous STO on SiO_2/Si.[2] Including the crystalline areas nucleated in regions away from the nanocrystalline seeds causes a slight underestimation in the determination of the lateral crystallization velocity. The growth rate from the SRO NM seeds was not systematically underestimated because the nucleation and growth of STO crystals away from the edge of SRO NM did not affect the measurement of the crystallization distance in that system.

The microstructure of STO crystallized at 450 °C for 2160 min using the nanocrystalline STO seeds was evaluated using an unfocused synchrotron X-ray beam with a spot size of 100 × 100 μm^2. Figure 3-10 shows a radial scan in reciprocal space, acquired as a θ-2θ scan, in which the X-ray beam probed a region near the edge of a shadow mask. The peak positions and relative integrated peak intensities agree with the powder X-ray diffraction pattern of STO, consistent with the formation of polycrystalline STO in random orientations.[11]

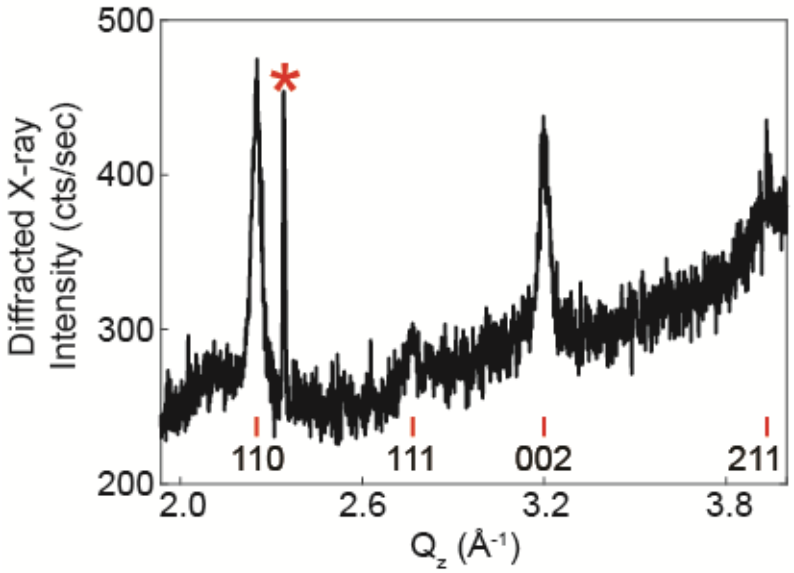

*Figure 3-10. X-ray diffraction pattern of STO crystallized at 450 °C for 2160 min with STO seed crystals. Reflections arising from STO are labeled with their indices. An additional reflection at Q_z = 2.34 Å^{-1} (marked with *) arises from the diffraction of incident X-rays with one half of the nominal incident wavelength by the Si substrate 004 reflection.*

3.4 SPE growth on top of SRO NM

3.4.1 SPE growth measured with laboratory-source X-ray diffraction

The structure of the STO crystallized on top of the SRO NM was first examined by laboratory-source X-ray diffraction. The data were collected using the method described in Section 1.6 of Chapter 1. The laboratory-source diffraction study employed a millimeter-scale X-ray beam and thus provides a diffraction pattern averaged over the full area of the sample. The laterally crystallized regions near the edges of the NMs occupy a small fraction of the total sample area covered by the SRO NMs and thus contribute negligibly to the area-averaged diffracted intensity. Figure 3-11(a) shows the intensity as a function of Q_z for STO crystallized on SRO NM seeds by heating at 450 °C for 2160 min, measured with laboratory X-ray diffraction. Both the SRO 002 and STO 002 reflections are evident,

showing that the amorphous STO film on top of the SRO NM transforms into an epitaxial layer.

The angular widths of the X-ray rocking curves provide insight into the relative defect densities within the STO layer and the SRO seed. Figure 3-11(b) shows rocking curve scans of SRO 002 and STO 002 reflections near θ_B, which give FWHM values of 0.29° and 0.40°, respectively. The crystallized STO on top of the SRO membrane thus has a larger concentration of extended defects than in the SRO membrane leading to a broader mosaic width than the SRO membrane.

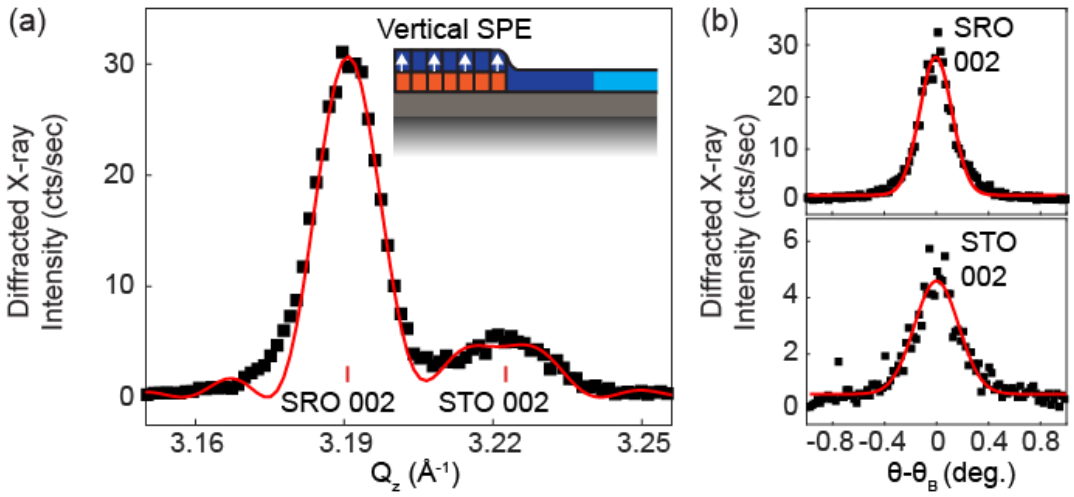

Figure 3-11. (a) Laboratory X-ray diffraction pattern (points) and kinematic X-ray diffraction simulation (line) of STO crystallized on SRO NM seeds at 450 °C for 2160 min. (b) Rocking curve scans of SRO 002 and STO 002 reflections with Gaussian fits used to find the angular widths of each reflection.

The STO lattice parameter is a key quantity that provides insight into the degree to which the epitaxial mismatch between STO and SRO has been relaxed by the formation of defects. Three methods with increasing mathematical and experimental complexity were employed to measure this lattice parameter as accurately as possible.

The first, and likely least accurate, approach to measuring the lattice parameters of STO and SRO uses the overall magnitude of the 2θ angles of the STO and SRO 002 reflections. By fitting the data in Figure 3-11(a) with the kinematic X-ray diffraction simulation, the out-of-plane lattice parameters of the crystallized STO layer and the SRO NM are derived to be 3.902 Å and 3.94 Å, respectively, and the thicknesses of the crystallized STO layer and the SRO NM are derived to be 28 nm and 38 nm, respectively. Both the measurements described in Section 3.2 of this Chapter and the study reported by Dr. Deborah Paskiewicz show that the SRO NM also had a lattice parameter of 3.94 Å before the deposition of STO and the crystallization process.[12] The same lattice parameter indicates that the SRO NM remains relaxed on SiO_2/Si substrates after deposition of an amorphous STO layer and the subsequent heating procedure.

The second measurement of the STO lattice parameter uses the angular difference between the STO and SRO 002 reflections to measure the out-of-plane lattice parameter of STO more precisely. STO has a cubic structure and SRO has a pseudocubic structure. c_{STO} and c_{SRO} are the out-of-plane lattice parameters of STO and SRO, respectively. c_{SRO} was determined to be 3.94 Å based on the 2θ value of its 002 reflection. c_{STO} was then calculated based on c_{SRO} and the angular difference in 2θ between the STO and SRO 002 reflections, denoted as $\Delta\theta$. In the equations listed below, θ_R is the Bragg angle of the SRO 002 reflection.

$$2dsin\theta = \lambda$$

The derivative of the above equation can be written as:

$$-\frac{\Delta d}{d} = \frac{cos\theta_R}{sin\theta_R}\Delta\theta$$

The relationship between the d spacing of 002 planes and the out-of-plane lattice parameter of a cubic structure is: $d = \frac{c}{2}$. Plug into the above equation:

$$-\frac{c_{STO} - c_{SRO}}{c_{SRO}} = cot\theta_R \Delta\theta c_{STO} = c_{SRO}(1 - cot\theta_R \Delta\theta)$$

Equation 3-1

The Bragg angle θ_R of the SRO 002 reflection is 23.018º based on the value of c_{SRO} which has been determined to be 3.94 Å. The measured $\Delta\theta$ between 002 reflections of SRO and STO is 0.235º. c_{STO} is thus determined to be 3.902 Å based on Equation 3-1, consistent with the results obtained with the first method.

The in-plane and out-of-plane lattice parameters of STO are denoted as a_{STO} and c_{STO}, respectively. The bulk STO has a lattice parameter of a_0 =3.905 Å. With c_{STO} = 3.902 Å, the crystallized STO layer has a compressive out-of-plane strain ε_{out} = -0.1% with respect to a_0. With the in-plane strain ε_{in} and the Poisson ratio v of STO, the expected ε_{out} arising from the mechanical constraint imparted by the SRO NM on the STO is:[13]

$$\varepsilon_{out} = -\frac{2v}{1-v}\varepsilon_{in}$$

$$\varepsilon_{in} = -\frac{1-v}{2v}\varepsilon_{out}$$

With $\varepsilon_{in} = \frac{a_{STO} - a_0}{a_0}$ and $\varepsilon_{out} = \frac{c_{STO} - a_0}{a_0}$, the following equation can be obtained:

$$\frac{a_{STO} - a_0}{a_0} = -\frac{1-v}{2v}\frac{c_{STO} - a_0}{a_0}$$

$$a_{STO} = a_0 - \frac{1-v}{2v}(c_{STO} - a_0)$$

Equation 3-2

The Poisson ratio of STO is $v = 0.232$.[14] The a_{STO} deduced from the Equation 3-2 is 3.910 Å, which is very close to a_0. A fully coherent epitaxial layer of STO on the SRO NM would have in-plane strain ε_{in} = 0.9% and out-of-plane strain ε_{out} = -0.5%. The calculated a_{STO} of 3.910 Å and ε_{out} of -0.1% indicate that the crystallized STO film on SRO NM is nearly completely relaxed under these deposition and crystallization conditions.

The third, and final, approach used to measure the lattice parameter of the epitaxial STO layer employed the small angular differences between the 103 reflections of STO and SRO. This separate X-ray study used the Bruker D8 Advance diffractometer to probe the in-plane and out-of-plane lattice parameters of STO by measuring the interplanar angles between 103 and 001 planes of STO and SRO.

Figure 3-12 shows the 2D detector image of the measurement of 103 reflections of STO and SRO. In the 2D detector image, Υ represents the azimuthal angle normal to the 2θ direction. $\Delta\Upsilon$ and $\Delta 2\theta$ are the angular differences between the 103 reflections of STO and SRO in the γ and 2θ directions, respectively. φ_R and φ_T is the interplanar angle between 103 and 001 planes for SRO and STO, respectively. The in-plane and out-of-plane lattice parameters of STO a_{STO} and c_{STO} can be deduced from the angular difference $\Delta\Upsilon$ and $\Delta 2\theta$ based on the Equations 3-3, 3-4, 3-5, 3-6 listed below. The calculated result was consistent with the conclusion that the epitaxial STO layer is nearly completely relaxed.

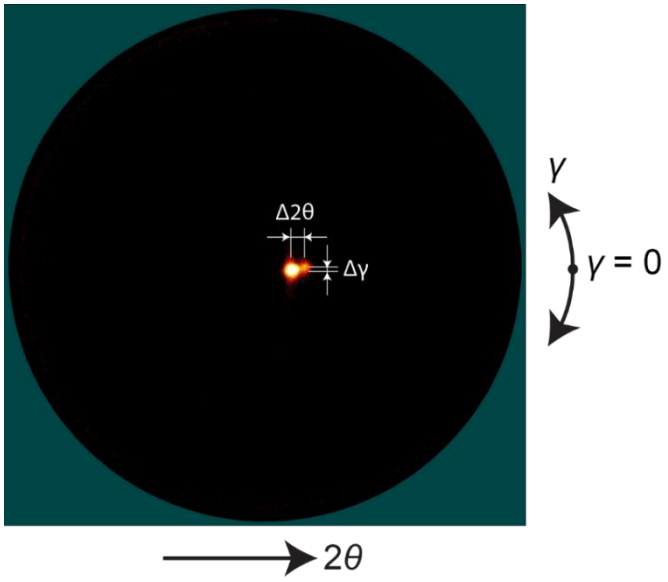

Figure 3-12. 2D detector image of the measurement of 103 reflections of SRO and STO. The reflection with smaller 2θ is from SRO (left) and the reflection with larger 2θ is from STO (right).

The 103 lattice planes of STO and SRO are tilted with respect to each other by $\Delta\varphi$:[15]

$$\Delta\varphi = \Delta\gamma \frac{k}{q}$$

For 103 reflections, wavevectors $q = \frac{2\pi}{d_{103}}$, $k = \frac{2\pi}{\lambda}$, and $sin\theta_{B\ 103} = \frac{\lambda}{2d_{103}}$.

$\Delta\varphi$ is thus related to the measured $\Delta\gamma$ and the Bragg angle of the SRO 002 reflection θ_B with the following equation:

$$\Delta\varphi = \Delta\gamma \frac{2\pi}{\lambda} \frac{d_{103}}{2\pi} = \Delta\gamma \frac{d_{103}}{\lambda} = \Delta\gamma \frac{1}{2sin\theta_{B\ 103}}$$

Equation 3-3

For cubic SRO, the interplanar angle between 103 and 001 is φ_R.

$$cos\varphi_R = \frac{3}{\sqrt{10}} \quad \varphi_R = 18.43°$$

For tetragonal STO, the interplanar angle between 103 and 001 is φ_T.

$$cos\varphi_T = \frac{3}{\sqrt{9 + \frac{{c_{STO}}^2}{{a_{STO}}^2}}}$$

It is useful to define the small difference between c_{STO} and a_{STO} using a parameter that has a value much less than 1 in order to allow the denominator to be expanded in a Taylor series. The small parameter δ is termed the tetragonality correction and is defined so that $\frac{{c_{STO}}^2}{{a_{STO}}^2} = 1 + 10\delta$. With this substitution the expansion is straightforward:

$$cos\varphi_T = \frac{3}{\sqrt{9 + 1 + 10\delta}} = \frac{3}{\sqrt{10}}\frac{1}{\sqrt{1 + \delta}} = \frac{3}{\sqrt{10}}\left(1 - \frac{1}{2}\delta\right) = cos\varphi_R\left(1 - \frac{1}{2}\delta\right)$$

$$cos\varphi_T - cos\varphi_R = -\frac{1}{2}\delta cos\varphi_R$$

Because $\Delta(cos\varphi) = -sin\varphi\Delta\varphi$, so $cos\varphi_T - cos\varphi_R = -sin\varphi_R\Delta\varphi$

Plug in, the following equation can be obtained:

$$-sin\varphi_R\Delta\varphi = -\frac{1}{2}\delta cos\varphi_R$$

$$\delta = 2tan\varphi_R\Delta\varphi$$

$$\frac{{c_{STO}}^2}{{a_{STO}}^2} = 1 + 10\delta = 1 + 20tan\varphi_R\Delta\varphi$$

Equation 3-4

Use $\Delta 2\theta$ to find c_{STO} and use $\frac{c_{STO}}{a_{STO}}$ to find a_{STO} based on Equation 3-4.

The d spacing of 103 lattice planes of SRO and STO is d_{103}^{R} and d_{103}^{T} respectively.

$$d_{103}^{R} = \frac{c_{SRO}}{\sqrt{10}}$$

$$d_{103}^{T} = \left(\frac{1}{\frac{1}{a_{STO}^2} + \frac{9}{c_{STO}^2}}\right)^{\frac{1}{2}} = c_{STO}\left(\frac{1}{\frac{c_{STO}^2}{a_{STO}^2} + 9}\right)^{\frac{1}{2}} = c_{STO}\left(\frac{1}{1 + 10\delta + 9}\right)^{1/2}$$

$$= \frac{c_{STO}}{\sqrt{10}}\left(\frac{1}{1+\delta}\right)^{1/2} = \frac{c_{STO}}{\sqrt{10}}\left(1 - \frac{1}{2}\delta\right)$$

$$d_{103}^{T} - d_{103}^{R} = \frac{c_{STO}}{\sqrt{10}}\left(1 - \frac{1}{2}\delta\right) - \frac{c_{SRO}}{\sqrt{10}}$$

$$\Delta d_{103} = \Delta c\left(\frac{1 - \frac{1}{2}\delta}{\sqrt{10}}\right)$$

$$\Delta c = \frac{\sqrt{10}\Delta d_{103}}{1 - \frac{1}{2}\delta} = \sqrt{10}\Delta d_{103}\left(1 + \frac{1}{2}\delta\right)$$

Suppose the STO film is fully relaxed and has a cubic structure, the tetragonality correction of δ is thus 0. The following equation can be obtained:

$$c_{STO} = c_{SRO} + \sqrt{10}\Delta d_{103}$$

$$\frac{\Delta d_{103}}{d_{103}} = -cot\theta_{103}\Delta\theta_{103}$$

$$\Delta d_{103} = -d_{103}(cot\theta_{103}\Delta\theta_{103}) = -\frac{c_{SRO}}{\sqrt{10}}cot\theta_{103}\Delta\theta_{103}$$

$$c_{STO} = c_{SRO} + \sqrt{10}\left(-\frac{c_{SRO}}{\sqrt{10}}cot\theta_{103}\Delta\theta_{103}\right) = c_{SRO}(1 - cot\theta_{103}\Delta\theta_{103})$$

Equation 3-5

Suppose the STO film is strained on SRO, the tetragonality correction of δ is thus not 0. The following equation can be obtained:

$$c_{STO} = c_{SRO} + \sqrt{10}\Delta d_{103}\left(1+\frac{1}{2}\delta\right) = c_{SRO} - \sqrt{10}\frac{c_{SRO}}{\sqrt{10}}cot\theta_{103}\Delta\theta_{103}\left(1+\frac{1}{2}\delta\right)$$

$$c_{STO} = c_{SRO}\left(1 - cot\theta_{103}\Delta\theta_{103}\left(1+\tfrac{1}{2}\delta\right)\right)$$

Equation 3-6

δ is small, so this is a second-order correction.

The three methods show essentially the same result. The crystallized STO layer is epitaxially grown on the SRO NM and the epitaxial mismatch between STO and SRO has been nearly completely relaxed by the formation of defects.

3.4.2 SPE growth measured with synchrotron-source X-ray diffraction

The structure of the STO crystallized on top of the SRO NM was also examined with synchrotron-source X-ray diffraction. Because the spot size of the focused X-ray nanobeam is 50 nm, the local epitaxial relationship between SRO and STO can be examined with X-ray nanodiffraction. The details of synchrotron X-ray nanobeam diffraction measurements were introduced in Section 1.4 of Chapter 1.

The relatively large convergence angle of the nanofocused beam allowed a single incident angle to be used to probe both the STO 002 and SRO 002 reflections simultaneously. Figure 3-13(a) plots the intensity of each reflection as a function of position along a line crossing the edge of the SRO NM. The simultaneous rapid decrease of the diffracted intensity from STO and SRO at the edge of the SRO NM indicates that the STO grows epitaxially on the SRO NM. The abrupt decrease in the STO 002 intensity

away from the edge of the SRO NM also shows that the laterally crystallized STO does not have an [001] out-of-plane orientation. A diffraction pattern acquired with the X-ray nanobeam illuminating only the SRO seed and the top epitaxial STO layer is shown in Figure 3-13(b). The narrow angular range of STO 002 reflection along the vertical direction of the 2D detector further indicates that the STO film is epitaxially grown on the SRO NM.

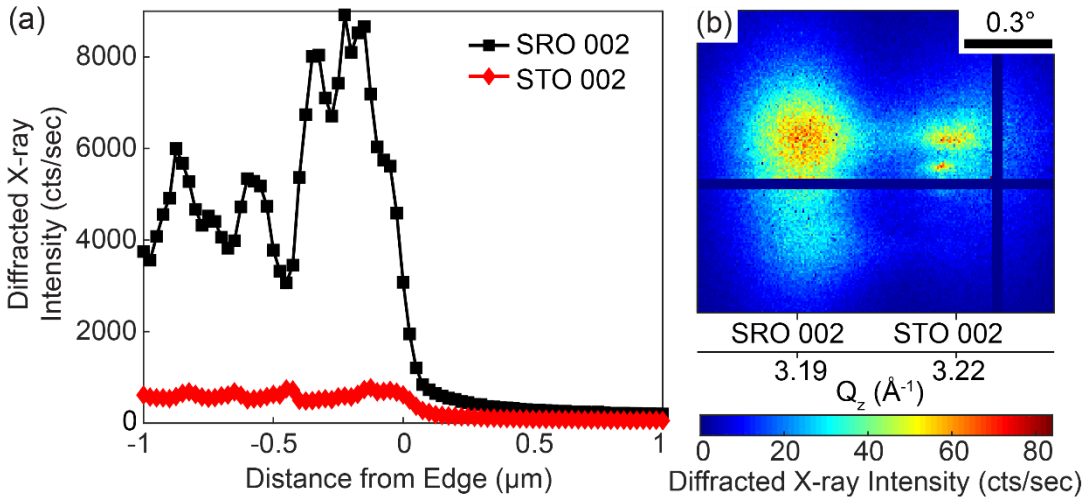

Figure 3-13. (a) Intensities of SRO 002 and STO 002 reflections as a function of position along a line crossing the edge of the SRO NM, measured with synchrotron X-ray nanodiffraction. (b) Individual X-ray diffraction pattern with STO 002 and SRO 002 reflections acquired with the X-ray nanobeam illuminating the SRO seed and epitaxial STO layer. The horizontal angular axis of the diffraction plane is in the scattering plane and is labeled with corresponding values of the wavevector Q_z. The vertical axis is angle out of the scattering angle. Dark lines arise from the insensitive area between quadrants of the X-ray detector.

3.5 Discussion

The lateral crystallization results provide insight into the relative rates of the two key nucleation and growth processes: (i) crystallization via the motion of amorphous/crystalline interfaces from the seed crystals and (ii) the nucleation of new crystals away from the seeds. The results of previous homoepitaxial SPE studies of STO

at 450 °C have suggested that the amorphous/crystalline crystallization front can propagate over a distance of at least 0.5 μm before impinging on nuclei away from the initial amorphous/crystalline interface.[2] The use of vertical thin-film geometries to study the relative rates of nucleation and growth processes, however, was limited because the maximum seeded growth distance without nucleation was limited by the film thickness. Lateral crystallization distances from nanoscale seed crystals are orders of magnitude greater than the film thickness and can allow these phenomena to be investigated. The present results indicate that the seeded crystallization fronts propagate at least 2 μm before impinging on separately nucleated crystals. This distance is far larger than the previously estimated value of 0.5 μm using STO/STO thin-film homoepitaxy experiments.[2] Crystallization over micron-scale distances occurs without nucleation within the amorphous STO, at the surface, or at the STO/SiO_2 interfaces. Based on these results, it appears to be possible to crystallize STO and other similar perovskite structures in complex nanoscale architectures starting from individual seeds.

The lateral crystallization rate is apparently independent of the crystallographic orientation of the crystallized STO. The constant crystallization rate observed in the present experiments with STO has also been observed in other oxide systems with similar crystal structures. An isotropic lateral growth rate was observed, for example, in the crystallization of amorphous perovskite oxide Pb(Zr,Ti)O_3 (PZT) thin films from pre-formed PZT seed islands.[16] SPE studies of $CaTiO_3$ (CTO) show that the growth rate in <001> directions is only a factor of three larger than in <010> directions.[17] The SPE velocities for STO [001] and [110] are approximately equal.[18] Together, the results from PZT, CTO, and STO suggest that comparatively isotropic lateral crystallization rates from seed crystals may be

a general phenomenon in perovskite oxides. The apparently isotropic lateral growth rate of STO and other perovskite-oxide crystals indicate that the rate-limiting steps in the crystallization process occur within the amorphous STO rather than at the amorphous/crystalline interface, which may include rearrangement of the anion bonding configuration or other changes of the amorphous structures.[19-20]

The crystallization from the SRO NM shows that the seed crystals determine at least some aspects of the crystal orientation during lateral crystallization. There are isolated areas in Figure 3-7, for example, in which there is a clear influence of the SRO NM on the orientation of the crystallized STO. The remaining areas of lateral crystallization, however, do not have a well-defined relationship. The lack of an epitaxial relationship in these regions may be caused by the physical rough edge of the transferred SRO NM seed, which was not specifically prepared for epitaxial growth. Future preparation of SRO NM seeds with flat, straight, and crystallographically oriented edges may improve the lateral epitaxial growth of the STO film.

In systems other than perovskite STO, seeded crystallization of oxides with single crystals is an effective way to control the crystallographic orientations of the crystallized area. Large α-Al_2O_3 grains with the same orientations as the seeds were achieved by crystallizing an amorphous Al_2O_3 layer from α-Al_2O_3 seeds.[3] Epitaxial Nb:TiO_2 crystals with lateral sizes up to 10 μm were formed by crystallizing an amorphous Nb:TiO_2 layer from $Ca_2Nb_3O_{10}$ nanosheets with 1-nm-thick epitaxial Nb:TiO_2 secondary seed layers.[4] Nanoscale seed crystals may thus be utilized to control the orientations of the crystallized films in localized area or confined geometries. The methods presented in this work should thus be applicable to other materials including other perovskite oxides and metal oxides.

3.6 Conclusions

The lateral crystallization of STO can be initiated at selected locations using seed crystals. The lateral crystallization rates from both STO and SRO seeds are close to the SPE growth rate on a planar substrate. At a relatively low temperature of 450 ºC probed here, the kinetics of crystallization favor crystal growth around the seeds rather than nucleation away from the seeds. Following the nucleation at the seeds, amorphous/crystalline STO interfaces propagate over micron-scale distances without impinging on other separately nucleated crystals.

Crystallization from the amorphous form with seed crystals has the potential to create complex oxide nanostructures or in other complex geometries because the structure and morphology of the NM and nanocrystalline seeds are highly versatile. The two seeding strategies probed here provide essentially similar results, which indicates that our approaches can be generalized. Nanomembranes, such as the SRO NM seeds presented here can be transferred to specific locations in order to select the locations of crystallization. Similarly, isolated nanocrystalline islands can be produced in selected locations via the methods described here and used to seed the lateral crystallization. The results from the present STO/STO and STO/SRO seeding systems should be also applicable to the creation of other homoepitaxial and heteroepitaxial nanostructures due to high degree of similarity among the structural and chemical properties of perovskite oxides.

The creation of complex oxide nanostructures or in other complex geometries will enable new applications. For example, the interfaces between epitaxial lanthanum aluminates and TiO_2-termined STO exhibit electron-transport phenomena showing that

there is a two-dimensional electron gas at the interface.[21-22] These interfaces can presently be synthesized only in planar geometries, but they can have potentially widespread applications in 3D nanoscale geometries because of their promising electronic properties. Integrated circuits based on $LaAlO_3$-$SrTiO_3$ heterostructures have been demonstrated.[23] Our study provides the opportunities to integrate those epitaxial oxide interfaces in devices with 3D nanoscale geometries.

3.7 References

1. Evans, P. G.; Chen, Y.; Tilka, J. A.; Babcock, S. E.; Kuech, T. F. Crystallization of Amorphous Complex Oxides: New Geometries and New Compositions via Solid Phase Epitaxy. *Curr. Opin. Solid State Mater. Sci.* **2018,** *22*, 229-242.
2. Chen, Y. J.; Yusuf, M. H.; Guan, Y. X.; Jacobson, R. B.; Lagally, M. G.; Babcock, S. E.; Kuech, T. F.; Evans, P. G. Distinct Nucleation and Growth Kinetics of Amorphous $SrTiO_3$ on (001) $SrTiO_3$ and SiO_2/Si: A Step toward New Architectures. *ACS Appl. Mater. Interfaces* **2017,** *9*, 41034-41042.
3. Maret, H.; Weisberg, D.; Chan, H. M.; Strandwitz, N. C. Seeded Solid-Phase Epitaxy of Atomic Layer Deposited Aluminum Oxide. *Cryst. Growth Des.* **2016,** *16*, 1662-1666.
4. Taira, K.; Hirose, Y.; Nakao, S.; Yamada, N.; Kogure, T.; Shibata, T.; Sasaki, T.; Hasegawa, T. Lateral Solid-Phase Epitaxy of Oxide Thin Films on Glass Substrate Seeded with Oxide Nanosheets. *ACS Nano* **2014,** *8*, 6145-6150.
5. Simpson, T. W.; Wen, Q. Z.; Yu, N.; Clarke, D. R. Kinetics of the Amorphous → γ → α Transformations in Aluminum Oxide: Effect of Crystallographic Orientation. *J. Am. Ceram. Soc.* **1998,** *81*, 61-66.
6. Paskiewicz, D. M.; Sichel-Tissot, R.; Karapetrova, E.; Stan, L.; Fong, D. D. Single-Crystalline $SrRuO_3$ Nanomembranes: A Platform for Flexible Oxide Electronics. *Nano Lett.* **2016,** *16*, 534-542.
7. Koster, G.; Klein, L.; Siemons, W.; Rijnders, G.; Dodge, J. S.; Eom, C.-B.; Blank, D. H.; Beasley, M. R. Structure, Physical Properties, and Applications of $SrRuO_3$ Thin Films. *Rev. Mod. Phys.* **2012,** *84*, 253-298.
8. Longo, V.; Verheijen, M. A.; Roozeboom, F.; Kessels, W. M. M. Crystallization Study by Transmission Electron Microscopy of $SrTiO_3$ Thin Films Prepared by Plasma-Assisted ALD. *ECS Trans.* **2013,** *50*, 69-77.
9. Bjorck, M.; Andersson, G. GenX: an Extensible X-ray Reflectivity Refinement Program utilizing Differential Evolution. *J. Appl. Crystallogr.* **2007,** *40*, 1174-1178.
10. Simpson, T. W.; Mitchell, I. V.; Mccallum, J. C.; Boatner, L. A. Hydrogen Catalyzed Crystallization of Strontium Titanate. *J. Appl. Phys.* **1994,** *76* (5), 2711-2718.

11. Wang, F.; Badaye, M.; Yoshida, Y.; Morishita, T. Characterization of the Recovery and Recrystallization of $SrTiO_3$ Surface by Ion Channeling. *Nucl. Instrum. Methods Phys. Res., Sect. B* **1996,** *118*, 547-551.
12. Paskiewicz, D. M.; Sichel-Tissot, R.; Karapetrova, E.; Stan, L.; Fong, D. D. Single-Crystalline $SrRuO_3$ Nanomembranes: A Platform for Flexible Oxide Electronics. *Nano Letters* **2016,** *16* (1), 534-542.
13. Ederer, C.; Spaldin, N. A. Effect of Epitaxial Strain on the Spontaneous Polarization of Thin Film Ferroelectrics. *Phys. Rev. Lett.* **2005,** *95*, 257601.
14. Christen, H. M.; Specht, E. D.; Silliman, S. S.; Harshavardhan, K. S. Ferroelectric and Antiferroelectric Coupling in Superlattices of Paraelectric Perovskites at Room Temperature. *Phys. Rev. B* **2003,** *68* (2), 020101.
15. Evans, P. G.; Rugheimer, P. P.; Lagally, M. G.; Lee, C. H.; Lal, A.; Xiao, Y.; Lai, B.; Cai, Z. Microfabricated Strained Substrates for Ge Epitaxial Growth. *J. Appl. Phys.* **2005,** *97* (10).
16. Lee, J. S.; Joo, S. K. Self-Limiting Behavior of the Grain Growth in Lead Zirconate Titanate Thin Films. *J. Appl. Phys.* **2002,** *92*, 2658-2662.
17. Rankin, J.; McCallum, J. C.; Boatner, L. A. Annealing-Environment Effects in the Epitaxial Regrowth of Ion-Beam-Amorphized Layers on $CaTiO_3$. *J. Appl. Phys.* **1995,** *78*, 1519-1527.
18. White, C. W.; Boatner, L. A.; Sklad, P. S.; Mchargue, C. J.; Rankin, J.; Farlow, G. C.; Aziz, M. J. Ion-Implantation and Annealing of Crystalline Oxides and Ceramic Materials. *Nucl. Instrum. Methods Phys. Res., Sect. B* **1988,** *32*, 11-22.
19. Frenkel, A. I.; Ehre, D.; Lyahovitskaya, V.; Kanner, L.; Wachtel, E.; Lubomirsky, I. Origin of Polarity in Amorphous $SrTiO_3$. *Phys. Rev. Lett.* **2007,** *99*, 215502.
20. Blonkowski, S.; Defay, E.; Biquard, X. Sign of the Nonlinear Dielectric Susceptibility of Amorphous and Crystalline $SrTiO_3$ Films. *Phys. Rev. B* **2009,** *79*, 104108.
21. Ohtomo, A.; Hwang, H. Y. A High-Mobility Electron Gas at the $LaAlO_3/SrTiO_3$ Heterointerface. *Nature* **2004,** *427* (6973), 423-426.
22. Annadi, A.; Putra, A.; Liu, Z. Q.; Wang, X.; Gopinadhan, K.; Huang, Z.; Dhar, S.; Venkatesan, T.; Ariando Electronic Correlation and Strain Effects at the Interfaces between Polar and Nonpolar Complex Oxides. *Phys. Rev. B* **2012,** *86*, 085450.
23. Jany, R.; Richter, C.; Woltmann, C.; Pfanzelt, G.; Forg, B.; Rommel, M.; Reindl, T.; Waizmann, U.; Weis, J.; Mundy, J. A.*; et al.* Monolithically Integrated Circuits from Functional Oxides. *Adv Mater Interfaces* **2014,** *1*, 1300031.

Chapter 4: Solid-phase epitaxy of $PrAlO_3$ films grown by atomic layer deposition

4.1 Introduction

Ohtomo and Hwang reported in 2004 that a two-dimensional electron gas (2DEG) can be formed at the interface between $LaAlO_3$ and $SrTiO_3$, two insulating perovskite oxides.[1] This interface has been extensively studied since that initial report, with the discovery of a large number of other related electronic phenomena including superconductivity and magnetism.[1-5] Various combinations of other oxide compounds such as $NdAlO_3/SrTiO_3$, $PrAlO_3/SrTiO_3$, and $NdGaO_3/SrTiO_3$ form interfaces that are analogous to the $LaAlO_3/SrTiO_3$ interface and can also produce 2DEGs.[6] Those epitaxial complex-oxide heterostructures have been mostly fabricated by pulsed laser deposition (PLD) or molecular beam epitaxy (MBE).[7-10]

The creation of oxide interfaces exhibiting 2DEGs has been limited to planar geometries by the kinetic and geometric considerations of crystal growth from the vapor phase. As described throughout this thesis, solid-phase epitaxy (SPE) can be used to create epitaxial oxide interfaces with intricate geometries because this process faces a different set of kinetic constraints. The kinetics of SPE growth of amorphous $SrTiO_3$ thin films created by sputter deposition were described in Chapter 2 and Chapter 3.[11-12] One method for creating oxide films with SPE involves using atomic layer deposition (ALD) to grow amorphous A-B-O oxide thin films at low temperatures and followed by *ex situ* crystallization into epitaxial ABO_3 thin films.[13-14] ALD can be used to deposit thin films with precise control of the thickness and can be used to deposit

conformal thin films on high-aspect-ratio structures. In both cases, the key feature of the ALD process is the self-limiting growth mechanism.[15-17]

ALD has been widely employed for the deposition of binary oxides that can be used as high-dielectric-constant gate insulators in field-effect transistors for integrated circuits.[16,18-19] Studies of the use of ALD to create ternary-oxide thin films are, however, more limited because of the difficulty in controlling the two metal ion atomic ratios and the impurities in the deposited films.[16,18-21] One way to deposit ternary-oxide thin films by ALD is to combine the separate deposition processes for binary oxides and adjust the pulsing ratio to get the desired stoichiometry because the growth rates per cycle for both binary oxides are often different.[19] The ratio of the number of cycles used for the deposition of each binary oxide is termed pulsing ratio here.[20] The different optimum deposition temperatures for the binary oxides may lead to a narrow or non-existent temperature window for the deposition of ternary oxides. The A/B atomic ratio in the ALD of a ternary oxide ABO_3 cannot be selected by simply adjusting the A/B pulsing ratio because the atomic ratio is often not proportional to the ALD pulsing ratio.[20,22] For example, for the ALD of a ternary-oxide $SrTiO_3$ thin film, the atomic ratio of Sr/Ti of the deposited film is not proportional to the Sr/Ti pulsing ratio. A $SrTiO_3$ thin film with a Sr/Ti atomic ratio of 1:1 can be deposited by ALD with a range of Sr/Ti pulsing ratios varying from 0.67 to 0.82.[23]

Lanthanide aluminum oxide $LnAlO_3$ (Ln = La, Pr) thin films have previously been deposited by ALD using a lanthanum precursor, an aluminum precursor, and an oxidant.[21,24-25] Self-limiting growth of stoichiometric $LaAlO_3$ films was achieved with the use of the ALD precursors $La(thd)_3$, $Al(acac)_3$, and ozone. An important problem with this particular process was that the resulting $LaAlO_3$ films contained 0.8-1.9 atomic % carbon and 0.3 atomic % hydrogen as impurities.[21] In another study, the precursors $La(^{i}PrAMD)_3$, trimethylaluminum (TMA), and water

were employed to deposit $LaAlO_3$ films. The deposited films contained less than 1 atomic % carbon. These films were, however, Al-rich and there was no way to control the composition precisely because the process did not exhibit self-limiting growth.[24] $PrAlO_3$ films have been deposited by ALD using $Pr(amd)_3$, $AlMe_3$ and water.[25] Among the several samples reported, the composition closest to the stoichiometry is $Pr_{1.15}Al_{0.85}O_3$ using the Pr/Al pulsing ratio of 3:1.[25]

The deposition of amorphous ternary-oxide thin films with the desired stoichiometry and without impurities can be achieved with the design of new ALD chemical precursors and the development of new ALD procedures. A previous study showed that phase pure, epitaxial and misfit dislocation-free $BiFeO_3$ (001) thin films can be achieved on (001) STO substrates through a combination of the use of new ALD precursors for the deposition of amorphous $BiFeO_3$ thin films and the SPE growth.[26] A similar strategy is expected to work for the growth of epitaxial lanthanide aluminate thin films.

This chapter describes a series of collaborative studies that have resulted in the development of new lanthanide precursors. The collaboration was facilitated through the University of Wisconsin Materials Research Science and Engineering Center (MRSEC). The new precursors were designed, synthesized, and used for ALD deposition by Wathsala Waduge and Navoda Jayakodiarachchi in the laboratory of Professor Charles Winter at Wayne State University. The characterization of the lanthanide aluminate films shows that the film compositions can be controlled precisely because the new precursors exhibit self-limiting growth.

Creating epitaxial $PrAlO_3/SrTiO_3$ interfaces by SPE requires several important steps: (i) developing new ALD precursors and procedures for the deposition of stoichiometric amorphous $PrAlO_3$ thin films with high purity; (ii) understanding the differences in between the crystallization kinetics of amorphous $PrAlO_3$ deposited on substrates that present crystalline surfaces and the

crystallization on amorphous substrate surfaces; and (iii) characterizing the microstructures and interface structures of the crystallized thin films.

The novel Pr precursor synthesized at Wayne State University for this study was tris(isopropylcyclopentadienyl)praseodymium, which had the chemical formula $Pr(iPrC_5H_4)_3$. The ALD procedures for depositing $PrAlO_3$ films used precursors of $Pr(iPrC_5H_4)_3$, TMA, and water. All of the precursors exhibited self-limiting growth. The deposition process exhibits an ALD window and can be used to deposit $PrAlO_3$ films with constant Pr:Al ratios and without carbon contamination. The films are, however, not exactly stoichiometric with this set of precursors and, as described below, have approximately 20% excess Al.

A series of crystallization experiments reveals that the crystalline order of the substrate surface plays an important role in the crystallization kinetics. As-deposited $PrAlO_3$ films on SiO_2/Si substrates, which lack crystalline order, remained amorphous even after heating at 1000 ºC for 8 h. Epitaxial $PrAlO_3$ films on crystalline (001) $SrTiO_3$ (STO) substrates were achieved after crystallization at 800 ºC for 3 h. The examination of the interface structures shows that an epitaxial γ-Al_2O_3 layer formed at the interface during the growth by ALD and the epitaxial relationship of the crystallized film on STO was actually [001] $PrAlO_3$ // [001] Al_2O_3 // [001] STO.

The existence of the interfacial γ-Al_2O_3 layer points to potential directions for future work, including the electrical characterization of the interfaces in the epitaxial $PrAlO_3$/γ-Al_2O_3/STO thin films and the direct growth of pure amorphous $PrAlO_3$ films on STO by ALD. If the direct growth of pure amorphous $PrAlO_3$ on STO can be achieved, the study of the crystallization kinetics of amorphous $PrAlO_3$ on STO can be further conducted for the realization of using nanoscale seed crystals to create complex-oxide nanostructures with interesting electrical properties at the interfaces.

4.2 ALD growth of $PrAlO_3$ films

The ALD development and growth of $PrAlO_3$ films conducted by Wathsala Waduge in Prof. Winter's group at Wayne State University have been reported in a collaborative manuscript that has been submitted for publication.[27] The key aspects of the synthesis and deposition process are reported in this section.

The ALD procedures to deposit the binary oxides Pr_2O_3 were separately developed and then combined with the standard ALD procedures of Al_2O_3 to deposit $PrAlO_3$ films. First, the deposition of Pr_2O_3 was explored using the new Pr-containing precursor. The ALD procedures to deposit Pr_2O_3 were developed using $Pr(iPrC_5H_4)_3$ and water. The deposition studies revealed an ALD window for the growth of Pr_2O_3 with a constant growth rate of 0.85 Å/cycle from 275 to 325 ºC. A standard ALD process using TMA and water as precursors for the growth of Al_2O_3 was employed in this study because the growth rate of Al_2O_3 with this process is 1.0 Å/cycle at 300 ºC.[28] The close growth rates between Pr_2O_3 and Al_2O_3 allow the deposition of $PrAlO_3$ films with Pr:Al atomic ratio close to 1:1 using a 1:1 Pr/Al precursor pulsing ratio.

The experiments combining the two deposition processes for Pr_2O_3 and Al_2O_3 indicated that self-limiting growth of $PrAlO_3$ films can be achieved at 300 ºC with a pulse duration of greater than or equal to 3 s for $Pr(C_5H_4iPr)_3$, a pulse duration of greater than or equal to 0.1 s for $AlMe_3$, and a pulse duration of greater than or equal to 0.1 s for water. Figure 4-1 shows one ALD supercycle that was employed to deposit $PrAlO_3$ films with a 1:1 Pr/Al precursor pulsing ratio in this study. The detailed pulse and purge sequences and durations are also shown in Figure 4-1. Depositions were conducted on both Si substrates with native oxide and thermal SiO_2 on Si substrates. The Si substrates with native oxide are termed SiO_2/Si substrates, as used throughout

this thesis. The thermal SiO_2 on Si substrates are termed SiO_2 substrates in the following text. Similar growth behavior was observed on both substrates.

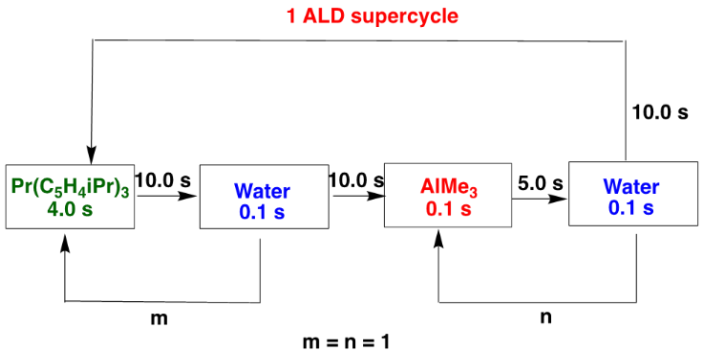

Figure 4-1. Pulse and purge sequences and durations for the deposition of $PrAlO_3$ films.

The temperature dependence of the growth rates of $PrAlO_3$ films was explored in a series of deposition experiments. An ALD window was observed for the growth of $PrAlO_3$ films, shown in Figure 4-2. The growth rate of $PrAlO_3$ is constant and has a value of 1.7 Å/cycle in a temperature range from 275 to 325 ºC. The increase of the growth rate at 375 ºC may originate from the thermal decomposition of TMA or $Pr(iPrC_5H_4)_3$ precursor.[29]

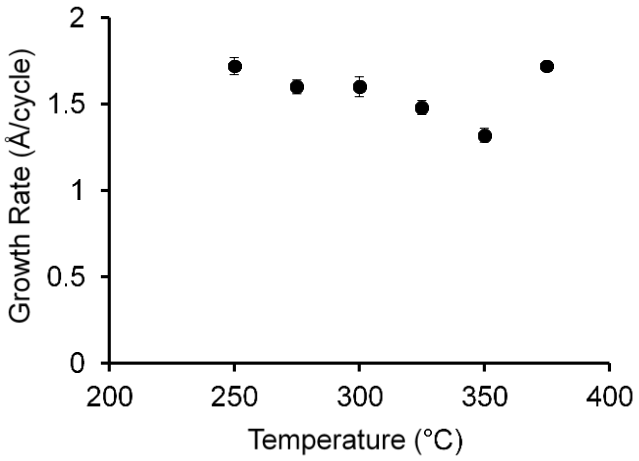

Figure 4-2. Growth rates of $PrAlO_3$ at different deposition temperatures using $Pr(iPrC_5H_4)_3$, TMA and water precursors with 250 cycles on SiO_2/Si substrates.

4.3 Characterization of the as-deposited $PrAlO_3$ films

4.3.1 Composition of the as-deposited $PrAlO_3$ films

The elemental composition of the as-deposited $PrAlO_3$ films and the oxidation state of each element were characterized using X-ray photoelectron spectroscopy (XPS). The XPS characterization was performed with a Thermo Scientific K-alpha XPS spectrometer using a microfocused monochromatic Al Kα X-ray source. XPS measurements were acquired for two 41-nm-thick $PrAlO_3$ films deposited on SiO_2/Si and SiO_2 substrates at 300 ºC. The XPS spectra and depth profiles of those two samples show essentially the same results. Only the XPS spectra and depth profile of the film deposited on the SiO_2 substrate are shown and discussed here. Figure 4-3 shows the XPS spectra of O 1s, Al 2p and Pr $3d_{5/2}$ for a $PrAlO_3$ film deposited on a SiO_2 substrate at 300 ºC. The binding energies of O1s, Al 2p and Pr $3d_{5/2}$ at 529.4 eV, 73.3 eV and 933.3 eV match well with the reported binding energies of those elements in the $PrAlO_3$ phase.[30-32] The satellite peak of Pr $3d_{5/2}$ at the binding energy of 929 eV has also been reported.[30,32] It is common that for the XPS measurement of Pr $3d_{5/2}$, a satellite peak appears at a binding energy of 4 eV lower than the peak maximum and the satellite peak has an intensity of 40% of the main peak.[30]

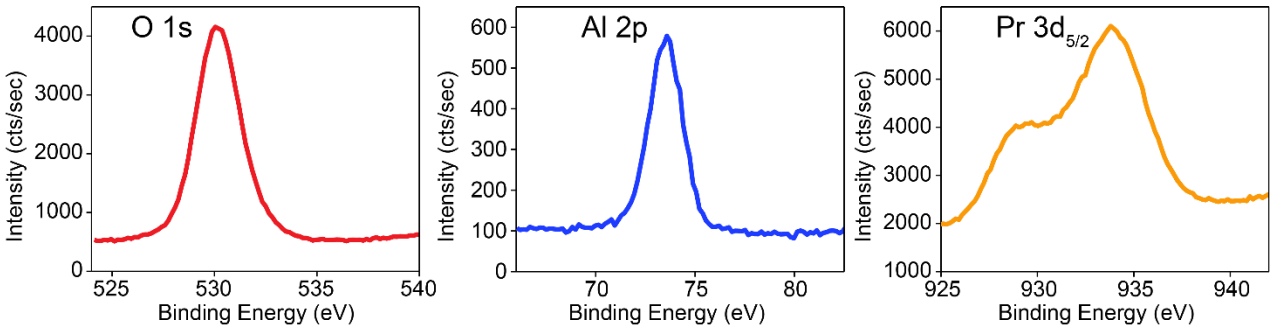

Figure 4-3 XPS spectra of O 1s, Al 2p and Pr $3d_{5/2}$ for a $PrAlO_3$ film deposited on a SiO_2 substrate at 300 ºC.

An XPS depth profile was acquired to determine the elemental composition as a function of the depth into the as-deposited $PrAlO_3$ film. The film was progressively removed by ion sputtering using a Ar^+ ion source. Spectra were acquired for the Si 2p, C 1s, Al 2p, Pr 3d, and O 1s spectral features. Figure 4-4(a) shows the XPS depth profile of a $PrAlO_3$ film deposited on a SiO_2 substrate at 300 ºC. No Si signal was observed for any depth in the film.

Figure 4-4(a) presents the atomic percentages of the elements C, Pr, Al and O as a function of Ar^+ etching time. The atomic percentage of each element was calculated based on the peak area of the spectra for C 1s, Pr 3d, Al 2p and O 1s shown in Figure 4-3 using the Thermo Avantage software (Thermo Fisher Corporation). The details of the calculation are shown as below.

The intensities constituting the peak above the background intensity are the signal from the electrons for a given transition of a specific element. The number of electrons for a given transition is proportional to the number of atoms. For an element A, the intensity of a peak (I_A) is thus proportional to the number of atoms (N_A). Each transition, such as C1s, Pr3d, or Al2p, has a probability of occurring and being detected, which is defined as the sensitivity factor (*SF*) for that transition. The detected number of electrons can also be affected by the depth of analysis, which corresponds approximately to the inelastic mean free path of electrons and depends on the composition of the material. An energy compensation factor (*ECF*) is used to correct for the inelastic mean free path term.[33] The following equation thus can be obtained:

$$N_A = \frac{I_A}{SF\ ECF}$$

Equation 4-1

A quantitative calculation of the atomic percentage of each element can be conducted by considering the intensity peak area of the spectra with a background subtraction for different

elements. A variety of background algorithms can be used to calculate the peak area.[33] A nonlinear Shirley background subtraction algorithm was used in this study.[34-35] The normalized peak area can be obtained from the peak area considering the sensitivity factor and energy compensation factor with the following equation:

$$NS_A = \frac{S_A}{SF\ ECF}$$

Equation 4-2

In Equation 4-2, NS_A is the normalized peak area considering the sensitivity factor and the energy compensation factor. S_A is the peak area of the element A with the background subtracted. The sensitivity factors in the library "ALTHERMO1" in the Thermo Avantage software were used for the analysis of the XPS data in this study. The energy compensation factors were also accessible in the Thermo Avantage software, which are the average values derived from a reported study.[36]

With the calculation of the normalized peak area for elements A, B, C and D, denoted as NS_A, NS_B, NS_C and NS_D, the atomic percentage of element A (f_A) can be calculated with the following equation:

$$f_A = \frac{NS_A * 100}{NS_A + NS_B + NS_C + NS_D}$$

Equation 4-3

The calculated atomic percentages of different elements depend on the choice of the algorithm for background subtraction, the different libraries used for sensitivity factors and energy compensation factors. The resulting atomic percentages can be different even with the same measured data. XPS can measure the absolute atomic concentrations within an accuracy of ±

10%.[37] XPS is good for quantitative comparison studies, but not for measurements of absolute numbers because of the uncertainty.

The atomic percentages of the four elements of a $PrAlO_3$ film on SiO_2 were determined with Equation 4-2 and Equation 4-3 using the Thermo Avantage software, as plotted in Figure 4-4(a). The rapid variation of the composition value for the first 30 s was caused by the presence of adventitious C on the sample surface. The atomic percentage of C on the sample surface is 25%. The atomic percentage of C is 1% at the etching time of 420 s and 1470 s, and 2% at the etching time of 540 s, 1050 s and 1260 s.

The validity of the atomic percentages of C in the sample can be verified by examining the XPS spectra of C 1s. Figure 4-4(b) shows a stack of the XPS spectra of C 1s at different depths of the same sample. There is an obvious peak at a binding energy of 285 eV for the spectrum of C 1s on the top sample surface, indicating that there is a measurable concentration of C on the sample surface. After the beginning of the etching process, however, the C peak is no longer measurable under these acquisition conditions.

The observed atomic percentage of C of 1% or 2% determined for regions inside the film at a few depths using the process above may thus not be accurate because no C 1s emission peaks were observed at those depths. Figure 4-4(c) shows the average of 10 spectra of C 1s measured at different depths inside the film. The C 1s emission peak was also not observed in the average spectrum. Obvious peaks can be observed in the XPS spectra of a specific transition of an element when the atomic percentage of that element is equal to or more than 2%. The observed atomic percentages of C vary slightly depending on the method used for the subtraction of the background. The resulting atomic percentages of C are, however, all below 2% no matter which method is used for the subtraction of the background. The average of the measured atomic percentages of C at

different depths inside the sample is 0.1%. C exists on the sample surface in the deposited film. The average atomic percentage of C inside the film detected by the XPS scans under these acquisition conditions is 0.1%.

In this study, the standard deviation of the values of the atomic percentages of the C, Pr, Al and O elements at all measured depths excluding the first data point measured for the composition of the sample surface is equal to or lower than 0.6%. The small standard deviation indicates that the overall Pr:Al atomic ratio is constant through the top layers of the films. The XPS measurements did not provide information about the composition of the interfacial layer between the film and the substrate because the Ar^+ etching time was not long enough to reach the interface.

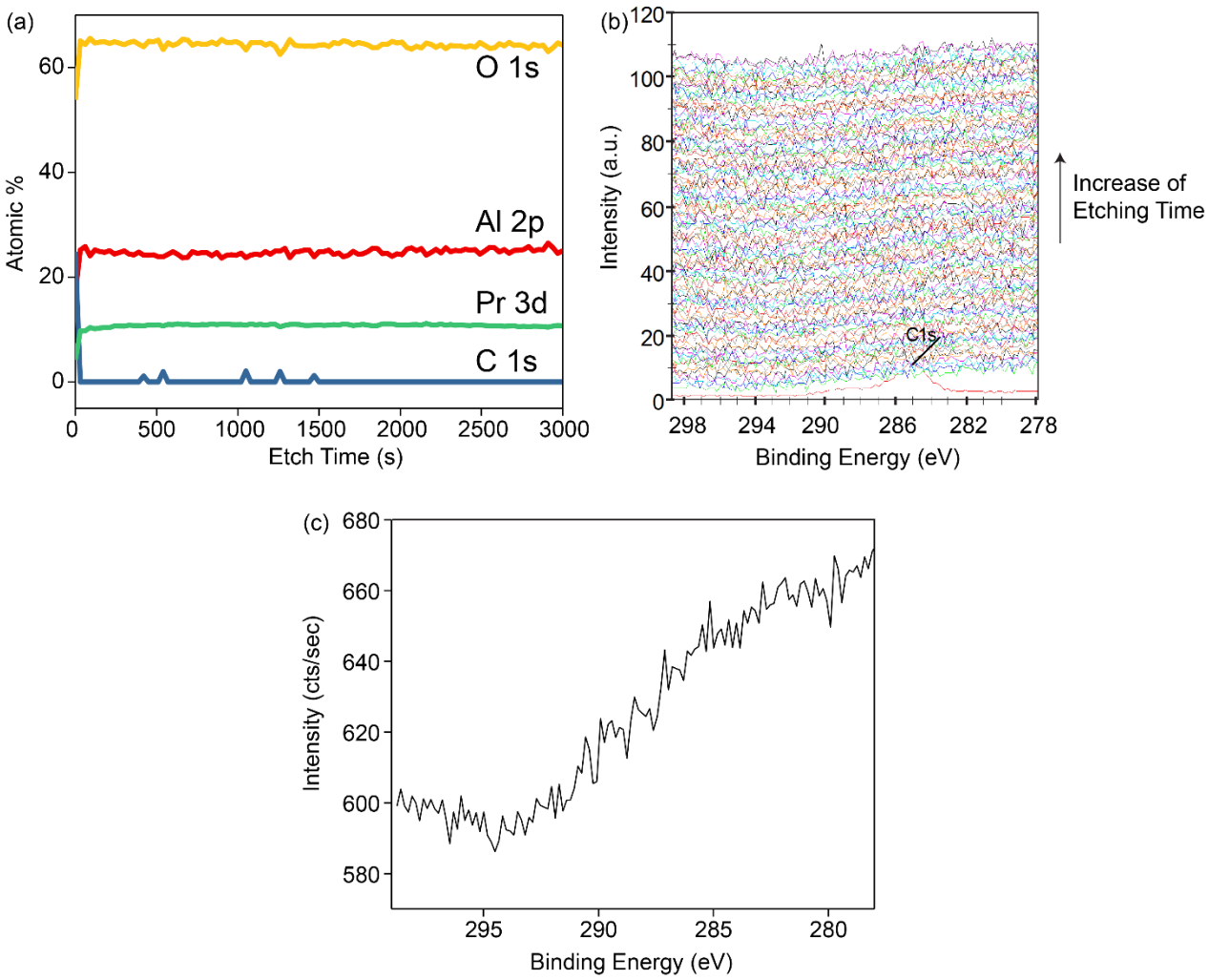

Figure 4-4. (a) XPS depth profile of a $PrAlO_3$ film deposited on a SiO_2 substrate at 300 ºC. (b) A stack of the XPS spectra of C 1s at different depths of the $PrAlO_3$ film deposited on a SiO_2 substrate at 300 ºC. (c) The average of 10 spectra of C 1s measured at different depths inside the film.

A more accurate measurement of the Pr:Al atomic ratios in the as-deposited $PrAlO_3$ films were obtained using electron probe microanalysis with X-ray wavelength dispersive spectroscopy (EPMA-WDS). The EPMA-WDS measurements were conducted by Dr. J. H. Fournelle in the Department of Geology and Geophysics at University of Wisconsin-Madison. Synthetic $PrPO_4$ was used as the reference standard for the measurement of the amount of Pr element in the films. Al_2O_3 was used as the reference standard for the measurement of the amount of Al and O elements in the films. Si was used as the reference standard for the measurement of Si element.

Characteristic X-ray intensities from the as-deposited films and the reference standards ($PrPO_4$, Al_2O_3, Si) were acquired at three different incident electron energies of 8, 12 and 20 keV. The compositions of the different elements in a film were determined by fitting the data at the three incident electron energies with a thin film model using a commercial program STRATAGem.[38]

The Pr:Al atomic ratios of the films grown with 1:1 Pr:Al precursor pulsing ratio at different temperatures within the ALD window were determined by EPMA-WDS and are shown in Table 4-1. The Pr:Al atomic ratios for the films deposited at temperatures of 300, 325, 350 and 375 ºC range from 1:1.25 to 1:1.39. The growth rates of the binary oxides Al_2O_3 and Pr_2O_3 within the ALD window were 1 Å/cycle and 0.85 Å/cycle, respectively.[28] The Pr:Al atomic ratio was estimated to be 1:1.18 based on the growth rates of Al_2O_3 and Pr_2O_3. The measured Pr:Al atomic ratio using EPMA-WDS is close to the estimated value. The Pr:Al atomic ratio of 1:1.71 for the film deposited at 250 ºC is higher than the atomic ratios of the films deposited at other deposition temperatures. The higher atomic ratio might be caused by the lower reactivity of the precursor $Pr(C_5H_4iPr)_3$ toward the surface reactive sites at 250 ºC.

Table 4-1. Pr:Al atomic ratio of the $PrAlO_3$ films deposited on SiO_2/Si substrates within the ALD window using EPMA-WDS.

Substrate temperature (°C)	Film thickness (nm)	Pr:Al precursor pulsing ratio	Pr:Al atomic ratio
250	51	1:1	1:1.71
300	41	1:1	1:1.25
325	37	1:1	1:1.39
350	33	1:1	1:1.26
375	44	1:1	1:1.26

The Pr:Al atomic ratio determined by EPMA-WDS differs from that derived from the XPS data. The difference arises because a standard XPS study employed here cannot provide accurate measurements of the absolute compositions due to the uncertainty in the analysis of the intensity data to obtain the atomic percentages as discussed above. The XPS data, however, can guide comparison study and are consistent with the reliable indication from EPMA-WDS measurements that the as-deposited films are Al-rich. The key piece of information from the XPS depth profiles is that the overall Pr:Al atomic ratio is constant through the top layers of the films and there is no carbon contamination within the films. The Ar^+ etching time in the XPS measurements was not long enough to detect the chemical compositions of the films that are in contact with the substrates. The TEM measurements described below, however, indicate that there are Pr/Al composition variations at very short length scales on the order of nanometers at the interfaces between the films and the substrates, perhaps due to pulse-to-pulse variations in the ALD process.

4.3.2 Structure of the as-deposited $PrAlO_3$ films

An as-deposited $PrAlO_3$ thin film grown by ALD on a SiO_2/Si substrate at 275 °C was characterized with grazing-incidence X-ray scattering employing the methods described in Section 1.4 of Chapter 1. The incident angles for $PrAlO_3$ on STO and $PrAlO_3$ on SiO_2/Si were selected to be 2.9° and 3°, respectively, because of the different sample size of $PrAlO_3$ films. The 2θ angle at the center of the detector was 30° for all measurements. Figure 4-5(a) shows a two-dimensional (2D) detector image spanning the range of 2θ angles from 13 to 45° for a grazing-incidence X-ray scattering of the as-deposited $PrAlO_3$ thin film. The angle χ is the azimuthal angle normal to the 2θ direction. Integrating the 2D detector image along the scattering ring azimuthal angle provides measurements of the scattered intensity as a function of 2θ. Figure 4-5(b) shows grazing-incidence X-ray scattering patterns acquired from a bare SiO_2/Si substrate and the as-deposited $PrAlO_3$ thin

film. The bare SiO_2/Si substrate exhibits a featureless low-intensity background. The X-ray scattering pattern of the as-deposited $PrAlO_3$ includes a broad intensity maximum centered at 2θ = 30°, indicating that the as-deposited $PrAlO_3$ layer is amorphous.

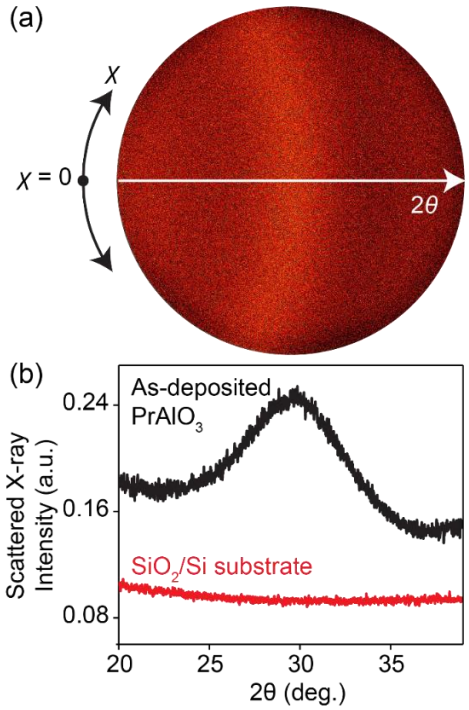

Figure 4-5. (a) 2D detector image spanning the range of 2θ angles from 13 to 45° for a grazing-incidence X-ray scattering study of a $PrAlO_3$ thin film deposited on a SiO_2/Si substrate at 275 °C. (b) Grazing-incidence X-ray scattering intensity as a function of 2θ angles for the as-deposited $PrAlO_3$ film (black). Scattered X-ray intensity from the bare SiO_2/Si substrate (red) is shown for comparison.

The thicknesses of the as-deposited amorphous $PrAlO_3$ films were determined by cross-sectional SEM. Figure 4-6(a) shows a cross-sectional SEM image of a $PrAlO_3$ film deposited on a SiO_2/Si substrate at 275 ºC. The film thickness is 41 nm.

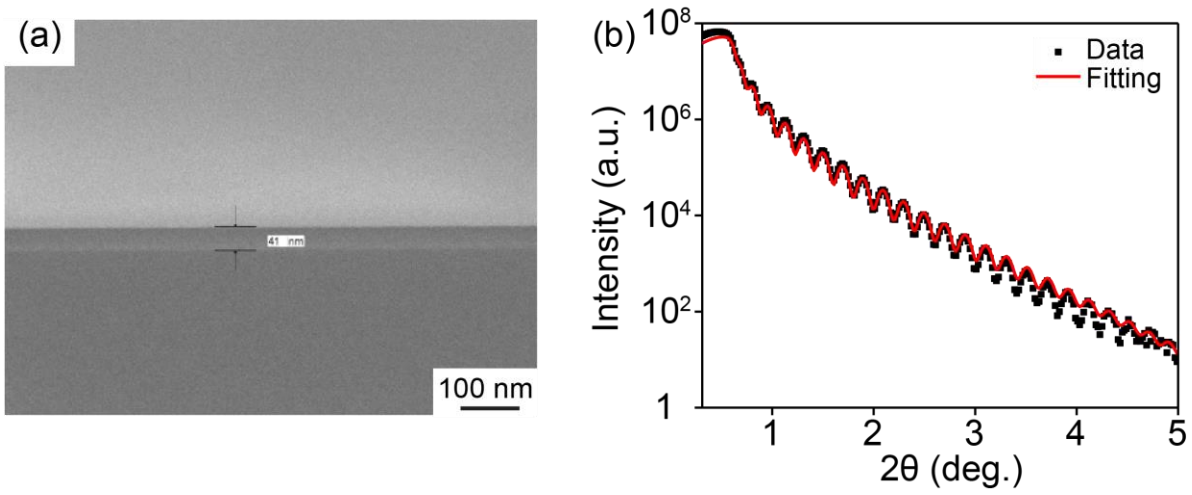

Figure 4-6. (a) Cross-sectional SEM image and (b) XRR measurement of a $PrAlO_3$ film deposited on a SiO_2/Si substrate at 275 ºC. The red line in (b) shows a calculated reflectivity curve using the parameters given in the text.

X-ray reflectivity (XRR) measurements provide further information about the thickness and roughness of the as-deposited amorphous $PrAlO_3$ thin film. XRR data were collected and analyzed using the same method introduced in the Section 2.3 of Chapter 2. Figure 4-6(b) shows the XRR data of the same sample for which the film thickness was measured by SEM in Figure 4-6(a). The XRR curve fit employed a three-layer model consisting of the $PrAlO_3$ film, native SiO_2, and the Si substrate. The densities of the SiO_2 and Si were set at 2.196 and 2.329 g cm^{-3}, respectively. There are not yet any available literature reports of the density of amorphous $PrAlO_3$. The density of amorphous $PrAlO_3$ was thus allowed to vary during the fitting. The best fit to the XRR data was obtained for an amorphous $PrAlO_3$ film with a density of 5.2 g cm^{-3}. The thickness of the as-deposited amorphous $PrAlO_3$ film and the surface rms roughness derived from the best fit are 42 nm and 0.6 nm, respectively. The thickness is consistent with the measurement of a 41-nm-thick $PrAlO_3$ film by SEM. The small rms roughness of 0.6 nm indicates that the as-deposited amorphous $PrAlO_3$ film is smooth.

4.4 Crystallization of amorphous $PrAlO_3$ films

A series of heating experiments were conducted to find out the conditions to fully crystallize the amorphous films. These experiments were first conducted with the $PrAlO_3$ films deposited on SiO_2/Si substrates that had a Al-rich composition with a constant Pr:Al atomic ratio. The films that had been deposited on SiO_2/Si substrates at 300 ºC were heated to temperatures ranging from 600 ºC to 1200 ºC by inserting the samples into a preheated tube furnace. The crystallization conditions were slightly different from those used for the STO samples described in Chapter 2 and Chapter 3. In the case of $PrAlO_3$, a constant O_2 gas flow was used during the heating processes.

All of the $PrAlO_3$ films on SiO_2/Si remained amorphous at an annealing temperature up to 1000 ºC. The X-ray diffraction study of the sample heated to 1200 ºC exhibited X-ray reflections for which the phases cannot be identified, which was possibly caused by the flow of materials and reaction with the substrate. The sample after heating at 1200 ºC showed darker blue areas with circular shapes which are distinct from the rest of the substrate surface, indicating that the materials started to melt and flow at this temperature. The sample heated to 1200 ºC is thus not discussed further below.

In order to observe the possible transition of the amorphous materials into crystalline phases for the $PrAlO_3$ films heated to different temperatures, grazing-incidence X-ray scattering measurements were conducted with the same X-ray data acquisition conditions used for the as-deposited amorphous film. Figure 4-7 shows the grazing-incidence X-ray scattering pattern of a $PrAlO_3$ film on SiO_2/Si after heating at 1000 ºC for 8 h. The broad intensity maximum at $2\theta = 27^\circ$ in Figure 4-7 is similar to the maximum observed in the as-deposited film and no new crystalline

X-ray reflections are apparent. The $PrAlO_3$ film remained amorphous even after heating at 1000 ºC for 8 h. Compared to the scattering pattern of the amorphous $PrAlO_3$ film shown in Figure 4-5, there is a slight broadening of the angular distribution of intensity and the intensity maximum shifts to $2\theta = 27^{o}$ from $2\theta = 30^{o}$. The broadening of the amorphous peak might also arise from a rearrangement of the amorphous structure, similar to what was observed at the early stages of crystallization of STO on SiO_2/Si as discussed in Section 2.5 of Chapter 2.

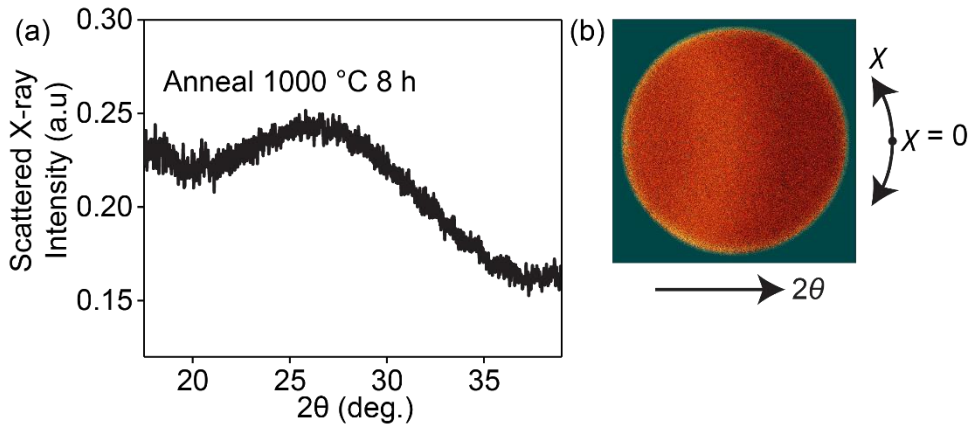

Figure 4-7. (a) Grazing-incidence X-ray scattering intensity for a $PrAlO_3$ film on a SiO_2/Si substrate after heating at 1000 ºC for 8 h. (b)2D detector image spanning the range of 2θ angles from 13 to 45° for the data in (a).

Amorphous $PrAlO_3$ on single-crystal (001) STO can crystallize into crystalline structures at temperatures lower than 1000 ºC, a temperature at which the $PrAlO_3$ films on SiO_2/Si remained amorphous. $PrAlO_3$ films on (001) STO substrates were deposited with the same ALD procedure as that was used for the deposition of $PrAlO_3$ films on SiO_2/Si substrates. Figure 4-8(a) shows grazing-incidence X-ray scattering patterns of a 206-nm-thick $PrAlO_3$ film deposited at 300 °C and a bare STO substrate. The bare STO substrate shows a featureless background for comparison. The broad peak centered at $2\theta = 30°$ indicates that the as-deposited $PrAlO_3$ film on STO is amorphous. Figure 4-8(b) shows the grazing-incidence X-ray scattering pattern of the $PrAlO_3$ film after crystallization at 800 ºC for 3 h. The intensity of the scattering in the amorphous peak

decreased to an immeasurably low level and only crystalline peaks are apparent in Figure 4-8(b). The results indicate that a 206-nm-thick amorphous $PrAlO_3$ film on STO can be fully crystallized with an 800 ºC 3 h heat treatment. The crystalline order of the substrate surface plays an important role in determining the crystallization kinetics of the amorphous $PrAlO_3$ film.

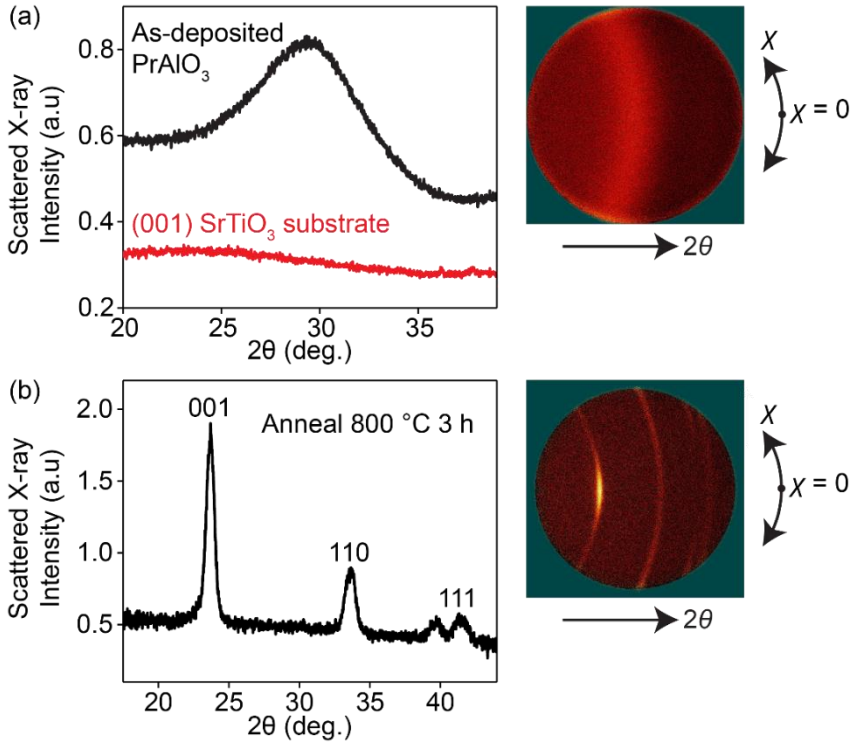

Figure 4-8. (a) Grazing-incidence X-ray scattering intensity for a $PrAlO_3$ film (black) deposited on a (001) STO substrate at 300 °C. Scattering intensity from the bare (001) STO substrate (red) is shown for comparison. The intensity of the as-deposited sample is shifted vertically by 0.3 to allow the curves to be distinguished. The 2D detector image spanning the range of 2θ angles from 13 to 45° for the as-deposited $PrAlO_3$ film is shown on the right. (b) Grazing-incidence X-ray scattering intensity of the $PrAlO_3$ film crystallized at 800 ºC for 3 h. The corresponding 2D detector image spanning the range of 2θ angles from 13 to 45° is shown on the right.

The phases and crystalline structure of the crystallized $PrAlO_3$ film on STO were examined in two separate X-ray diffraction measurements. First, a θ-2θ scan with a wide 10° step size in 2θ using the Bruker D8 Advance diffractometer was conducted in order to determine whether other crystalline phases are also present in the crystallized $PrAlO_3$ film. The measurement consisted of

4 steps with the 2θ angle at the center of the detector positioned at 10°, 20°, 30° and 40°, respectively. Figure 4-9(a) shows the sum of the scattered X-ray intensity from the crystallized film of the 4-step measurement. Figure 4-9(b) shows a stack of the 4 detector images with the 2θ angles ranging from 0 to 65°. Each detector image has a 2θ angle range of 32°. All of the crystalline peaks in Figure 4-9(a) can be indexed as arising from the crystalline $PrAlO_3$ phase except the 002 reflection of the STO substrate at the 2θ of 49°. The reflections were indexed based on the pseudocubic unit cell of $PrAlO_3$ with a lattice parameter of 3.772 Å.[40] The much higher intensities of $PrAlO_3$ 001 and 002 reflections indicate that the crystallized $PrAlO_3$ film is highly (001)-oriented, although polycrystalline grains in other directions are also present in the film. The (001)-oriented growth is more clearly visible from the corresponding 2D detector image in Figure 4-9(b), in which the $PrAlO_3$ (001) and (002) reflections have a broad intensity maximum in a limited range of χ angles.

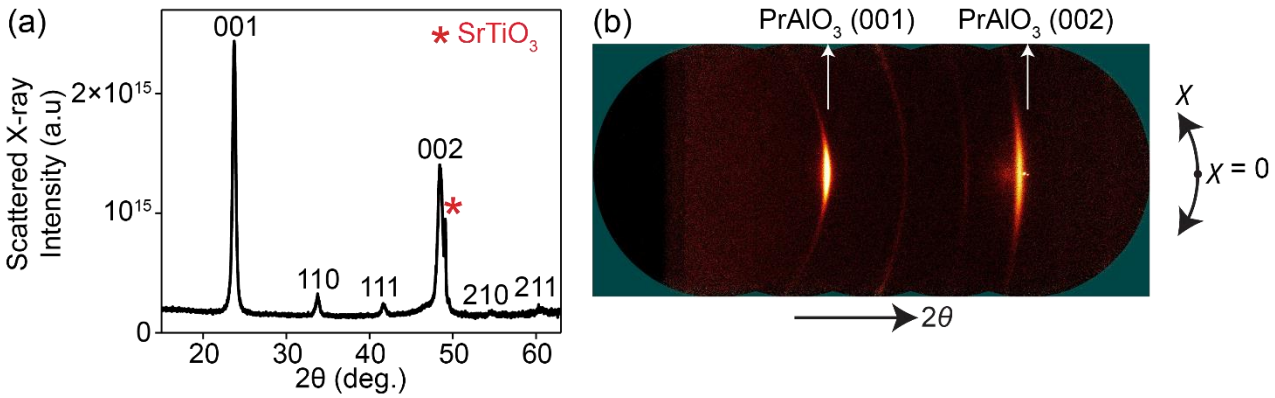

Figure 4-9. (a) X-ray scattering intensity of the $PrAlO_3$ film on (001) STO crystallized at 800 °C for 3h. The peak marked with a star is the diffraction from STO substrate. (b) A stack of the 2D detector images at the 4 steps generally spanning the range of 2θ angles from 0 to 65°.

The epitaxial relationship between the crystallized $PrAlO_3$ film and the (001) STO substrate was further examined by conducting a high-resolution θ-2θ scan. The experimental method was described in Section 1.6 of Chapter 1. Figure 4-10(a) shows a θ-2θ scan of the

crystallized $PrAlO_3$ film on STO with a step size of 0.04° in 2θ along the out-of-plane direction of the STO substrate. The $PrAlO_3$ 00L and STO 00L reflections appear on the same rod of reciprocal space, indicating that the amorphous $PrAlO_3$ film transforms into an epitaxial layer. The FWHM of the rocking curve of the $PrAlO_3$ (001) reflection, shown in Figure 4-10(b), is 7°. Figure 4-10(c) shows a scan of the azimuthal angle Φ of the in-plane 103 reflections of the crystallized $PrAlO_3$ film measured by the Bruker D8 Advance diffractometer. The four peaks corresponding to the 103 reflections of $PrAlO_3$ appear at 90º intervals in Φ, indicating that the crystallized $PrAlO_3$ film has a fourfold symmetry. This result further demonstrates that the crystallized $PrAlO_3$ film is epitaxial and shares the same in-plane orientation with the STO substrate.

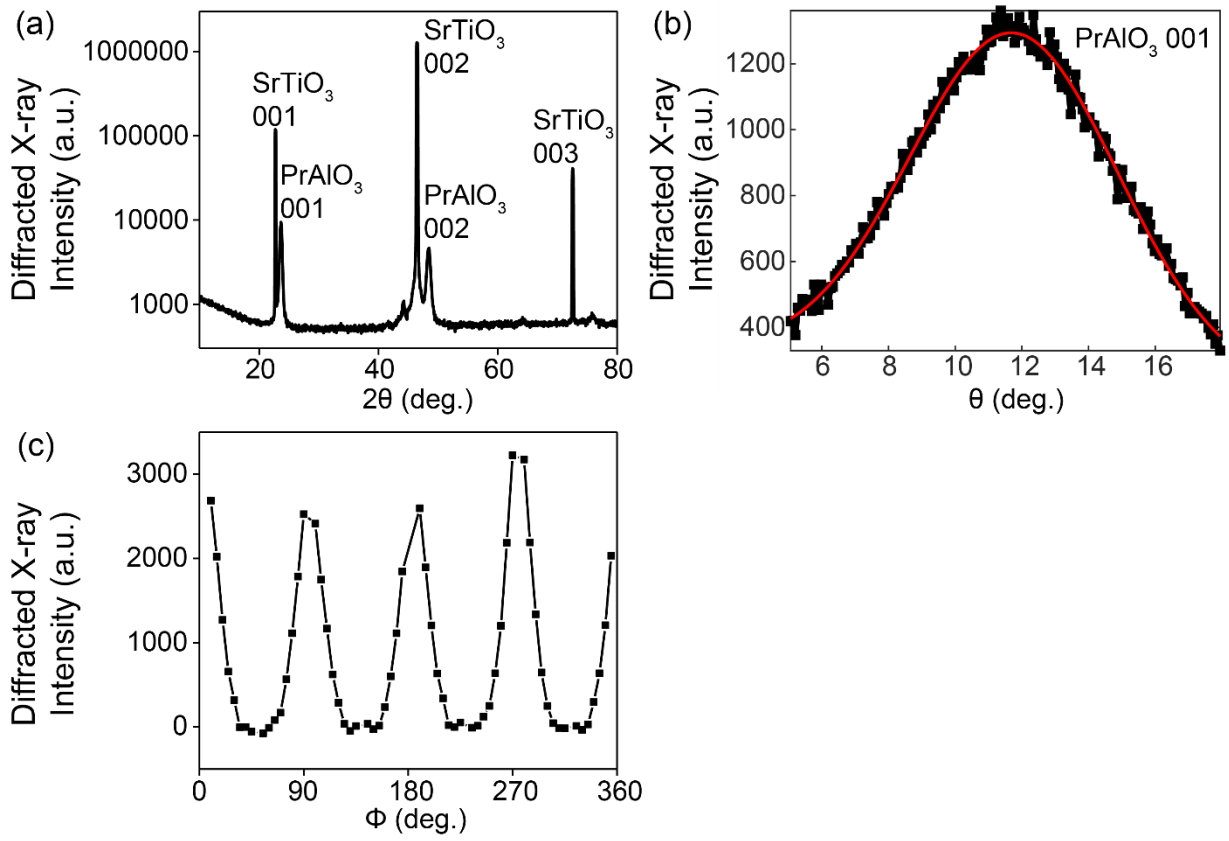

Figure 4-10. (a) X-ray scattering intensity along the substrate out-of-plane direction, (b) rocking curve scan of $PrAlO_3$ (001) reflection and (c) Φ scan of the in-plane 103 reflections of the $PrAlO_3$ film on (001) STO crystallized at 800 °C for 3h.

4.5 Characterization of the interface structure

The X-ray characterization reported in the previous section shows that the $PrAlO_3$ films are epitaxial when crystallized on the (001) STO substrates. Beyond this overall orientation, however, the X-ray measurement also indicates that the (001) reflection of the crystallized $PrAlO_3$ film has a large mosaic width of 7º, which shows that the film has a highly defective microstructure. Characterization of the interface structure between the film and the substrate is necessary to understand how to create epitaxial $PrAlO_3$ films with a smaller mosaic width. Scanning transmission electron microscopy (STEM) microanalysis is a good tool to provide detailed information about the microstructures of the film and the interface. The STEM measurements and crystal structure analysis in this section were conducted by Dr. Peng Zuo at UW-Madison through a collaboration supported by the University of Wisconsin MRSEC. An abrupt change of compositions was observed at the interface between the $PrAlO_3$ film and the STO substrate. An epitaxial crystalline γ-Al_2O_3 layer with a thickness of several nanometers formed at the interface between the amorphous $PrAlO_3$ layer and the (001) STO substrate during ALD at 300 ºC. The as-deposited amorphous and crystallized $PrAlO_3$ films have uniform compositions and structures.

The microstructure of an as-deposited 206-nm-thick $PrAlO_3$ film grown on (001) STO at 300 ºC was probed with STEM high-angle annular dark-field (HAADF) imaging, shown in Figure 4-11(a). The HAADF image appears brighter for the part of the sample with a larger atomic number (Z), because the contrast in a HAADF image is approximately proportional to Z^2. The as-deposited $PrAlO_3$ film and the STO substrate appear at the top and bottom of the image in Figure 4-11(a), respectively. A dark layer with a different composition appears at the interface between the film and the substrate.

Figure 4-11(b) shows a larger magnification of the interface structure marked with the red box in Figure 4-11(a). The interfacial layer is 5-nm thick. Energy dispersive X-ray spectroscopy (EDS) was conducted in the STEM for the same sample. Figure 4-11(c) shows the STEM-EDS line profiles of the Pr and Al elements across the sample interface. The EDS line profiles of the Pr and Al elements indicate that the concentrations of Pr and Al are constant throughout the top part of the as-deposited film and only Al is present in the interfacial layer.

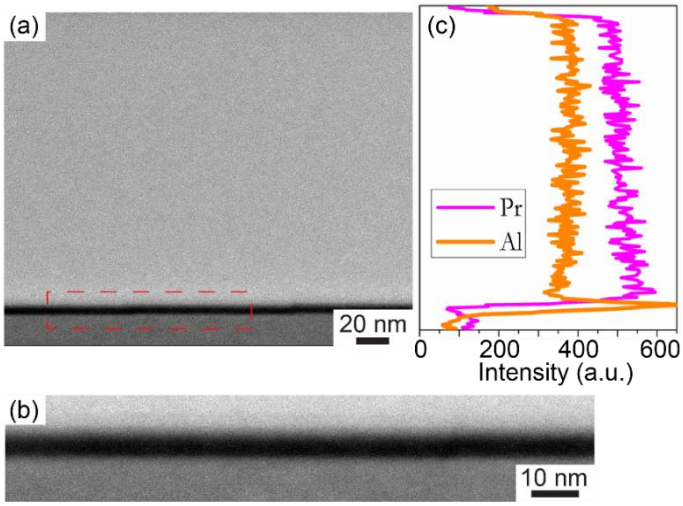

Figure 4-11. (a) STEM-HAADF image of an as-deposited 206-nm-thick $PrAlO_3$ film grown on (001) STO at 300 ºC. (b) STEM-HAADF image of the interface of the sample marked with the red box in (a). (c) STEM-EDS line profiles of Pr and Al elements across the sample interface.

A series of straightforward comparisons suggest that the interfacial layer is the γ-Al_2O_3 phase. Figure 4-12(a) shows a STEM-HAADF image with a higher magnification of the same sample measured in Figure 4-11. This image shows that the Al-rich interfacial layer is epitaxially grown on the STO substrate. The atomic planes of the interfacial layer align well with the STO substrate and have atomic spacings of 1.95 Å along both [001] and [100] directions. γ-Al_2O_3 has a cubic structure with a lattice parameter of 7.911 Å.[41] Figure 4-12(b) shows a schematic of a unit cell of γ-Al_2O_3 viewed along [010] direction. The spacings between Al atoms along both [001] and [100] directions of γ-Al_2O_3 are 1.975 Å, very close to the atomic spacings of 1.95 Å of the

interfacial layer observed in Figure 4-12(a). This comparison suggests that the interfacial layer is γ-Al_2O_3 and it is epitaxially grown on STO.

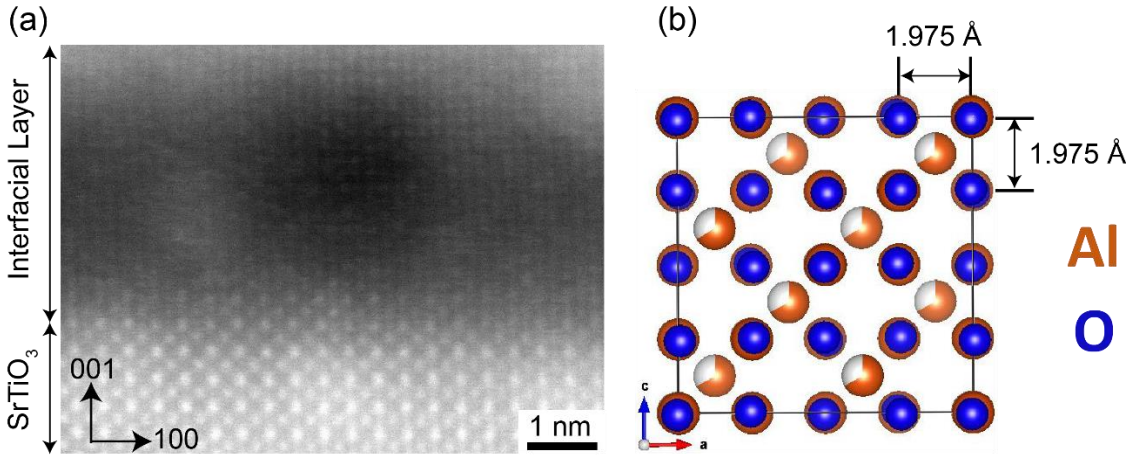

Figure 4-12. (a) STEM-HAADF image with a high magnification of an as-deposited 206-nm-thick $PrAlO_3$ film grown on (001) STO at 300 ºC. (b) Schematic of a unit cell of γ-Al_2O_3 viewed along [010] direction.

The formation of an epitaxial γ-Al_2O_3 layer between the as-deposited amorphous $PrAlO_3$ film and the STO substrate during deposition may affect the crystallization of the amorphous $PrAlO_3$ film. STEM analysis of the film crystallized at 800 ºC for 3 h provides more insight into the epitaxial relationship between the film, the interfacial layer and the substrate. Figure 4-13 shows a STEM-HAADF image of the 206-nm-thick $PrAlO_3$ film deposited on (001) STO and crystallized at 800 ºC for 3 h. Consistent with the observation in the X-ray diffraction studies, the crystallized $PrAlO_3$ film is highly (001)-oriented. The atomic planes of the $PrAlO_3$ film, the γ-Al_2O_3 layer and the STO substrate appear in the same 100 zone axis. The [001] and [100] orientations of $PrAlO_3$ align with the orientations of γ-Al_2O_3 and STO. Figure 4-13 shows the localized structure of a part of the sample measured with STEM. The slight misalignment between the film and substrate observed here is due to the misorientation of the $PrAlO_3$ lattice in the particular area imaged in Figure 4-13. The misorientation observed in Figure 4-13 is consistent

with the wide mosaic width of the $PrAlO_3$ 001 reflection observed using X-ray diffraction in Figure 4-10(b).

The (001)-oriented γ-Al_2O_3 interfacial layer existed between the $PrAlO_3$ film and the STO substrate before crystallization and the interfacial layer remained after crystallization. The crystallization of amorphous $PrAlO_3$ thus actually occurred on (001) γ-Al_2O_3 and the crystalline structure of the interfacial layer was not affected by the crystallization process. The epitaxial relationship of the crystallized sample is actually [001] $PrAlO_3$ // [001] Al_2O_3 // [001] STO. The original amorphous/crystalline interface structure plays an important role in determining the crystalline structure of the crystallized film formed by SPE growth.

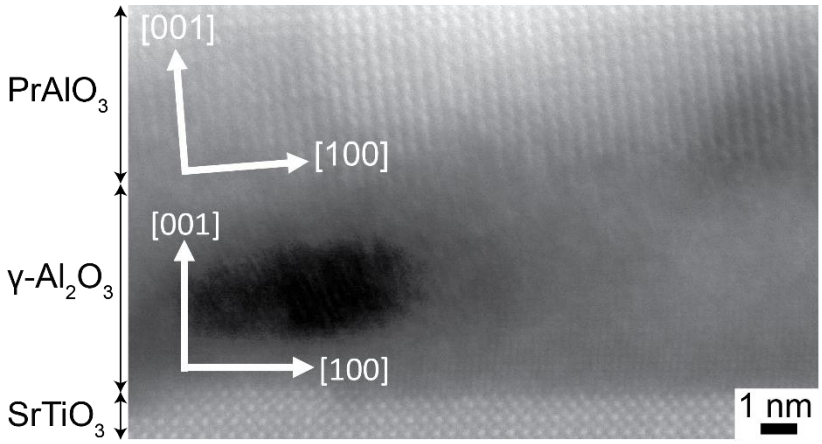

Figure 4-13. STEM-HAADF image of a 206-nm-thick film deposited on (001) STO and crystallized at 800 ºC for 3 h.

The examination of the crystal structures of the γ-Al_2O_3 and STO crystalline phases and several literature reports about the growth of γ-Al_2O_3 films on (001) STO substrates can help explain why an epitaxial γ-Al_2O_3 layer forms on (001) STO in the growth of amorphous $PrAlO_3$ films by ALD in this study. With the formation of an interfacial γ-Al_2O_3 layer, further examination of the crystal structures of $PrAlO_3$ and γ-Al_2O_3 crystalline phases can help understand why the crystallized $PrAlO_3$ film has a wide mosaic width of 7º.

The examination of the crystal structures of γ-Al_2O_3 and STO can explain why an epitaxial crystalline γ-Al_2O_3 layer formed on (001) STO during the deposition. STO has a cubic structure with a lattice parameter of 3.905 Å and γ-Al_2O_3 has a cubic structure with a lattice parameter of 7.911 Å.[41-42] The lattice parameter of γ-Al_2O_3 is about twice that of STO. Figure 4-14 shows schematics of the STO (001) and γ-Al_2O_3 (001) surfaces viewed along [001] directions. The oxygen sublattices between STO and γ-Al_2O_3 phases closely match although the cation sublattices of those two phases are different. The lattice mismatch between STO and γ-Al_2O_3 is 1.3%. The close oxygen sublattices and small lattice mismatch enable γ-Al_2O_3 to grow epitaxially on (001) STO during the deposition.

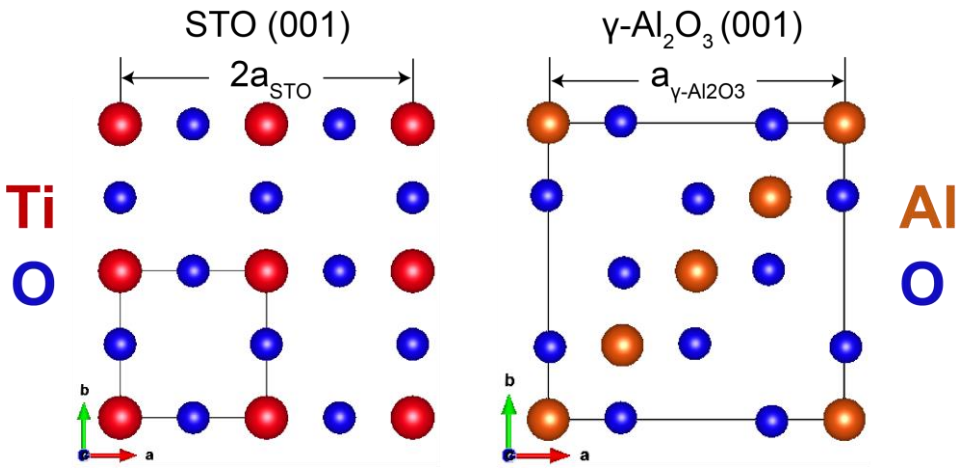

Figure 4-14. Schematics of STO (001) and γ-Al_2O_3 (001) surfaces viewed along [001] direction.

More specific studies in the literature about the growth of only epitaxial γ-Al_2O_3 layers on (001) STO revealed the fundamental mechanisms to form the epitaxial γ-Al_2O_3 phase on (001) STO. Epitaxial γ-Al_2O_3 layers were grown on (001) STO using ALD, MBE and PLD.[43-46] A previous ALD study reported that Al_2O_3 phase with different crystalline order forms at different deposition temperatures and explained why γ-Al_2O_3 phase forms on STO when TMA was used as the precursor.[43] The ALD growth of only Al_2O_3 phase on (001) STO substrates was carried out

using TMA and water as precursors at deposition temperatures of 200-345 ºC.[43] The as-deposited Al_2O_3 film was amorphous at a deposition temperature of 200 ºC and the as-deposited film was epitaxial γ-Al_2O_3 crystalline phase when the deposition temperature was equal to or more than 300 ºC.[43] The reaction between TMA and STO can lead to the formation of Al_2O_3 at 300 ºC even without supplying H_2O.[43] TMA was one of the precursors for the deposition of amorphous $PrAlO_3$ films and the growth rate of Al_2O_3 was larger than that of Pr_2O_3 in this study. The easy reaction between TMA and STO may lead to the formation of γ-Al_2O_3 phase at the interface between the $PrAlO_3$ film and the STO substrate, and the deposition temperature of 300 ºC causes the formation of epitaxial crystalline γ-Al_2O_3 phase. The epitaxial growth of crystalline γ-Al_2O_3 films on (001) STO has also been extensively studied using other deposition methods including MBE at temperatures of 400-800 ºC and PLD at temperatures of 20-700 ºC.[44-46] High-quality epitaxial γ-Al_2O_3 thin films can be grown on (001) STO by PLD even at room temperature, which provides the opportunities to fabricate nanoelectronic devices based on oxides.[45]

With the understanding why epitaxial γ-Al_2O_3 layer formed at the interface between the as-deposited amorphous $PrAlO_3$ film and the STO substrate, the examination of the crystal structures of $PrAlO_3$ and γ-Al_2O_3 phases can help explain why the crystallized $PrAlO_3$ film on top of γ-Al_2O_3 has a wide mosaic width. The interfacial epitaxial γ-Al_2O_3 layer plays a key role in determining the crystalline structure of the $PrAlO_3$ film after crystallization. $PrAlO_3$ has a rhombohedral crystal structure with lattice parameters a = b = c = 5.304 Å and α = β = γ = 60.32º. The crystal structure of $PrAlO_3$ can be considered as a pseudocubic structure with a lattice parameter of 3.772 Å or it can be considered as a face-centered cubic structure with a lattice parameter of 7.544 Å. Figure 4-15 shows the schematics of $PrAlO_3$ (001) and γ-Al_2O_3 (001) surfaces viewed along [001] directions. Similar to the epitaxial growth of γ-Al_2O_3 phase on STO

shown in Figure 4-14, $PrAlO_3$ can grow epitaxially on γ-Al_2O_3 because of the good match of their oxygen sublattices as shown in Figure 4-15. The lattice mismatch between $PrAlO_3$ and γ-Al_2O_3 is, however, as large as 5%. The large lattice mismatch leads to the formation of an epitaxial $PrAlO_3$ film on γ-Al_2O_3 with a wide mosaic width of 7º.

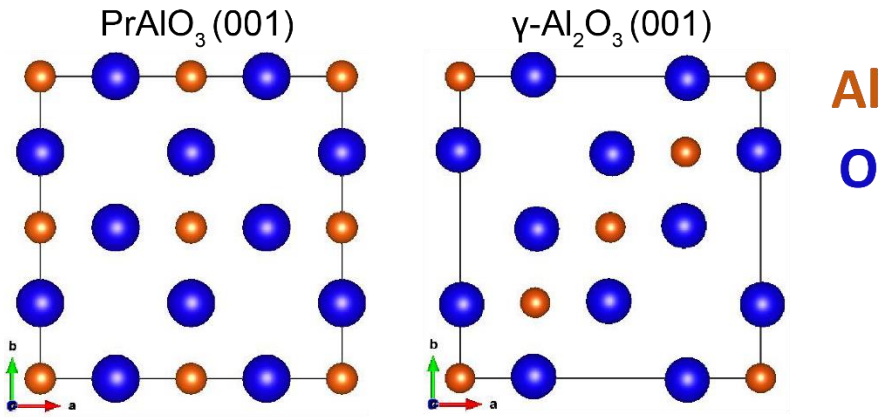

Figure 4-15. Schematics of $PrAlO_3$ (001) and γ-Al_2O_3 (001) surfaces viewed along [001] direction.

4.6 Future work

4.6.1 Electrical measurements

The original goal of this study was to form epitaxial $PrAlO_3$/STO heterostructures by SPE and characterize the electronic properties of the interfaces. With the formation of the epitaxial γ-Al_2O_3 layer between the epitaxial $PrAlO_3$ film and the STO substrate discussed in the previous section, the new interface structures can still possibly have promising electronic properties.

The formation of a 2DEG at the interface between the epitaxial γ-Al_2O_3 and (001) STO was reported in the literature.[43-46] Because of the better lattice match and the well-defined interface structure between γ-Al_2O_3 and STO, their interface exhibited an even higher mobility than the perovskite-oxide heterostructures.[43-46] The electronic properties of the γ-Al_2O_3/STO system depend on the deposition methods, the growth temperatures and the thickness of the γ-Al_2O_3

layer.[43-44,46] The results of the electrical measurement of the γ-Al_2O_3/STO system reported in the literature are briefly summarized as below. The sample with a 6-nm-thick γ-Al_2O_3 layer on STO grown by MBE at 700 ºC had an electron mobility of 3100 $cm^2 V^{-1} s^{-1}$ at 3.2 K and a mobility of 22 $cm^2 V^{-1} s^{-1}$ at room temperature.[44] The electron mobility of a γ-Al_2O_3/STO interface can be larger than 10^4 $cm^2 V^{-1} s^{-1}$ at 2 K for a γ-Al_2O_3 layer grown by PLD at 600 ºC, with a thickness larger than 2 unit cells (u.c.) but smaller than 3 u.c.[46] For a 2.5-nm-thick γ-Al_2O_3 layer deposited by PLD at room temperature, the electron mobility is 3200 $cm^2V^{-1}s^{-1}$ at 2 K.[45] For a 2.1-nm-thick γ-Al_2O_3 layer grown by ALD at 345 ºC, the electron mobility is 3000 $cm^2V^{-1}s^{-1}$ at 15 K.[43] The presence of oxygen vacancies on the STO side close to the interface was reported to be the mechanism causing the formation of 2DEG at the γ-Al_2O_3/STO interfaces.[43-44,46-47] Post-deposition annealing in oxygen reduced the carrier density and suppressed electron conductivity.[43-44,46-47]

Given the promising electronic properties of the γ-Al_2O_3/STO interfaces, it's worth looking into the electronic properties of the $PrAlO_3$/γ-Al_2O_3/STO samples before and after crystallization of the amorphous $PrAlO_3$ layers as a future work. The following questions might be of scientific interests: Whether the γ-Al_2O_3/STO interfaces prepared in this study by ALD also have oxygen vacancies and thus have high electron mobilities even when the γ-Al_2O_3 layers are covered with the amorphous $PrAlO_3$ layers; If they have, whether heating of $PrAlO_3$/Al_2O_3/STO samples in oxygen can also reduce the carrier density at the γ-Al_2O_3/STO interfaces depending on whether $PrAlO_3$ can function as a barrier layer.

4.6.2 Composition of the as-deposited films

As discussed in the previous section, an extra γ-Al_2O_3 layer formed at the interface because of the larger growth rate of Al_2O_3 than that of Pr_2O_3 and the easy reaction between the precursor TMA and STO. The creation of epitaxial $PrAlO_3$/STO heterostructures by SPE still requires the

deposition of pure amorphous $PrAlO_3$ films on STO substrates without extra interfacial layers. Future work might include the optimization of the composition of the as-deposited films by matching the growth rates of Pr_2O_3 and Al_2O_3 to create pure $PrAlO_3$ films on STO. The growth rate of Pr_2O_3 has already been increased by using the $Pr(C_5H_4iPr)_3$ precursor in this study compared with the prior Pr precursors.[48] Navoda Jayakodiarachchi in Prof. Winter's group at Wayne State University is now developing of other Pr precursors to have higher growth rates of Pr_2O_3 that match the growth rates of Al_2O_3 using the TMA and water precursors. Another strategy is to change the ALD precursors for the growth of Al_2O_3 with lower growth rates. For example, the growth rate of Al_2O_3 using TMA and isopropanol is 0.8 Å/cycle at 250 ºC, closely matching the growth rate of Pr_2O_3 of 0.85 Å/cycle using the $Pr(C_5H_4iPr)_3$ and water precursors reported in this study.[49]

4.6.3 Crystallization kinetics of amorphous $PrAlO_3$ on STO

As introduced in Chapter 2 and Chapter 3, the study of the crystallization kinetics of amorphous oxide layers on substrate surfaces with different crystalline order can facilitate the creation of complex-oxide single crystals in nanoscale geometries.[11-12] The crystallization kinetics of $PrAlO_3$ on STO is particularly important for the creation of $PrAlO_3$/STO heterostructures employing nanoscale STO seed crystals. Some studies have been conducted to measure the rates of crystallization of amorphous $PrAlO_3$ layers on STO. The existence and variation of the thickness of the interfacial γ-Al_2O_3 layer prohibits a consistent quantitative study about the rates of crystallization. Future work about the crystallization kinetics of amorphous $PrAlO_3$ on STO can build on what has been done and reported in this section.

An amorphous $PrAlO_3$ film on a SiO_2/Si substrate remained amorphous even after heating at 1000 ºC for 8 h and an amorphous $PrAlO_3$ film on a (001) STO substrate was fully crystallized

after heating at 800 ºC for 3 h, as discussed in Section 4.4 of this Chapter. The crystallization of $PrAlO_3$ films with the nominally same thickness on (001) STO at different temperatures ranging from 500 ºC to 800 ºC was investigated to study the crystallization kinetics of $PrAlO_3$ films. An amorphous $PrAlO_3$ film on (001) STO can be fully crystallized after heating at 800 ºC for 1 h. X-ray diffraction studies of the film crystallized at 800 ºC for 1 h showed the same crystalline structure as the film crystallized at 800 ºC for 3 h for which the crystalline structure was characterized in Section 4.4 and 4.5 of this Chapter. When the crystallization temperature was equal to or lower than 700 ºC, an $PrAlO_3$ film remained amorphous after a relatively long heating duration. Figure 4-16 shows the evolution of the scattered X-ray intensity of an amorphous $PrAlO_3$ layer on (001) STO after heating at 700 ºC for two different duration. The data were acquired in two separate heating steps, each of which was followed by X-ray scattering characterization. The X-ray intensity of scattering from the amorphous $PrAlO_3$ was calculated by integrating the intensity over the 2theta range from 25º to 33º to avoid the (001) and (110) crystalline peaks. The intensity of scattering from the amorphous $PrAlO_3$ in the film heated to 700 ºC for 8 h is 96% of that in the as-deposited film. The intensity of scattering from the amorphous $PrAlO_3$ in the film heated to 700 ºC for 16 h is 95% of that in the as-deposited film. A large amount of the film thus remained amorphous even after heating at 700 ºC for 16 h.

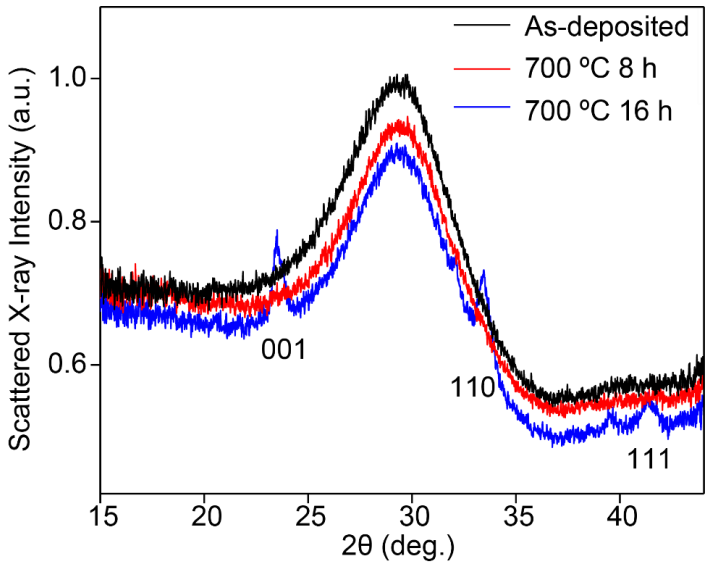

Figure 4-16. Grazing-incidence X-ray scattering intensity for an as-deposited $PrAlO_3$ film on STO (black) and after heating at 700 ºC for 8 h (red) and 16 h (blue). Crystalline peaks corresponding to $PrAlO_3$ 001, 110 and 111 reflections appear for the film heated at 700 ºC for 16 h.

The crystallization kinetics can be studied by examining the structure of partially crystallized $PrAlO_3$ layers. The lowest temperature at which partially crystallized $PrAlO_3$ films can be achieved in a relatively short heating duration is 750 ºC. The time dependence of the X-ray intensity of scattering from the amorphous $PrAlO_3$ layer on STO at 750 ºC is shown in Figure 4-17(a). The amorphous $PrAlO_3$ scattered X-ray intensity decreases after heating at 750 ºC for 20 min. Obvious crystalline peaks evolve after heating at 750 ºC for 80 min. A more quantitative study to measure the rate of crystallization of $PrAlO_3$ at 750 ºC was not completed because inconsistent results were obtained for the 4 samples deposited and crystallized at 750 ºC under the same conditions. For example, sample A and sample B were both deposited using the same ALD procedure and crystallized at 750 ºC for 3 h under the same conditions. The grazing-incidence X-ray scattering measurements of those two samples in Figure 4-17(b) show that the intensity of scattering from the amorphous $PrAlO_3$ in sample A remains and is 21% of that in the as-deposited amorphous film. The intensity of scattering from the amorphous $PrAlO_3$ in sample B is, however,

0.1% of that in the as-deposited amorphous film, very close to 0, as pointed out by the black arrow. The results indicate that part of the amorphous $PrAlO_3$ film in sample A was not crystallized yet, but the whole amorphous $PrAlO_3$ film in sample B was fully crystallized.

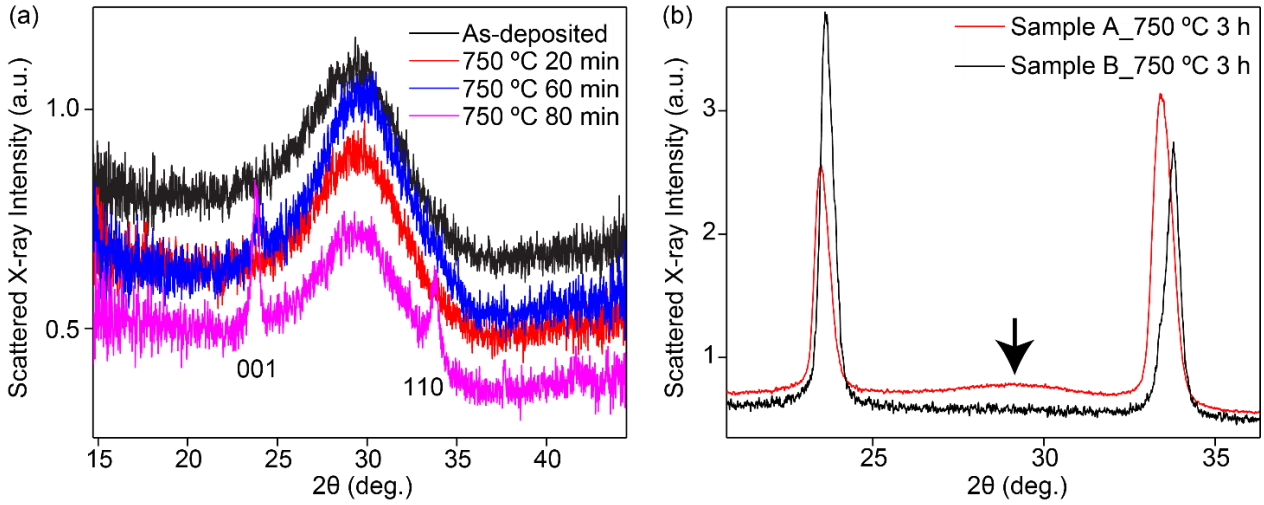

Figure 4-17. (a) Grazing-incidence X-ray scattering intensity for an as-deposited $PrAlO_3$ film on STO (black) and after annealing at 750 ºC for 20 min (red), 60 min (blue), and 80 min (magenta). (b) Grazing-incidence X-ray scattering intensity for sample A (red) and sample B(black). They are two samples prepared with the same growth conditions and both were heated at 750 ºC for 3 h under the same condition.

The inconsistent results of the crystallization experiments can in principle arise from a differing thickness of the interfacial γ-Al_2O_3 layer in different samples, perhaps due to pulse-to-pulse variations in the ALD process. STEM-HAADF images of three films grown on (001) STO with the same ALD process but with different heating treatments show that the thickness of the interfacial γ-Al_2O_3 layer varies from sample to sample. Figure 4-18(a), (b), and (c) show the STEM-HAADF images of an as-deposited film, a film crystallized at 750 ºC for 3 h and a film crystallized at 800 ºC for 1 h, respectively. The thickness of the dark interfacial γ-Al_2O_3 layer for those three samples is 6 nm, 3 nm and 8 nm, respectively. The different thickness of the γ-Al_2O_3 layer indicates that the thickness of the $PrAlO_3$ film also varies from sample to sample. The differing thickness of the $PrAlO_3$ film poses challenges to study the crystallization kinetics of

$PrAlO_3$ because the crystallization time to fully crystallize a film largely depends on the thickness of the original amorphous layer.

Further work on developing procedures to deposit stoichiometric $PrAlO_3$ films directly on STO substrates with a precise control of the film thickness will enable the further study of the crystallization kinetics of $PrAlO_3$ on STO. With the samples in this study, an amorphous $PrAlO_3$ film on γ-Al_2O_3 can be partially crystallized at 750 ºC within a relatively short duration to study the rates of crystallization. Better lattice match between $PrAlO_3$ and STO than that between $PrAlO_3$ and γ-Al_2O_3 may allow amorphous $PrAlO_3$ layers to crystallize at a lower temperature than 750 ºC within a shorter duration.

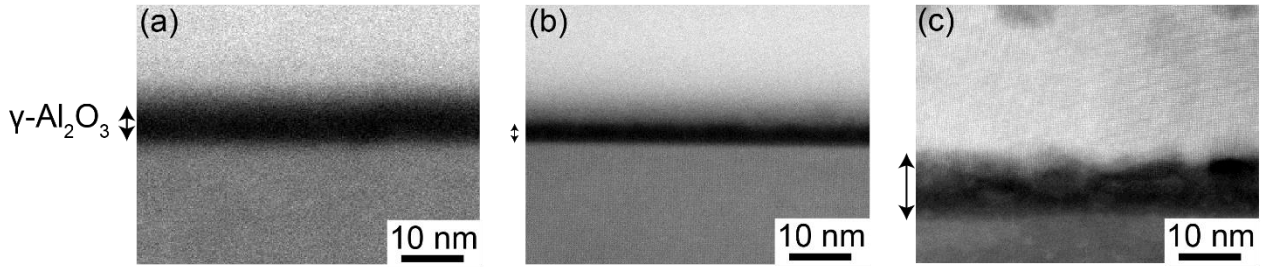

Figure 4-18. STEM-HAADF images of 3 samples grown on STO with the same ALD process, but with different heating treatment: (a) an as-deposited film; (b) a film crystallized at 750 ºC for 3 h; (c) a film crystallized at 800 ºC for 1 h. The arrows indicate the interfacial γ-Al_2O_3 layer.

4.7 Conclusions

The group of Prof. Charles Winter at Wayne State University developed the ALD procedures to deposit $PrAlO_3$ films using $Pr(iPrC_5H_4)_3$, TMA, and water as precursors. Self-limiting growth was demonstrated in each precursor at 300 ºC, and an ALD window was observed from 275 to 325 ºC with a growth rate of 1.7 Å/cycle for the growth of $PrAlO_3$ films. The as-deposited films are overall Al-rich, free of carbon contamination and exhibit smooth surfaces. The

Al-rich compositions of the as-deposited films originate from the larger growth rate of Al_2O_3 than that of Pr_2O_3, leading to the formation of epitaxial γ-Al_2O_3 layers at the interfaces between the $PrAlO_3$ films and the STO substrates.

The crystalline order of the substrate surface plays an important role in the crystallization kinetics. As-deposited $PrAlO_3$ films on SiO_2/Si substrates remained amorphous even after heating at 1000 ºC for 8 h. Epitaxial $PrAlO_3$ films on (001) STO substrates were achieved after crystallization at 800 ºC for 3 h. The epitaxial relationship of the crystallized film on STO was actually [001] $PrAlO_3$ // [001] γ-Al_2O_3 // [001] STO because of the formation of the epitaxial γ-Al_2O_3 layer at the interface during the deposition. Directions for future work are suggested in the end, including the electrical measurement of the interfaces in the epitaxial $PrAlO_3$/γ-Al_2O_3/STO thin films, the direct growth of pure amorphous $PrAlO_3$ films on STO by ALD, and more complete kinetics study of the crystallization of amorphous $PrAlO_3$ films on STO substrates for the creation of complex-oxide nanostructures using seed crystals. This study demonstrates the opportunities to create the lanthanide aluminum oxide and STO heterostructures in new geometries by combining the use of ALD and SPE.

4.8 References

1. Ohtomo, A.; Hwang, H. Y. A High-Mobility Electron Gas at the $LaAlO_3$/$SrTiO_3$ Heterointerface. *Nature* **2004,** *427* (6973), 423-426.
2. Reyren, N.; Thiel, S.; Caviglia, A. D.; Kourkoutis, L. F.; Hammerl, G.; Richter, C.; Schneider, C. W.; Kopp, T.; Ruetschi, A. S.; Jaccard, D.*; et al.* Superconducting Interfaces between Insulating Oxides. *Science* **2007,** *317* (5842), 1196-1199.
3. Brinkman, A.; Huijben, M.; Van Zalk, M.; Huijben, J.; Zeitler, U.; Maan, J. C.; Van der Wiel, W. G.; Rijnders, G.; Blank, D. H. A.; Hilgenkamp, H. Magnetic Effects at the Interface between Non-Magnetic Oxides. *Nat. Mater.* **2007,** *6* (7), 493-496.
4. Thiel, S.; Hammerl, G.; Schmehl, A.; Schneider, C. W.; Mannhart, J. Tunable Quasi-Two-Dimensional Electron Gases in Oxide Heterostructures. *Science* **2006,** *313* (5795), 1942-1945.

5. Ariando; Wang, X.; Baskaran, G.; Liu, Z. Q.; Huijben, J.; Yi, J. B.; Annadi, A.; Barman, A. R.; Rusydi, A.; Dhar, S.*; et al.* Electronic Phase Separation at the $LaAlO_3/SrTiO_3$ Interface. *Nat. Commun.* **2011,** *2*.
6. Annadi, A.; Putra, A.; Liu, Z. Q.; Wang, X.; Gopinadhan, K.; Huang, Z.; Dhar, S.; Venkatesan, T.; Ariando Electronic Correlation and Strain Effects at the Interfaces between Polar and Nonpolar Complex Oxides. *Phys. Rev. B* **2012,** *86* (8).
7. Cantoni, C.; Gazquez, J.; Granozio, F. M.; Oxley, M. P.; Varela, M.; Lupini, A. R.; Pennycook, S. J.; Aruta, C.; di Uccio, U. S.; Perna, P.*; et al.* Electron Transfer and Ionic Displacements as the Origin of the 2D Electron Gas at the LAO/STO Interface: Direct Measurements with Atomic-Column Spatial Resolution. *Adv. Mater.* **2012,** *24* (29), 3952-3957.
8. Chambers, S. A. Epitaxial Growth and Properties of Doped Transition Metal and Complex Oxide Films. *Adv. Mater.* **2010,** *22* (2), 219-248.
9. Mannhart, J.; Schlom, D. G. Oxide Interfaces-An Opportunity for Electronics. *Science* **2010,** *327* (5973), 1607-1611.
10. Huijben, M.; Brinkman, A.; Koster, G.; Rijnders, G.; Hilgenkamp, H.; Blank, D. H. A. Structure-Property Relation of $SrTiO_3/LaAlO_3$ Interfaces. *Adv. Mater.* **2009,** *21* (17), 1665-1677.
11. Chen, Y. J.; Yusuf, M. H.; Guan, Y. X.; Jacobson, R. B.; Lagally, M. G.; Babcock, S. E.; Kuech, T. F.; Evans, P. G. Distinct Nucleation and Growth Kinetics of Amorphous $SrTiO_3$ on (001) $SrTiO_3$ and SiO_2/Si: A Step toward New Architectures. *ACS Appl. Mater. Interfaces* **2017,** *9*, 41034-41042.
12. Chen, Y. J.; Tilka, J. A.; Ahn, Y.; Park, J.; Pateras, A.; Zhou, T.; Savage, D. E.; McNulty, I.; Holt, M. V.; Paskiewicz, D. M.*; et al.* Seeded Lateral Solid-Phase Crystallization of the Perovskite Oxide $SrTiO_3$. *J. Phys. Chem. C* **2019,** *123* (12), 7447-7456.
13. Akbashev, A. R.; Plokhikh, A. V.; Barbash, D.; Lofland, S. E.; Spanier, J. E. Crystallization Engineering as a Route to Epitaxial Strain Control. *APL Mater.* **2015,** *3* (10), 106102.
14. Almeida, B. G.; Pietka, A.; Caldelas, P.; Mendes, J. A.; Ribeiro, J. L. Determination of Infrared Optical Parameters of $SrTiO_3$ Thin Films from the Reflectivity Spectrum. *Thin Solid Films* **2006,** *513* (1-2), 275-282.
15. Johnson, R. W.; Hultqvist, A.; Bent, S. F. A Brief Review of Atomic Layer Deposition: from Fundamentals to Applications. *Mater. Today* **2014,** *17* (5), 236-246.
16. George, S. M. Atomic Layer Deposition: An Overview. *Chem. Rev.* **2010,** *110* (1), 111-131.
17. Leskela, M.; Ritala, M. Atomic Layer Deposition Chemistry: Recent Developments and Future Challenges. *Angew. Chem. Int. Ed.* **2003,** *42* (45), 5548-5554.
18. Knez, M.; Niesch, K.; Niinisto, L. Synthesis and Surface Engineering of Complex Nanostructures by Atomic Layer Deposition. *Adv. Mater.* **2007,** *19* (21), 3425-3438.
19. Miikkulainen, V.; Leskela, M.; Ritala, M.; Puurunen, R. L. Crystallinity of Inorganic Films Grown by Atomic Layer Deposition: Overview and General Trends. *J. Appl. Phys.* **2013,** *113* (2).
20. Elliott, S. D.; Nilsen, O. Reaction Mechanisms in ALD of Ternary Oxides. *ECS Trans.* **2011,** *41* (2), 175-183.
21. Nieminen, M.; Sajavaara, T.; Rauhala, E.; Putkonen, M.; Niinisto, L. Surface-Controlled Growth of $LaAlO_3$ Thin Films by Atomic Layer Epitaxy. *J. Mater. Chem.* **2001,** *11* (9), 2340-2345.

22. Wang, H. T.; Wang, J. J.; Gordon, R.; Lehn, J. S. M.; Li, H. Z.; Hong, D.; Shenai, D. V. Atomic Layer Deposition of Lanthanum-Based Ternary Oxides. *Electrochem. Solid-State Lett.* **2009,** *12* (4), G13-G15.
23. Vehkamaki, M.; Hatanpaa, T.; Hanninen, T.; Ritala, M.; Leskela, M. Growth of $SrTiO_3$ and $BaTiO_3$ Thin Films by Atomic Layer Deposition. *Electrochem. Solid-State Lett.* **1999,** *2* (10), 504-506.
24. Lim, B. S.; Rahtu, A.; de Rouffignac, P.; Gordon, R. G. Atomic Layer Deposition of Lanthanum Aluminum Oxide Nano-Laminates for Electrical Applications. *Appl. Phys. Lett.* **2004,** *84* (20), 3957-3959.
25. De Rouffignac, P.; Gordon, R. G. Atomic Layer Deposition of Praseodymium Aluminum Oxide for Electrical Applications. *Chem. Vap. Deposition* **2006,** *12* (2-3), 152-157.
26. Akbashev, A. R.; Chen, G. N.; Spanier, J. E. A Facile Route for Producing Single-Crystalline Epitaxial Perovskite Oxide Thin Films. *Nano Lett.* **2014,** *14* (1), 44-49.
27. Waduge, W.; Chen, Y. J.; Jayakodiarachchi, N.; Kuech, T. F.; Babcock, S. E.; Evans, P. G.; Winter, C. H. Solid Phase Epitaxy of $PrAlO_3$ Films Grown by Atomic Layer Deposition. *Submitted* **2019**.
28. Puurunen, R. L. Surface Chemistry of Atomic Layer Deposition: A Case Study for the Trimethylaluminum/Water Process. *J. Appl. Phys.* **2005,** *97* (12).
29. Blakeney, K. J.; Winter, C. H. Thermal Atomic Layer Deposition of Tungsten Carbide Films from WCl_6 and $AlMe_3$. *J. Vac. Sci. Technol., A* **2018,** *36* (1).
30. Ryndin, Y. A.; Nogin, Y. N.; Paukshtis, E.; Kalinkin, A.; Chuvilin, A.; Zverev, Y. B. Influence of Pr Ions on the Properties of Pd Supported on Ultradispersed Diamond and Graphite from Organometallic Precursors. *J. Mol. Catal.* **1990,** *62* (1), 45-56.
31. Sarma, D.; Rao, C. XPES Studies of Oxides of Second-and Third-Row Transition Metals Including Rare Earths. *J. Electron Spectrosc. Relat. Phenom.* **1980,** *20* (1), 25-45.
32. Kruczek, M.; Talik, E.; Pawlak, D. A.; Kolodziejak, K.; Lukasiewiu, T. XPS Study of $PrAlO_3$-$PrAl_{11}O_{18}$ and $PrAlO_3$-Pr_2O_3 Eutectics. *J. Alloys. Compd.* **2007,** *442* (1-2), 255-258.
33. Avantage Basic and Advanced Processing, Thermo Fisher Scientific. http://www.thermo.com.cn/Resources/201411/2412740468.pdf.
34. Harrison, K.; Hazell, L. B. The Determination of Uncertainties in Quantitative Xps Aes and Its Impact on Data Acquisition Strategy. *Surf. Interface Anal.* **1992,** *18* (5), 368-376.
35. Shirley, D. A. High-Resolution X-Ray Photoemission Spectrum of Valence Bands of Gold. *Phys. Rev. B* **1972,** *5* (12), 4709.
36. Tanuma, S.; Powell, C. J.; Penn, D. R. Calculations of Electron Inelastic Mean Free Paths (IMFPS). IV. Evaluation of Calculated IMFPS and of the Predictive IMFP Formula TPP-2 for Electron Energies between 50 and 2000 eV. *Surf. Interface Anal.* **1993,** *20* (1), 77-89.
37. Ward, R.; Wood, B. A Comparison of Experimental and Theoretically Derived Sensitivity Factors for XPS. *Surf. Interface Anal.* **1992,** *18* (9), 679-684.
38. Benoit, D.; Bresse, J. F.; VantDack, L.; Werner, H.; Wernisch, J. *Microbeam and Nanobeam Analysis*, Springer: Vienna, 1996; Vol. 13.
39. Tang, H.; Herman, I. P. Raman Microprobe Scattering of Solid Silicon and Germanium at the Melting Temperature. *Phys. Rev. B* **1991,** *43* (3), 2299-2304.
40. Yang, K.; Nazir, S.; Behtash, M.; Cheng, J. L. High-Throughput Design of Two-Dimensional Electron Gas Systems Based on Polar/Nonpolar Perovskite Oxide Heterostructures. *Sci. Rep.* **2016,** *6*.

41. Zhou, R.-S.; Snyder, R. L. Structures and Transformation Mechanisms of the η, γ and θ Transition Aluminas. *Acta Crystallogr., Sect. B: Struct. Sci.* **1991,** *47* (5), 617-630.
42. Janotti, A.; Jalan, B.; Stemmer, S.; Van de Walle, C. G. Effects of Doping on the Lattice Parameter of $SrTiO_3$. *Appl. Phys. Lett.* **2012,** *100* (26).
43. Ngo, T. Q.; Goble, N. J.; Posadas, A.; Kormondy, K. J.; Lu, S. R.; McDaniel, M. D.; Jordan-Sweet, J.; Smith, D. J.; Gao, X. P. A.; Demkov, A. A.*; et al.* Quasi-Two-Dimensional Electron Gas at the Interface of Gamma-Al_2O_3/$SrTiO_3$ Heterostructures Grown by Atomic Layer Deposition. *J. Appl. Phys.* **2015,** *118* (11).
44. Kormondy, K. J.; Posadas, A. B.; Ngo, T. Q.; Lu, S. R.; Goble, N.; Jordan-Sweet, J.; Gao, X. P. A.; Smith, D. J.; McCartney, M. R.; Ekerdt, J. G.*; et al.* Quasi-Two-Dimensional Electron Gas at the Epitaxial Alumina/$SrTiO_3$ Interface: Control of Oxygen Vacancies. *J. Appl. Phys.* **2015,** *117* (9).
45. Chen, Y. Z.; Bovet, N.; Kasama, T.; Gao, W. W.; Yazdi, S.; Ma, C.; Pryds, N.; Linderoth, S. Room Temperature Formation of High-Mobility Two-Dimensional Electron Gases at Crystalline Complex Oxide Interfaces. *Adv. Mater.* **2014,** *26* (9), 1462-1467.
46. Chen, Y. Z.; Bovet, N.; Trier, F.; Christensen, D. V.; Qu, F. M.; Andersen, N. H.; Kasama, T.; Zhang, W.; Giraud, R.; Dufouleur, J.*; et al.* A High-Mobility Two-Dimensional Electron Gas at the Spinel/Perovskite Interface of Gamma-Al_2O_3/$SrTiO_3$. *Nat. Commun.* **2013,** *4*.
47. Lu, S. R.; Kormondy, K. J.; Ngo, T. Q.; Aoki, T.; Posadas, A.; Ekerdt, J. G.; Demkov, A. A.; McCartney, M. R.; Smith, D. J. Spectrum and Phase Mapping Across the Epitaxial Gamma-Al_2O_3/$SrTiO_3$ Interface. *Appl. Phys. Lett.* **2016,** *108* (5).
48. Kondo, H.; Matsui, H.; Furuta, K.; Sakashita, M.; Zaima, S. Formation of Pr Oxide Films by Atomic Layer Deposition Using $Pr(EtCp)_3$ Precursor. *Jpn. J. Appl. Phys.* **2010,** *49* (4).
49. Jeon, W. S.; Yang, S.; Lee, C. S.; Kang, S. W. Atomic Layer Deposition of Al_2O_3 Thin Films Using Trimethylaluminum and Isopropyl Alcohol. *J. Electrochem. Soc.* **2002,** *149* (6), C306-C310.

Chapter 5: Low-temperature solid-phase epitaxial growth of $ScAlMgO_4$ thin films on (0001) sapphire

5.1 Introduction

GaN is a wide-bandgap semiconductor which has useful properties relevant to applications in lighting and electronics.[1-2] Epitaxial GaN films have been conventionally grown on c-plane sapphire substrates. The in-plane lattice mismatch between sapphire and GaN is as large as 13%, resulting in the formation of a large number of dislocations per unit area in the thin film.[3] The complex oxide $ScAlMgO_4$ (SCAM) is a particularly promising substrate material for growing high-quality GaN films because SCAM has an excellent in-plane lattice match of 1.4% with GaN.[4] SCAM has a slightly larger in-plane lattice parameter than GaN.[4] This excellent lattice match leads to the potential that GaN thin films can be grown with a far lower density of dislocations than with the current suite of substrates. The reduced defect concentrations can produce improved GaN materials for opto-electronic devices.[4] The growth of GaN on SCAM results in an epitaxial relationship in which the [0001] GaN is parallel to the [0001] SCAM and the $[10\bar{1}0]$ GaN is parallel to the $[11\bar{2}0]$ SCAM.[5]

SCAM single crystals have been grown by the Czochralski method in which crystal is made by pulling from a melt at high temperatures.[4,6] The complex chemical composition of SCAM and its high melting temperature of 2173 K, however, pose challenges to grow high-quality SCAM single crystals using the Czochralski method.[4,6-7] The cost of making single crystals of SCAM is also prohibitively high due to the rarity and expense of elemental Sc. A promising strategy is to grow epitaxial SCAM thin films on sapphire substrates as buffer layers to grow epitaxial GaN thin

films for reduced defect concentrations.

The growth of epitaxial SCAM thin films with vapor-phase epitaxy techniques is also challenging. The vapor-phase deposition of oxides often requires the use of high substrate temperatures because high-quality single-crystalline thin films are often grown at a high temperature very close to ½ of the melting temperature, as proposed by the Ishizaka rule.[8] High deposition temperatures can cause significant difference from the intended chemical compositions when one component of the deposited material is volatile, for example in rare-earth iridates, in mercury-based compounds such as $HgBa_2CaCu_2O_x$ and in complex oxides containing Zn.[9-12] A similar compositional deviation is expected in SCAM because the high vapor pressure of Sc can lead to evaporation during high-temperature deposition processes. A flux-mediated pulsed laser deposition process in which the SCAM components were delivered with a simultaneous supply of BiO_x flux was used to grow SCAM thin films on (0001) sapphire at a relatively low growth temperature of 840 ºC.[13] A thin layer of a competing $MgAl_2O_4$ spinel phase also formed between the SCAM film and sapphire substrate.[13] The preferential growth of the spinel phase at the interface was caused by the reactivity between the Al_2O_3 substrate and the Bi_2O_3 flux to form the Al-rich condition.[13]

This Chapter describes the development of low-temperature solid-phase epitaxy (SPE) technique for the growth of epitaxial SCAM thin films on sapphire substrates. As introduced in Chapter 1, SPE involves the creation of amorphous layers on single-crystal substrates followed by a separate epitaxial crystallization process often driven by heating. Diffusion in the solid state is much slower and relatively low temperatures can be used to crystallize the complex-oxide thin films on crystalline seeds.[14] SPE presents a promising method to grow this multi-component oxide thin film which may have deviation in compositions due to the volatile component when deposited

with vapor-phase epitaxy at high temperatures.

The present investigation of the conditions under which SPE can be used to form SCAM thin films builds on a series of investigations using related techniques in similar multi-component materials. One of these related techniques, reactive solid-phase epitaxy (R-SPE) has been developed for the deposition of complex oxides with layered structures such as $RAO_3(MO)_m$ (R = In and rare-earth elements; A = Ga, In, Al and Fe; M = Mg, Co, Cu and Zn; m = integer) and LaCuOS that cannot be deposited by vapor-phase epitaxy.[11-12,15] The R-SPE method employs a thin sacrificial epitaxial layer at the interface between the deposited oxide thin film and the substrate to react with the amorphous oxide at high heating temperatures.[12] The sacrificial layer in R-SPE serves as an epitaxial template determining the crystallographic orientation of the crystallized oxide film.[11] The ratio of the thickness of the sacrificial layer to the thickness of the amorphous oxide layer determines the resulting film composition.[11]

An epitaxial ZnO layer was used as the sacrificial layer to fabricate single-crystalline SCAM thin films on YSZ (111) substrates by R-SPE.[5,16-17] Epitaxial SCAM thin films were achieved by R-SPE at a high crystallization temperature of 1450 ºC or 1470 ºC, and polycrystalline SCAM films were obtained at a relatively lower temperature such as 1300 ºC.[5,16-17] The impurity phase $MgAl_2O_4$ formed at a crystallization temperature higher than 1200 ºC, probably because of the diffusion of Sc ions into the substrate.[5,16-17] Two strategies were employed to avoid the formation of the impurity phase $MgAl_2O_4$: (i) An extra 20% Sc was added into the target to compensate the loss of Sc due to diffusion;[5,17] (ii) A $ScGaO_3(ZnO)_m$ buffer layer was deposited on the substrate before the deposition of the ZnO and amorphous SCAM layers to suppress the reaction between the SCAM film and the substrate.[16] The strategy involving the use of an added amount of Sc required careful selection of the additional amount of Sc because too much Sc

resulted in extra Sc_2O_3 phase in the deposited and crystallized films.[5,17] The epitaxial SCAM film prepared using the $ScGaO_3(ZnO)_m$ buffer layer had Ga ions in the SCAM because Zn evaporated at high temperatures.[16] Those two strategies added a lot of complexity in the R-SPE process to create epitaxial SCAM thin films without the impurity $MgAl_2O_4$. Extensive experiments are required to figure out the right target compositions without forming an extra phase. Finding an appropriate buffer layer is also challenging because the buffer layer need to suppress the reaction and also totally evaporate at high temperatures so that extra impurities are not added on. Similar strategies thus may not be readily applicable to be combined with the R-SPE process to create other epitaxial complex oxides that also have diffusion of the components into substrates at high temperatures.

The studies discussed above proposed that the reason why the impurity phase $MgAl_2O_4$ formed at a crystallization temperature higher than 1200 ºC was probably because of the diffusion of Sc ions into the YSZ substrate.[5,16-17] Extra strategies were used in those studies to avoid the diffusion of Sc into the substrate and the formation of $MgAl_2O_4$ phase at temperatures higher than 1200 ºC.[5,16-17] No detailed structural analysis, however, have been conducted to observe the diffusion of the Sc into the substrate at high temperatures.

The direct SPE growth of epitaxial SCAM thin films on single-crystal substrates without the use of any sacrificial layer for the solid-state reactions in the R-SPE process has not been explored yet. There is now a particular opportunity to exploit the differences in how the rates of key processes in the epitaxy of SCAM depend on the temperature. This Chapter explores the hypothesis that the solid-state reaction and diffusion processes that have resulted in the degradation of the SCAM films produced at high temperatures will not be observed at lower temperatures. The experimental results reported here show that the epitaxy is possible at a far lower temperature than

has been reported in the R-SPE studies. The results of this Chapter more generally indicate that low crystallization temperatures can be employed to create epitaxial complex-oxide thin films with complicated compositions by SPE.

The study in this Chapter explores the solid-phase crystallization of amorphous SCAM thin films on (0001) sapphire (α-Al_2O_3) substrates without the use of any extra epitaxial template layer for the solid-state reactions. The key result is that epitaxial SCAM thin films can be grown by SPE at the relatively low temperature of 950 ºC. A series of high-temperature control experiments reveal effects that are consistent with previous literature reports. The solid-state reaction of Sc with Al_2O_3 resulted in compositional inhomogeneity of the film and substrate, which prohibits the SPE growth of SCAM at the relatively high temperature of 1400 ºC. The compositional inhomogeneity leads to the formation of epitaxial impurity phase $MgAl_2O_4$ on part of the (0001) sapphire substrate. The different crystallization results at the two temperatures indicate that a relatively low temperature of 950 ºC can be used to grow epitaxial SCAM thin films with SPE.

5.2 Structure of $ScAlMgO_4$

The chemical formula of SCAM can also be written as $ScAlO_3(MgO)$, which makes it clear that SCAM belongs to a broader family of the layered oxides $RAO_3(MO)_m$ that were introduced in Section 5.1 of this Chapter.[17] SCAM has a hexagonal structure with lattice parameters a = b = 3.236 Å and c = 25.150 Å as shown in Figure 5-1.[18-20] The wurtzite (Al, Mg)O_x (0001) layers and rock-salt ScO_y (111) layers alternatively stack along the c axis.[21] The dashed line in Figure 5-1 encloses one repeating unit of the SCAM structure, indicating that one unit of SCAM along the c axis covers three layers of (Al, Mg)O_x and ScO_y.

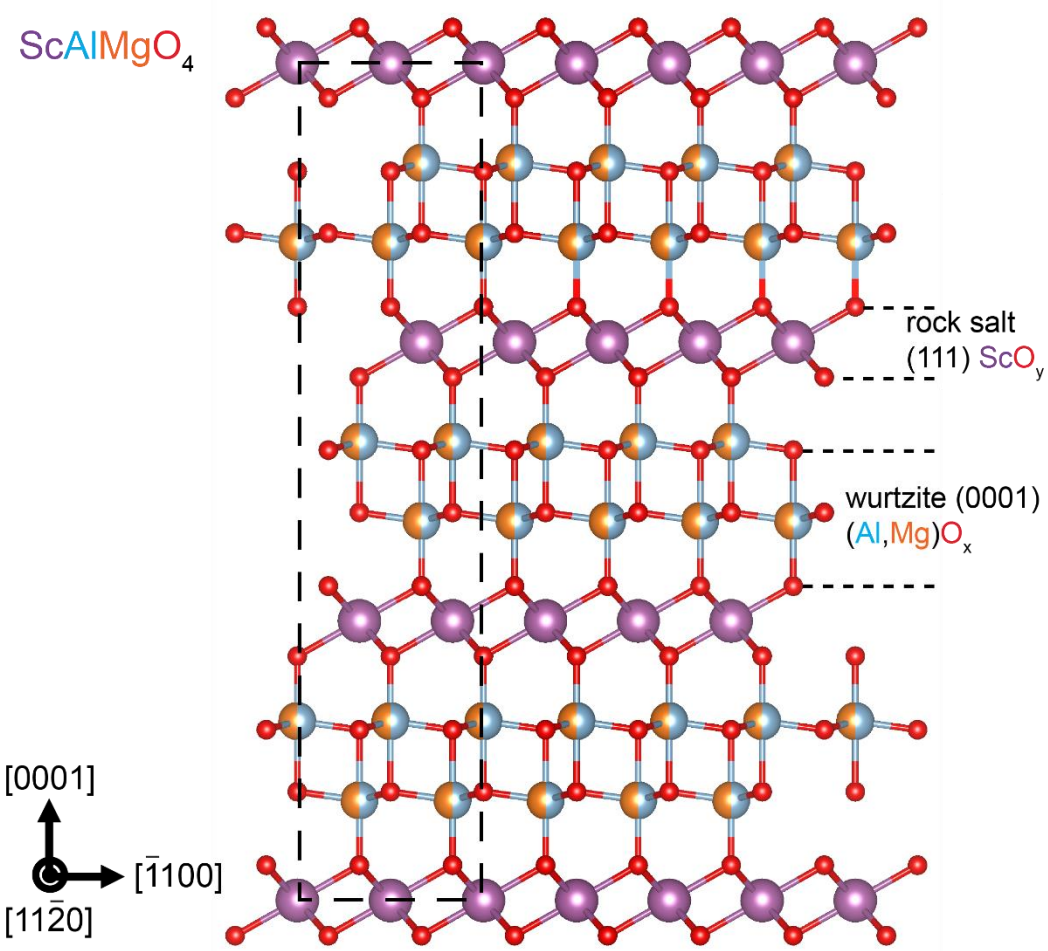

Figure 5-1. Crystal structure of SCAM. The dashed line encloses one repeating unit of the SCAM structure.

5.3 Experimental details

The crystallization of SCAM from initially amorphous layers was investigated by sputter depositing amorphous SCAM thin films on (0001) sapphire substrates, followed with *ex situ* thermal heating. A nominally stoichiometric $ScAlMgO_4$ ceramic target was purchased from AJA International, Inc.. The target was synthesized from a mixture of three oxides, Sc_2O_3, Al_2O_3, and MgO. Further details of the processing of this target are not known.

The composition and phases of a target play a key role in determining the composition of the deposited thin films. Characterization of the nominal SCAM target after purchase indicates that the target is composed of different sizes of $MgAl_2O_4$, MgO and Sc_2O_3 crystals. The surface of the target was characterized using variable pressure scanning electron microscopy (SEM) with energy-dispersive X-ray spectroscopy (EDS). The SEM-EDS measurements were conducted by Dr. J. H. Fournelle in the Department of Geology and Geophysics at University of Wisconsin-Madison. Figure 5-2 shows an SEM image of the target surface. EDS measurements were conducted at a series of positions, marked with the white circles in the SEM image shown in Figure 5-2, in order to determine which phases are present in the SCAM target. The EDS measurements indicate that the relatively brighter parts of the SEM image in Figure 5-2 (appearing white in the image) are the Sc_2O_3 phase. The less bright parts of the SEM image (appearing black in the image) are composed of $MgAl_2O_4$ or MgO phases. Other parts of the target surface show similar features.

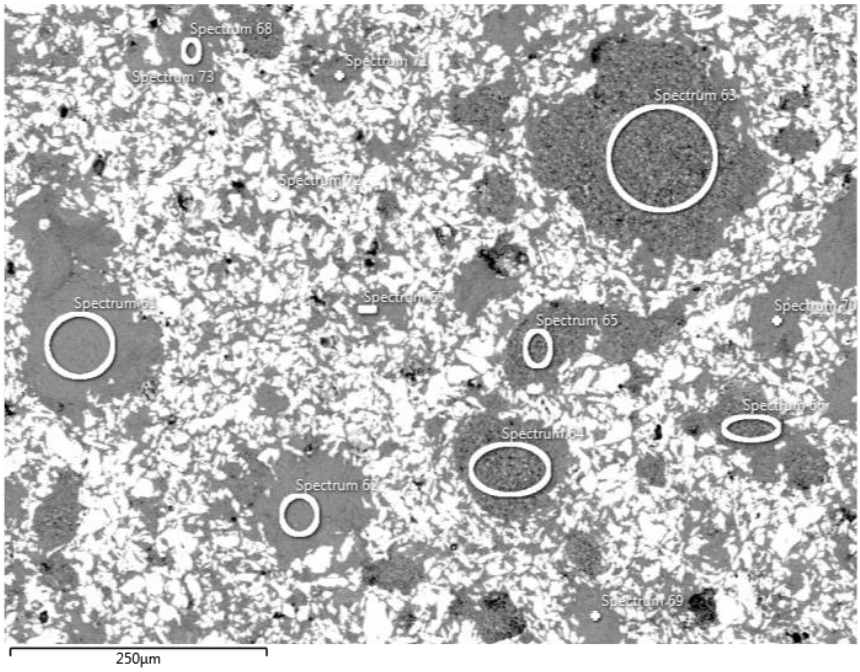

Figure 5-2: SEM image of a part of the target surface. The white circles are marking the positions where the EDS measurements were conducted.

The three distinct phases in the target were also identified by a powder X-ray diffraction measurement of the target surface. Figure 5-3 shows the powder X-ray diffraction pattern of the target. The crystalline peaks can be indexed as arising from the crystalline phases $MgAl_2O_4$, MgO and Sc_2O_3. The absence of the stoichiometric SCAM phase and the random mixture of the three phases in the target pose the challenge to deposit stoichiometric amorphous SCAM thin films.

The reason why SCAM phase did not form in the target employed in this study is not clear without knowing the detailed procedures for the synthesis of the target. A previous published study, however, shows that a target most of which is composed of the SCAM phase can be synthesized from a stoichiometric mixture of Sc_2O_3, Al_2O_3 and MgO and reaction of the three phases at a high temperature, although the target also contains a small amount of the impurity phases $MgAl_2O_4$ and Sc_2O_3.[5] The different crystalline phases of the target observed here might be caused by the different processing method and conditions under which the reaction to form SCAM phase did not occur. The preparation of oxide targets with complex compositions and volatile components is not easy and may require complicated procedures. For example, a pyrochlore $Nd_2Ir_2O_7$ sputtering target with the right stoichiometric atomic ratios was synthesized with a series of procedures because the component iridium is volatile.[22] Preparing a stoichiometric SCAM target without extra impurity phases can be challenging, but will be helpful for the deposition of an amorphous film with the stoichiometric composition.

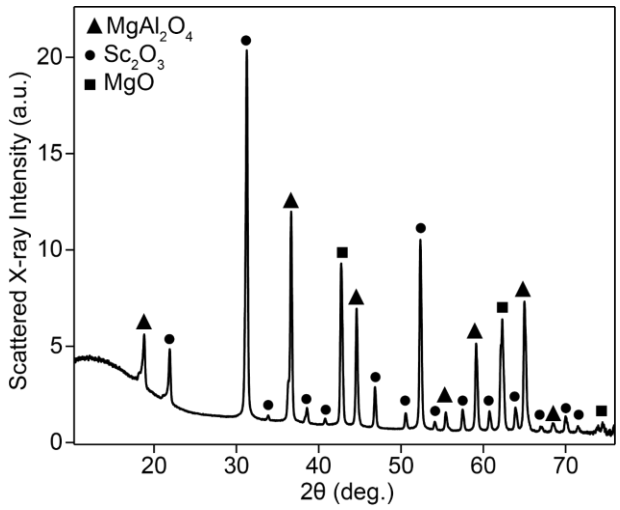

Figure 5-3: Powder X-ray diffraction pattern of the nominal SCAM target. The target contains three crystalline phases $MgAl_2O_4$, Sc_2O_3 and MgO.

With this target that has three crystalline phases, amorphous SCAM thin films were deposited by on-axis radio-frequency magnetron sputtering onto (0001) sapphire substrates held at room temperature. Prior to depositing the amorphous films, the sputter-deposition vacuum chamber was evacuated to 2×10^{-6} Torr. SCAM layers were grown with a total pressure of 18 mTorr with only Ar gas flow. The deposition conditions of SCAM layers are different from that used for STO described in Chapter 2. The amorphous film was deposited at a rate of 15 nm h^{-1} to a total thickness of approximately 60 nm.

Microstructures of the crystallized samples were studied by transmission electron microscopy (TEM) and scanning transmission electron microscopy (STEM). The TEM measurement in Figure 5-5 was conducted by Dr. Yingxin Guan, and the TEM and STEM measurements in Figure 5-7 and Figure 5-10 were conducted by Dr. Peng Zuo at UW-Madison through a collaboration supported by University of Wisconsin Materials Research Science and Engineering Center. The cross-sectional TEM and STEM specimens were prepared using focused ion beam (FIB) techniques with a Ga ion source (Auriga, Zeiss, Inc.). STEM high-angle annular

dark-field (HAADF) images were collected using a FEI Titian 80-200 aberration-corrected scanning transmission electron microscope with an acceleration voltage of 200 kV. Selected area electron diffraction (SAED) and TEM dark-field (DF) and bright-field (BF) images were acquired using a FEI Tecnai TF30 transmission electron microscope with an acceleration voltage of 300 kV.

5.4 Characterization of the as-deposited SCAM films

An as-deposited SCAM film on a (0001) sapphire substrate was characterized by grazing-incidence X-ray scattering employing the method described in Section 1.4 of Chapter 1. Figure 5-4(a) shows grazing-incidence X-ray scattering patterns acquired from a bare sapphire substrate and the as-deposited SCAM thin film. The bare sapphire substrate exhibits a featureless low-intensity background. The X-ray scattering pattern of the as-deposited film includes a broad intensity maximum centered at $2\theta = 32^{o}$ and another broad peak at $2\theta = 42^{o}$. The broad peaks of the as-deposited film indicate that the as-deposited film is amorphous.

The thickness of the as-deposited amorphous SCAM film was determined by an X-ray reflectivity (XRR) measurement. XRR data was collected using the method introduced in Section 2.3 of Chapter 2. Figure 5-4(b) shows the XRR data of an as-deposited SCAM film on a (0001) sapphire substrate. The film thickness was determined to be 59 nm based on the mean period of the oscillation of the reflected intensity.

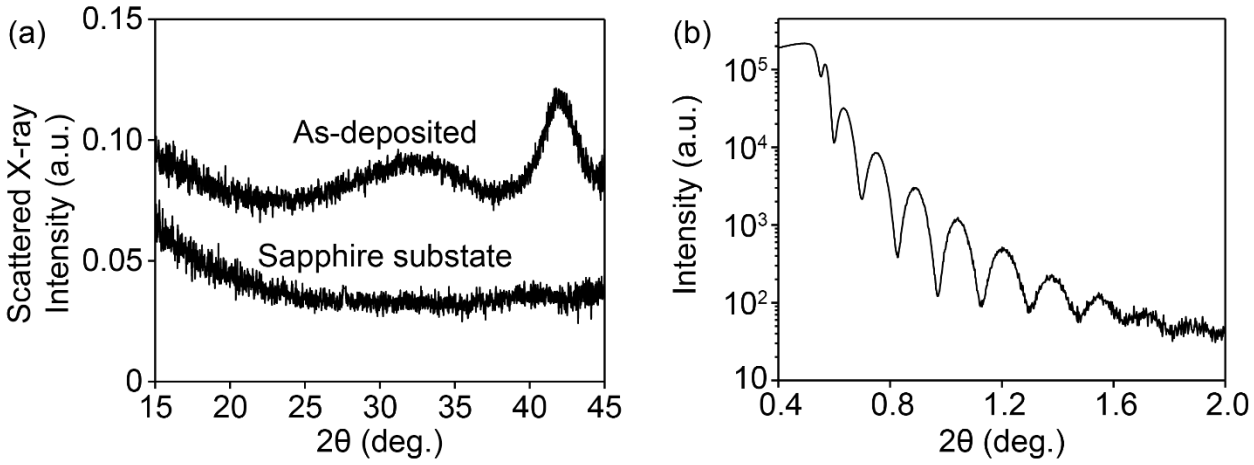

Figure 5-4. (a) Grazing-incidence X-ray scattering intensity for an as-deposited SCAM film and a bare sapphire substrate. (b) XRR measurement of an as-deposited SCAM film on a sapphire substrate.

The Mg:Sc atomic ratios in the as-deposited films were analyzed using EPMA-WDS as introduced in Section 4.3.1 of Chapter 4. In this case, synthetic $ScPO_4$ and MgO were used as the reference standards for the measurements of the amount of Sc and Mg elements in the films, respectively. The EPMA-WDS measurements were conducted by Dr. J. H. Fournelle at UW-Madison. Both an as-deposited amorphous film on a SiO_2/Si substrate and an as-deposited amorphous film on a sapphire substrate have a Mg:Sc atomic ratio of 1:0.85, indicating that the as-deposited films are Sc deficient.

5.5 Crystallization of the amorphous SCAM films

With the Sc-deficient SCAM layers deposited on sapphire substrates by sputter deposition, a series of different temperatures and durations were employed for the crystallization experiments. The as-deposited films were heated by inserting the samples into a preheated furnace in still air. After being heated in the furnace for durations ranging from 30 min to 48 h, the samples were removed from the furnace and cooled down with a dry N_2 gas flow.

The as-deposited film remained amorphous when the film was heated at a temperature below 900 ºC for a relatively long duration. An amorphous film can be fully crystallized after heating at 900 ºC for 48 h. The crystallization of two amorphous films at a relatively low temperature of 950 ºC and at a relatively high temperature of 1400 ºC is discussed below.

5.5.1 Crystallization at 950 ºC

950 ºC is the lowest temperature investigated in this study at which an amorphous film can be fully crystallized within a relatively short time of 10 h. Figure 5-5(a) shows grazing-incidence X-ray scattering patterns of a film on the sapphire substrate after heating at 950 ºC for 5 h and 10 h. Scattering intensity from the bare sapphire substrate and the as-deposited amorphous film is shown for comparison. The amorphous SCAM film heated at 950 ºC for 5 h is partially crystallized because there remains a broad intensity maximum centered at $2\theta = 35^{o}$ that comes from the amorphous film.

TEM provides further evidence that the film heated at 950 ºC for 5 h is partially crystallized. Figure 5-5(b) shows a cross-sectional high-resolution TEM image of the film crystallized at 950 ºC for 5 h. A thick Au layer was deposited on the sample surface for the measurement. The crystallized SCAM film is 50-nm thick. The bottom substrate is <0001>-oriented α-Al_2O_3. One 50-nm thick crystalline domain was observed in this regime. The spacing of the fringes is 0.84 nm, which matches the spacing of SCAM 0003 planes. The matched spacing indicates that this crystalline domain is SCAM crystal. The SCAM crystal does not share the same <0001> orientation as the sapphire substrate. The local orientation of the SCAM crystal has a misorientation of 30^{o} with respect to the α-Al_2O_3 substrate. The parts of the film to left and right of the SCAM crystal in Fig. 5-5(b) are still amorphous.

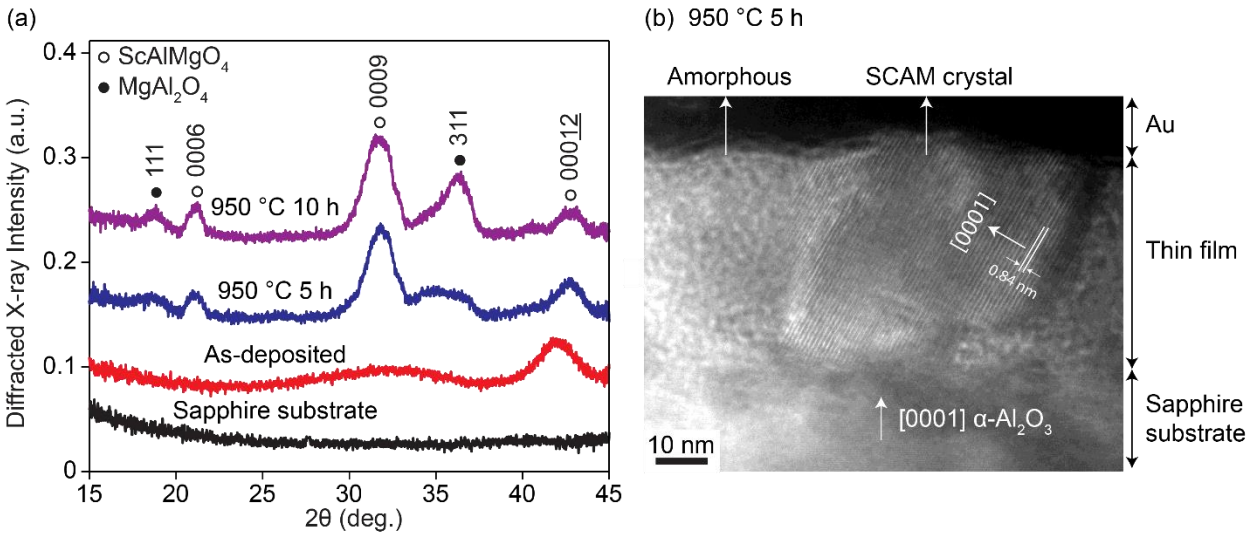

Figure 5-5. (a) Grazing-incidence X-ray scattering intensity for a SCAM film deposited on the sapphire substrate and crystallized at 950 ºC for 5 h and 10h. The curves represent partially crystallized (blue) and fully crystallized (purple) layers. Scattering intensity from the bare sapphire substrate (black) and the as-deposited amorphous film (red)is shown for comparison. (b) High-resolution TEM micrograph of a partially crystallized SCAM film on a sapphire substrate after crystallization at 950 ºC for 5 h.

The X-ray diffraction patterns indicate that the film heated at 950 ºC for 10 h is fully crystallized because the broad X-ray intensity maxima that originate from the as-deposited amorphous film are not present after heating under this condition, shown in Figure 5-5(a). The crystalline phases in the film crystallized at 950 ºC for 10 h and the epitaxial relationship between the film and the (0001) α-Al_2O_3 substrate were examined by a θ-2θ scan using the method described in Section 1.6 of Chapter 1. The scan direction is [0001] direction of the α-Al_2O_3 substrate, which is also the sample normal direction. Figure 5-6(a) shows the measured θ-2θ scan. The peak marked with a star in Figure 5-6(a) is the diffraction from α-Al_2O_3 0006 reflection. The SCAM 000L and α-Al_2O_3 000L reflections appear on the same rod of reciprocal space, indicating that the crystallized film is highly oriented with the same orientation as the substrate. Besides SCAM 000L reflections, $MgAl_2O_4$ 111 and 311 reflections are also observed in the crystallized film.

The mosaic width of the epitaxial SCAM crystals was examined with an X-ray rocking curve scan. Figure 5-6(b) shows X-ray rocking curve scan of SCAM 0009 reflection of the film crystallized at 950 ºC for 10 h. The FWHM of the rocking curve of SCAM 0009 reflection is 0.9º.

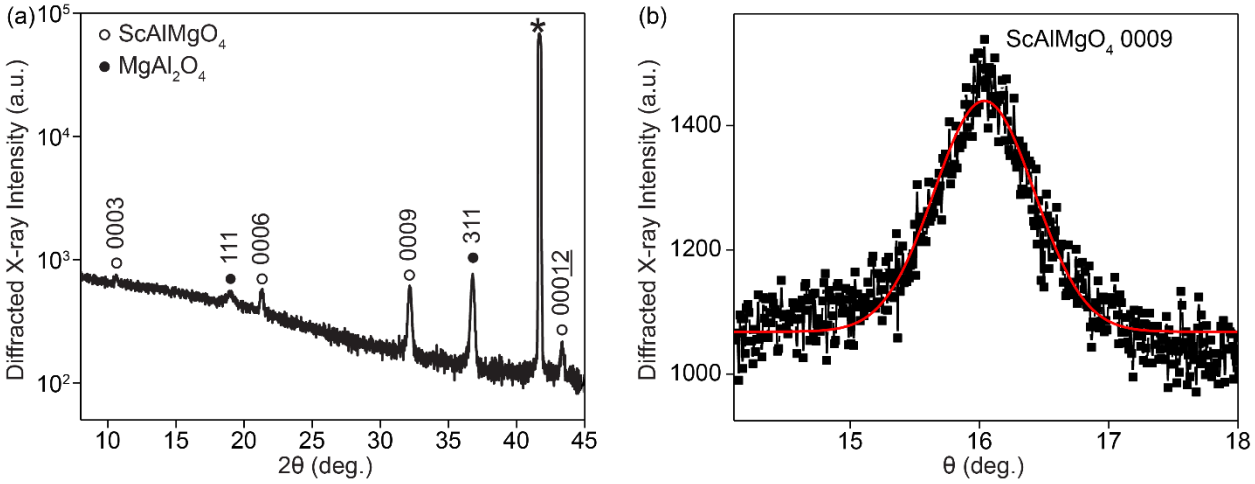

Figure 5-6. (a) X-ray diffraction pattern of the film deposited on (0001) α-Al_2O_3 and crystallized at 950 ºC for 10 h. (b) Rocking curve scan of SCAM 0009 reflection with the Gaussian fit used to find the angular width.

The microstructure of the SCAM layer crystallized at 950 °C for 10 h was studied by TEM DF and BF imaging under two-beam conditions. The sapphire 0003 diffraction spot was selected for the DF imaging in order to probe the expected epitaxial relationship between the SCAM layer and the sapphire substrate along the sample normal direction. Figures 5-7(a) and (b) show the TEM DF and BF images of the cross-sectional specimen with a large field of view including the capping layer deposited for the measurement, the SCAM layer and the α-Al_2O_3 substrate. The sample length investigated in this regime is 75 nm. The brighter areas of the film in the DF image shown in Figure 5-7(a) arise from the diffraction of the SCAM 0006 reflection. The brighter areas are thus where epitaxial SCAM crystals form. SCAM crystals that are not grown epitaxially or reflections from other phases are darker in the DF image. The two SCAM crystals were also observed as the relatively darker parts in the BF image shown in Figure 5-7(b).

The epitaxial relationship between the SCAM crystal and the α-Al_2O_3 substrate can be further examined by a BF image with a higher magnification. Figure 5-7(c) shows a BF image of the SCAM crystal indicated by the red box in Figure 5-7(b) with a higher magnification than in Figure 5-7(b). The spacing of the fringes is 0.83 nm, which matches the spacing of SCAM 0003 planes. The matched spacing indicates that epitaxial SCAM crystal forms on the α-Al_2O_3 substrate. The epitaxial SCAM crystal can grow as large as 110 nm along the in-plane direction and 47 nm along the out-of-plane direction from the interface to the sample surface.

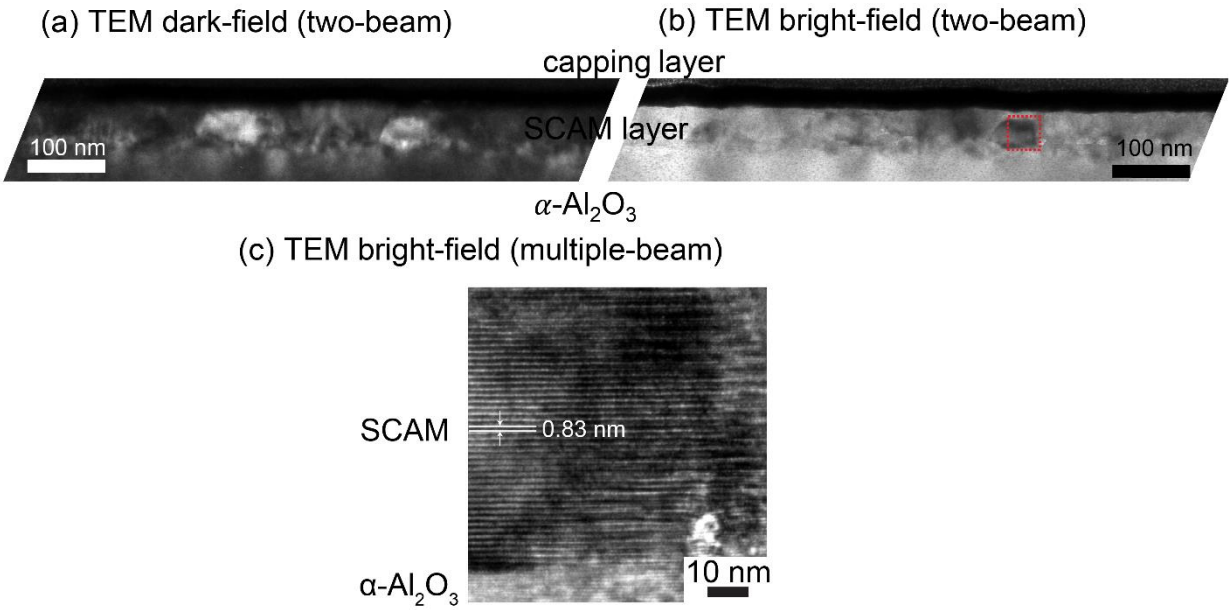

Figure 5-7. (a) TEM dark-field and (b) bright-field images taken under two beam conditions on the sample crystallized at 950 ℃ for 10h; (c) High resolution TEM BF image of the part selected by the red box in (b).

A non-epitaxial SCAM crystal was observed for the partially crystallized film after heating at 950 ºC for 5 h shown in Figure 5-5(b). Epitaxial SCAM crystals were observed for the fully crystallized film after heating at 950 ºC for 10 h shown in Figure 5-7. Because TEM measures the local structures of a small part of the sample, both epitaxial and non-epitaxial SCAM crystals form after crystallization of an amorphous SCAM film on (0001) α-Al_2O_3 at 950 ºC. The SCAM crystals

are 50-nm thick spreading from the interface to sample surface. The formation of $MgAl_2O_4$ crystalline phase was also observed, because the as-deposited amorphous film is Sc-deficient with a Mg:Sc atomic ratio of 1:0.85. The Mg:Sc atomic ratios of the film partially crystallized at 950 ºC for 5 h and of the film fully crystallized at 950 ºC for 10 h were also measured with EPMA-WDS. Both films still had a Mg:Sc atomic ratio of 1:0.85, indicating that the overall film composition did not change after crystallization at 950 ºC.

5.5.2 Crystallization at 1400 ºC

The crystallization behavior of an amorphous SCAM film heated at the higher temperature of 1400 ºC was examined. The amorphous SCAM film was deposited under the same conditions as described in Section 5.3 of this Chapter and was thus expected to also have a Mg:Sc atomic ratio of 1:0.85. The film crystallized at 1400°C for 30 min had very different crystalline structures than the film crystallized at 950 °C for 10 h.

The crystallization time to fully crystallize an amorphous film on (0001) α-Al_2O_3 at 1400 ºC was known by measuring the scattering from the amorphous film using grazing-incidence X-ray scattering. The measurement was conducted using the same geometry as described in Section 1.4 of Chapter 1. Figure 5-8 shows the grazing-incidence X-ray scattering pattern of a SCAM film after crystallization at 1400 ºC for a relatively short duration of 30 min. The grazing-incidence X-ray scattering pattern of the as-deposited amorphous film is shown for comparison. The broad X-ray intensity maxima that originate from the amorphous film disappeared and only crystalline peaks were apparent. An initially amorphous SCAM film thus can be fully crystallized after crystallization at 1400 ºC for 30 min.

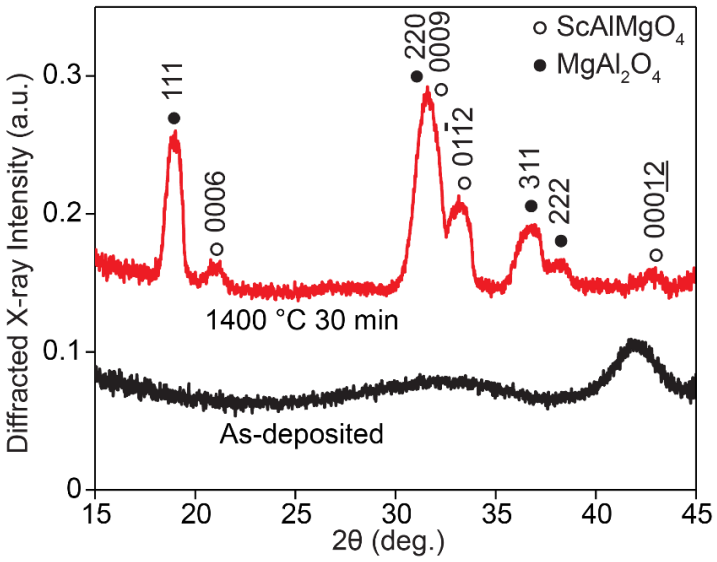

Figure 5-8. Grazing-incidence X-ray scattering of an as-deposited amorphous film and a film crystallized at 1400 ºC for 30 min.

The crystalline phase in the film crystallized at 1400 ºC for 30 min and the epitaxial relationship between the film and the (0001) α-Al_2O_3 substrate were determined using a θ-2θ scan, shown in Figure 5-9(a). The measurement details were introduced in Section 1.6 of Chapter 1. The peak marked with a star is the diffraction from 0006 reflection of the α-Al_2O_3 substrate. The $MgAl_2O_4$ 111, SCAM 000L and α-Al_2O_3 000L reflections appear on the same rod of reciprocal space. (111)-oriented $MgAl_2O_4$ and (000L)-oriented SCAM crystals form after crystallization and align with the 000L orientations of the substrate. Based on the integrated peak intensities of SCAM and $MgAl_2O_4$ phases, more (111)-oriented $MgAl_2O_4$ crystals and less (000L)-oriented SCAM crystals form of the film crystallized at 1400 ºC compared to the film crystallized at 950 ºC for 10 h.

The angular widths of the X-ray rocking curves provide insight into the defect densities of the $MgAl_2O_4$ and SCAM crystals. Figure 5-9(b) shows rocking curve scans of $MgAl_2O_4$ 111 and SCAM 0009 reflections, which give FWHM values of 0.8º and 1.0º, respectively.

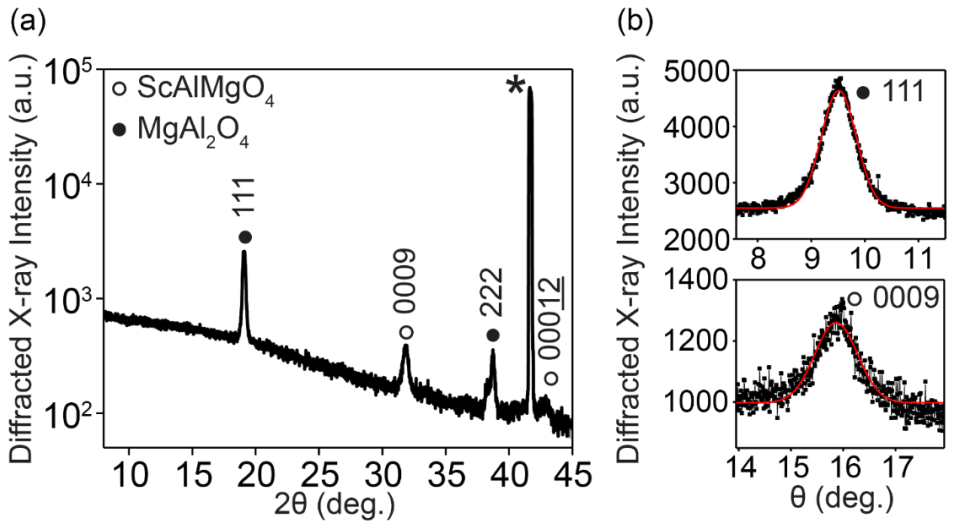

Figure 5-9. (a) X-ray diffraction pattern of the film deposited on (0001) α-Al_2O_3 and crystallized at 1400 ºC for 30 min. (b) Rocking curve scans of $MgAl_2O_4$ 111 and SCAM 0009 reflections with Gaussian fits used to find the angular widths of each reflection.

The microstructure of the film crystallized at 1400 ºC for 30 min was examined by STEM. Figure 5-10(a) shows a STEM-HAADF image of the cross-sectional specimen with a 2.3-μm length with a large field of view including the crystallized SCAM layer and the α-Al_2O_3 substrate. The deposited capping layer for the measurement is not visible with this image contrast. Figure 5-10(b) shows a higher magnification of the sample indicated by the green box in Figure 5-10(a). The red line in Figure 5-10(b) shows the interface between the crystallized film and the α-Al_2O_3 substrate.

Crystallization at 1400 ºC leads to the development of a rough sample surface. The dark and bright parts shown in Figure 5-10(a) and (b) represent the different compositions at different locations. Because the contrast of the STEM-HAADF imaging is approximately proportional to the square of the atomic number, heavier elements such as Sc are in the bright parts. The bright and dark parts of the film above the interface exhibit different phases. EDS analysis at different positions of the film above the interface further indicate that the bright parts are composed of Sc,

Al and O elements and the dark parts are composed of Mg, Al and O elements. EDS analysis at bright parts of the substrate below the interface show the existence of Sc, Al and O elements.

The compositional inhomogeneity observed in the film and substrate for the sample crystallized at 1400 ºC might be caused by solid-state reactions through which the crystalline phases that are composed of Sc, Al and O formed. The crystalline phases that are composed of Sc, Al and O have not been identified yet. The locations where the solid-state reactions occurred are the bright parts of the sample in the STEM-HAADF image. The reactions at those locations led to the long-range transport of Sc within the film from the dark parts of the film along the direction parallel to the interface. Sc had to transport for 0.5 μm within the film so that the solid-state reactions in the film and substrate occurred in the local region of the sample measured in Figure 5-10(b).

The phase of the film with lower intensity in the STEM-HAADF image in contact with the α-Al_2O_3 substrate and the phase above this part of the film are identified by a STEM-BF image with a higher magnification, shown in Figure 5-10(c). The bottom part of Figure 5-10(c) is the film with lower intensity in contact with the substrate in Figure 5-10(b), which is epitaxial $MgAl_2O_4$ crystal because the spacing of the lattice fringes of this part of the film matches with the spacing of $MgAl_2O_4$ 111, and EDS analysis of this part of the film indicates the existence of Mg, Al and O elements. The top part of Figure 5-10(c) is the film grown above the $MgAl_2O_4$ crystal, which is epitaxial SCAM crystal because the spacing of the stripes matches with the spacing of SCAM 0003 planes. The film with lower intensity in the STEM-HAADF image in contact with the α-Al_2O_3 substrate is thus (111)-oriented $MgAl_2O_4$ crystal, and (0001)-oriented SCAM crystal form on top of the $MgAl_2O_4$ crystal close to the sample surface.

The film crystallized at 1400 ºC for 30 min has a Mg:Sc atomic ratio of 1:0.76 based on

the EPMA-WDS measurement of the general composition of this sample. Compared to the as-deposited film with a composition of 1:0.85, the decrease of the amount of Sc in the film after crystallization at 1400 ºC for 30 min can be caused by the solid-state reactions of Sc with the substrate or evaporation of Sc, which will be discussed below in Section 5.6.

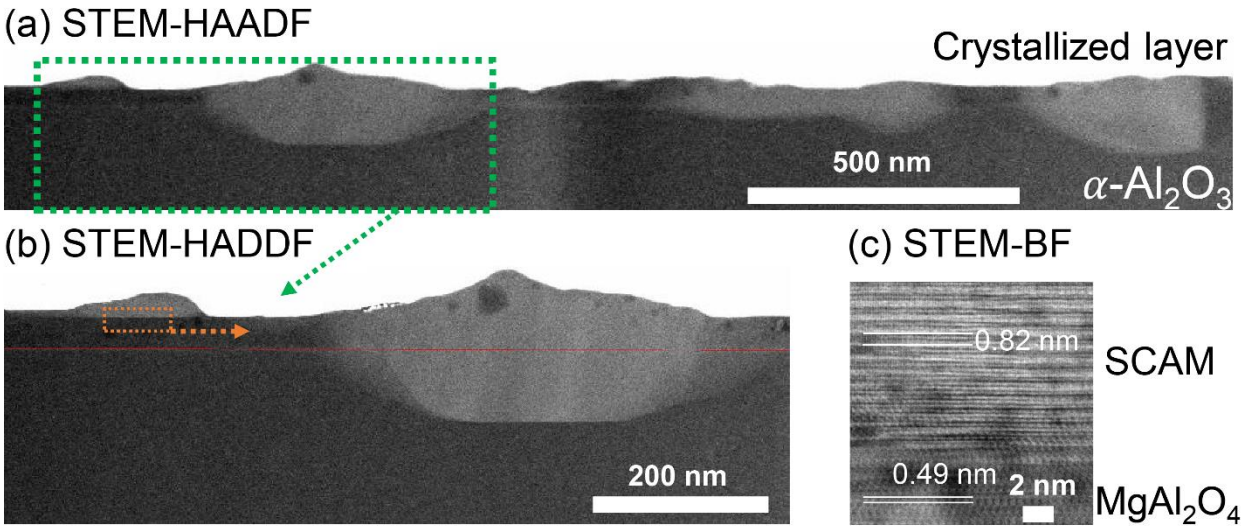

Figure 5-10. (a) STEM-HAADF image on the sample crystallized at 1400 ℃ for 30 min; (b) A higher magnification of the area indicated by the green box in (a); (c) An even higher magnification of the area indicated by the orange box in (b). The red line in (b) represents the interface between the film and the substrate.

The surface roughness and grain sizes of the films crystallized at different temperatures are also different. Figure 5-11(a) shows an atomic force microscopy (AFM) topography image of a partially crystallized film after heating at 950 ºC for 5 h. Figure 5-10(b) shows an AFM image of a fully crystallized film after heating at 1450 ºC for 1 h. The roughness of the partially crystallized film in Figure 5-10(a) is 2 nm and the roughness of the fully crystallized film in Figure 5-10(b) is 1.2 nm. The film crystallized at a higher temperature of 1450 ºC apparently has a larger average grain size than the film crystallized at 950 ºC.

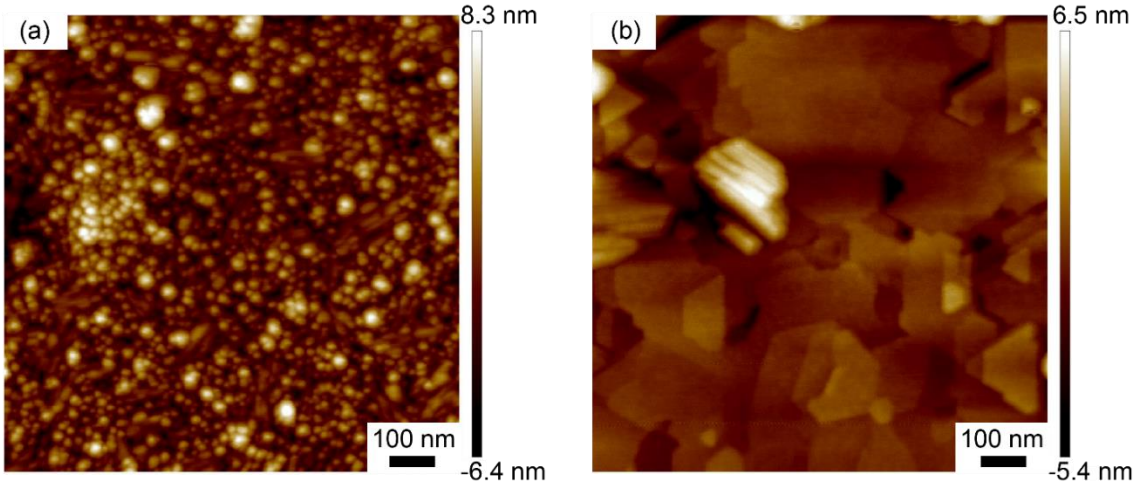

Figure 5-11. AFM images of (a) a partially crystallized film after heating at 950 ºC for 5 h (b) a fully crystallized film after heating at 1450 ºC for 1 h.

5.6 Discussion

Crystallization of amorphous SCAM thin films at two different temperatures results in different crystalline structures. Both epitaxial and non-epitaxial 0001 SCAM crystals throughout the film thickness grow on the 0001 α-Al_2O_3 substrate at 950 ºC. Because of the non-stoichiometric Sc-deficient composition of the as-deposited amorphous film, impurity phase $MgAl_2O_4$ also forms accompanying the formation of the SCAM crystals. The amorphous SCAM film deposited under the same conditions shows different crystallization behavior at 1400 ºC. Epitaxial 111 $MgAl_2O_4$ crystals form on part of the 0001 α-Al_2O_3 substrate. 0001 oriented SCAM crystals only grow on part of the 111 $MgAl_2O_4$ crystals close to the sample surface with non-uniform thicknesses. Large SCAM crystals cannot grow directly on the α-Al_2O_3 substrates at 1400 ºC because of the solid-state reactions at this high temperature. Evaporation of Sc is also possible at 1400 ºC.

5.6.1 Solid-state reaction at 1400 ºC

Because of the observed compositional inhomogeneity of the film and the α-Al_2O_3

substrate for the sample heated at 1400 ºC, solid-state reaction might occur at 1400 ºC in the film and the substrate. The solid-state reaction in the film resulted in the formation of different crystalline phases at different locations of the film including $MgAl_2O_4$ phase and another crystalline phase that is composed of Sc-Al-O. The solid-state reaction in the substrate close to the interface led to the formation of the crystalline phase that is composed of Sc-Al-O. The crystalline phases that are composed of Sc-Al-O in the film and substrate have not been identified yet.

The solid-state reactions that occurred in the film and substrate led to the long-range transport of Sc within the film. The long-range transport of Sc can be considered as the diffusion of Sc at high temperatures. The diffusivity of Sc depends on temperatures. The higher temperature promotes the diffusion of Sc.[23-24] The diffusion coefficient of Sc in single crystal MgO was 25.2 $\mu m^2/h$ at a temperature of 1500 ºC.[23] With this diffusion coefficient, the diffusion length of Sc in a SCAM film is estimated to be 3.5 μm when the film is crystallized at 1400 ºC for 0.5 h. The estimated 3.5 μm is a rough value to be referred to because of the lower temperature and different materials that Sc diffused through in this study. The estimation shows Sc can diffuse on the order of a few microns when the film is crystallized at 1400 ºC for 0.5 h. This estimation agrees with the observation that Sc diffused at least 0.5 μm within the film in order to facilitate the solid-state reaction in local regions of the sample where Sc existed shown in Figure 5-10.

5.6.2 Evaporation of Sc at 1400 ºC

The evaporation of Sc at the high temperature of 1400 ºC might be another reason why the amount of Sc element in the crystallized film decreases, and the decreases of the amount of Sc leads to the formation of epitaxial $MgAl_2O_4$ crystals on the 0001 α-Al_2O_3 substrates.

The vapor pressures of different oxide phases formed by the components were calculated

to evaluate the possible evaporation of components using a thermodynamic calculation software package (HSC Chemistry Version 9.9).[25] The condition was set to be in one air atmosphere and at temperatures varying from 800 to 1500 ºC. Vapor pressures of the possible Sc and Sc-O gas phases were calculated when they were in equilibrium with the solid Sc_2O_3 phase. ScO_2 phase shows the highest vapor pressure among the gas phases at all investigated temperatures. Similarly, vapor pressures of the possible Mg and Mg-O gas phases were calculated when they were in equilibrium with the solid MgO phase under the same environmental condition. MgO phase has the highest vapor pressure at all temperatures. AlO_2 phase is the one that has the highest vapor pressure among the possible Al and Al-O phases when different gas phases are in equilibrium with the solid Al_2O_3 phase under the same condition. Figure 5-12 plots the calculated vapor pressures of ScO_2, MgO and AlO_2 phases when they are in equilibrium with the solid phase Sc_2O_3, MgO and Al_2O_3, respectively in one air atmosphere at temperatures ranging from 800 to 1500 ºC. ScO_2 apparently shows higher vapor pressure than MgO and AlO_2 at all investigated temperatures.

Based on the kinetic theory of gases, molecules are estimated to evaporate with a rate of 1 monolayer of molecules per second at room temperature and at a pressure of 10^{-6} Torr.[26] The calculated vapor pressure of ScO_2 is about 10^{-12} Torr at 950 ºC and 10^{-6} Torr at 1400 ºC. A reasonable estimation is that less than a monolayer of ScO_2 evaporated at 950 ºC for 10 h and 1800 layers of ScO_2 evaporated at 1400 ºC for 30 mins. Evaporation of Mg at 1400 ºC is also possible. The vapor pressure of MgO phase is 10^{-8} Torr at 1400 ºC in one air atmosphere. 18 layers of MgO may evaporate when the film was crystallized at 1400 ºC for 30 min.

The evaporation of Sc at 1400 ºC thus possibly makes the film more Sc-deficient than the as-deposited amorphous film. The composition of the amorphous SCAM film can be maintained when the film is crystallized at 950 ºC. Consistent with the composition study of the as-deposited

and crystallized thin films, both the as-deposited amorphous film and the film crystallized at 950 ºC have a Mg:Sc atomic ratio of 1:0.85. The film crystallized at 1400 ºC, however, has a Mg:Sc atomic ratio of 1:0.76. The crystallization of amorphous SCAM films thus needs to be conducted under the crystallization conditions when the long-range transport and evaporation of the components are not severe to prohibit the epitaxial growth of crystals. Relatively low crystallization temperatures can be employed for the epitaxial growth of crystals through crystallization from the amorphous form.

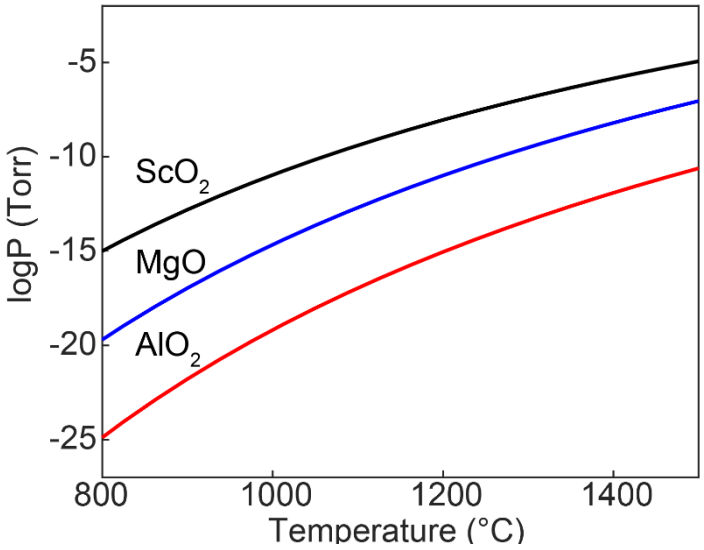

Figure 5-12. Calculated vapor pressures of ScO_2, MgO and AlO_2 gas phases when they are in equilibrium with the Sc_2O_3, MgO and Al_2O_3 solid phases, respectively as a function of temperature under one atmosphere condition.

5.7 Conclusions

The crystallization of an amorphous SCAM film on (0001) α-Al_2O_3 at a relatively low temperature of 950 ºC results in (0001)-oriented SCAM crystals spanning from the interface to sample surface. Crystallization of an amorphous SCAM film at a higher temperature of 1400 ºC is totally different. A variety of complex processes including solid-state reaction of Sc with the film

and Al_2O_3 substrate, evaporation of Sc and Mg, occurred at 1400 ºC. The different kinetic processes at 1400 ºC prohibit the direct SPE growth of SCAM crystals on (0001) α-Al_2O_3 substrates. Instead the competing phase $MgAl_2O_4$ crystals form on part of the substrate. Because of the good lattice match between SCAM and $MgAl_2O_4$, some SCAM crystals still form on part of the $MgAl_2O_4$ crystals.

The R-SPE method that was used for the growth of epitaxial SCAM thin films in the literature requires extra epitaxial template layers for the solid-state reactions, the high crystallization temperatures to facilitate the reactions, and extra strategies to prohibit the diffusion of Sc to reach the substrate and react with the substrate.[5,16-17] The study of the crystallization of an amorphous SCAM layer at 1400 ºC in this work provides direct evidence and structural analysis demonstrating that the solid-state reaction of Sc with the film and substrate causes the compositional inhomogeneity of the film and substrate. SPE growth of SCAM crystals without solid-state reactions at low temperatures is, however, possible because the complex processes are avoided including the diffusion, reaction and evaporation processes that would occur at high temperatures.

Pure epitaxial SCAM thin films at low temperatures are not achieved here because of the deposition of non-stoichiometric Sc-deficient amorphous films. Optimization of the composition of the as-deposited amorphous films is one strategy to form pure SCAM thin films.

Relatively low crystallization temperatures can be used for the SPE growth of complex oxides that have volatile components. The solid-state reactions at high temperatures are not necessary for achieving SPE growth of oxide thin films with complex compositions if careful control of the composition of the as-deposited amorphous films and selection of appropriate temperatures can be achieved.

5.8 References

1. Nakamura, S. The Roles of Structural Imperfections in InGaN-Based Blue Light-Emitting Diodes and Laser Diodes. *Science* **1998,** *281* (5379), 956-961.
2. Davis, R. F. III-V Nitrides for Electronic and Optoelectronic Applications. *Proc. IEEE* **1991,** *79* (5), 702-712.
3. Lester, S. D.; Ponce, F. A.; Craford, M. G.; Steigerwald, D. A. High Dislocation Densities in High-Efficiency Gan-Based Light-Emitting-Diodes. *Appl. Phys. Lett.* **1995,** *66* (10), 1249-1251.
4. Hellman, E. S.; Brandle, C. D.; Schneemeyer, L. F.; Wiesmann, D.; Brener, I.; Siegrist, T.; Berkstresser, G. W.; Buchanan, D. N. E.; Hartford, E. H. $ScAlMgO_4$: An Oxide Substrate for GaN Epitaxy. *MRS Internet J. Nitride Semicond. Res.* **1996,** *1* (1-46), U3-U13.
5. Katase, T.; Nomura, K.; Ohta, H.; Yanagi, H.; Kamiya, T.; Hirano, M.; Hosono, H. Large Domain Growth of GaN Epitaxial Films on Lattice-Matched Buffer Layer $ScAlMgO_4$. *Mater. Sci. Eng., B* **2009,** *161* (1-3), 66-70.
6. Tang, H. L.; Xu, J.; Dong, Y. J.; Lin, H.; Wu, F. Study on Growth and Characterization of $ScAlMgO_4$ Substrate Crystal. *J. Alloys Compd.* **2009,** *471* (1-2), L43-L46.
7. Zhou, H. T.; Liang, Y.; Huang, W. X.; Ye, N.; Zou, Y. Q. Single-Crystal Structure of $ScAlMgO_4$. *Chin. J. Struct. Chem.* **2009,** *28* (8), 947-950.
8. Ishizaka, A. Magic Number and Quasi-Melting Temperature Discovered in Crystal Growth and Surface Phase Transitions. *Adv. Colloid Interface Sci.* **1997,** *71-2*, 165-182.
9. Fujita, T. C.; Kozuka, Y.; Uchida, M.; Tsukazaki, A.; Arima, T.; Kawasaki, M. Odd-Parity Magnetoresistance in Pyrochlore Iridate Thin Films with Broken Time-Reversal Symmetry. *Sci. Rep.* **2015,** *5*.
10. Tsuei, C. C.; Gupta, A.; Trafas, G.; Mitzi, D. Superconducting Mercury-Based Cuprate Films with a Zero-Resistance Transition-Temperature of 124 Kelvin. *Science* **1994,** *263* (5151), 1259-1261.
11. Ohta, H.; Nomura, K.; Orita, M.; Hirano, M.; Ueda, K.; Suzuki, T.; Ikuhara, Y.; Hosono, H. Single-Crystalline Films of the Homologous Series $InGaO_3(ZnO)_m$ Grown by Reactive Solid-Phase Epitaxy. *Adv. Funct. Mater.* **2003,** *13* (2), 139-144.
12. Ogo, Y.; Nomura, K.; Yanagi, H.; Ohta, H.; Kamiya, T.; Hirano, M.; Hosono, H. Growth and Structure of Heteroepitaxial Thin Films of Homologous Compounds $RAO_3(MO)_m$ by Reactive Solid-Phase Epitaxy: Applicability to a Variety of Materials and Epitaxial Template Layers. *Thin Solid Films* **2006,** *496* (1), 64-69.
13. Obata, T.; Takahashi, R.; Ohkubo, I.; Oshima, M.; Nakajima, K.; Chikyow, T.; Koinuma, H.; Matsumoto, Y. Epitaxial $ScAlMgO_4$ (0001) Films Grown on Sapphire Substrates by Flux-Mediated Epitaxy. *Appl. Phys. Lett.* **2006,** *89* (19).
14. Evans, P. G.; Chen, Y.; Tilka, J. A.; Babcock, S. E.; Kuech, T. F. Crystallization of Amorphous Complex Oxides: New Geometries and New Compositions via Solid Phase Epitaxy. *Curr. Opin. Solid State Mater. Sci.* **2018,** *22*, 229-242.
15. Hiramatsu, H.; Ohta, H.; Suzuki, T.; Honjo, C.; Ikuhara, Y.; Ueda, K.; Kamiya, T.; Hirano, M.; Hosono, H. Mechanism for Heteroepitaxial Growth of Transparent P-type Semiconductor: LaCuOS by Reactive Solid-Phase Epitaxy. *Cryst. Growth Des.* **2004,** *4* (2), 301-307.
16. Katase, T.; Noinura, K.; Ohta, H.; Yanagi, H.; Kamiya, T.; Hirano, M.; Hosono, H. Fabrication of $ScAlMgO_4$ Epitaxial Thin Films Using $ScGaO_3(ZnO)_m$ Buffer Layers and Its

Application to Lattice-Matched Buffer Layer for ZnO Epitaxial Growth. *Thin Solid Films* **2008,** *516* (17), 5842-5846.
17. Katase, T.; Nomura, K.; Ohta, H.; Yanagi, H.; Kamiya, T.; Hirano, M.; Hosono, H. Fabrication of Atomically Flat $ScAlMgO_4$ Epitaxial Buffer Layer and Low-Temperature Growth of High-Mobility ZnO Films. *Cryst. Growth Des.* **2010,** *10* (3), 1084-1089.
18. Momma, K.; Izumi, F. VESTA 3 for Three-Dimensional Visualization of Crystal, Volumetric and Morphology Data. *J. Appl. Crystallogr.* **2011,** *44*, 1272-1276.
19. Kimizuka, N.; Mohri, T. Structural Classification of $RAO_3(MO)_n$ Compounds (R = Sc, In, Y, or Lanthanides; A = Fe(III), Ga, Cr, or Al; M = Divalent Cation; n = 1-11). *J. Solid State Chem.* **1989,** *78* (1), 98-107.
20. *ICDD PDF Powder Diffraction File*, International Centre for Diffraction Data: Newtown Square, Pennsylvania, United States.
21. Ohtomo, A.; Tamura, K.; Saikusa, K.; Takahashi, K.; Makino, T.; Segawa, Y.; Koinuma, H.; Kawasaki, M. Single Crystalline ZnO films Grown on Lattice-Matched $ScAlMgO_4$(0001) Substrates. *Appl. Phys. Lett.* **1999,** *75* (17), 2635-2637.
22. Gallagher, J. C.; Esser, B. D.; Morrow, R.; Dunsiger, S. R.; Williams, R. E. A.; Woodward, P. M.; McComb, D. W.; Yang, F. Y. Epitaxial growth of iridate pyrochlore Nd2Ir2O7 films. *Scientific Reports* **2016,** *6*.
23. Solaga, T.; Mortlock, A. J. Concentration Dependence of the Tracer Diffusion of Sc in Single Crystal MgO. *Phys. Status Solidi A* **1970,** *3* (4), K247-K250.
24. Zhang, D. L.; Qiu, C. X.; Wong, W. H.; Pun, E. Y. B. Diffusion Properties of Scandium in Lithium Niobate Crystal. *J. Am. Ceram. Soc.* **2014,** *97* (9), 2903-2908.
25. Roine, A. HSC Chemistry Version 9.9. Outokumpu Research Organization: Pori, Finland.
26. Brillson, L. J. *Surfaces and Interfaces of Electronic Materials*, John Wiley & Sons: 2010; Vol. 7.